AD-A098 522 TEXAS UNIV AT AUSTIN APPLIED RESEARCH LABS F/G 20/1
A SUMMARY OF THE RESULTS OF A STUDY OF ACOUSTIC BOTTOM INTERACT--ETC(U)
NOV 80 S R RUTHERFORD, S G PAYNE, R A KOCH N00014-78-C-0113
UNCLASSIFIED ARL-TR-80-56 NL

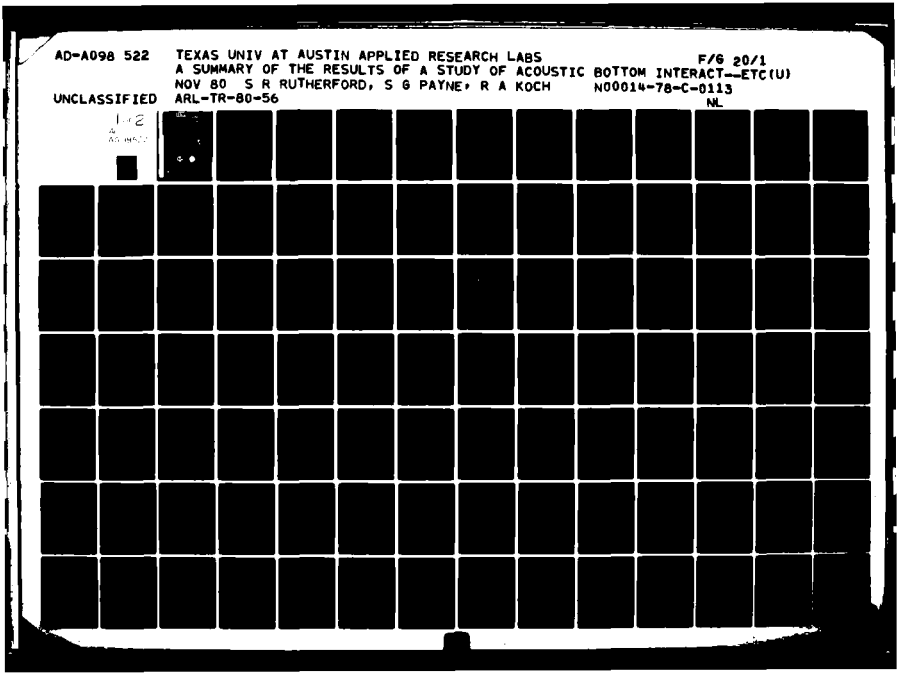

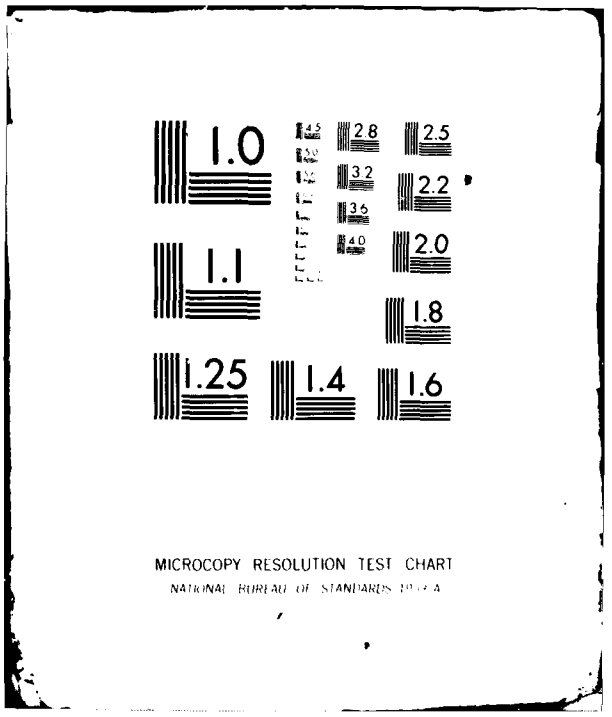
1.0
1.1
1.25
1.4
1.6
1.8
2.0
2.2
2.5
2.8
3.2
3.6
4.0
MICROCOPY RESOLUTION TEST CHART
NATIONAL BUREAU OF STANDARDS 1963-A

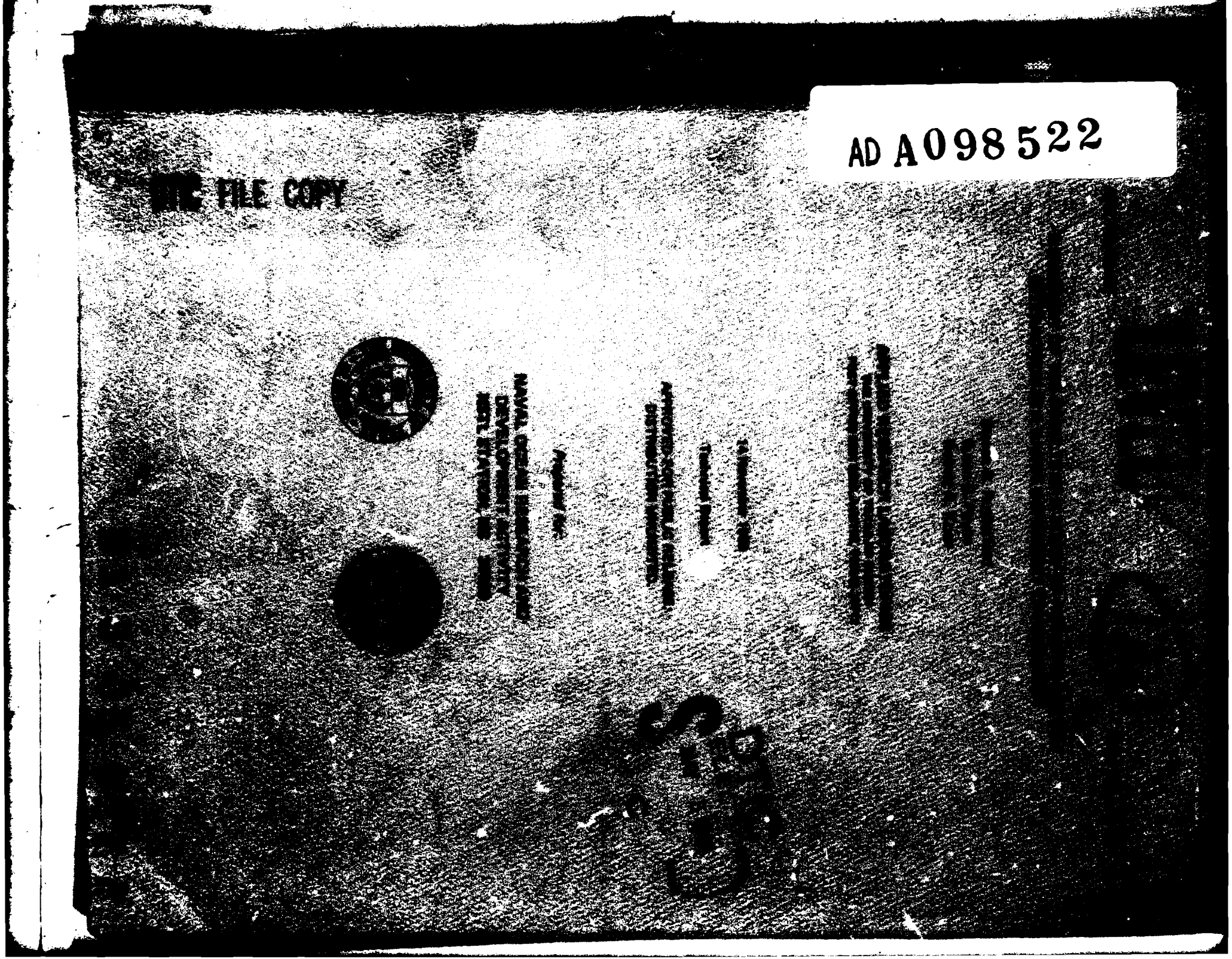
AD A098522
DTIC FILE COPY

UNCLASSIFIED

SECURITY CLASSIFICATION OF THIS PAGE (When Data Entered)

REPORT DOCUMENTATION PAGE

READ INSTRUCTIONS BEFORE COMPLETING FORM

1. REPORT NUMBER	2. GOVT ACCESSION NO.	3. RECIPIENT'S CATALOG NUMBER
	AD-A098 522	

4. TITLE (and Subtitle)

A SUMMARY OF THE RESULTS OF A STUDY OF ACOUSTIC BOTTOM INTERACTION IN A RANGE DEPENDENT ENVIRONMENT

5. TYPE OF REPORT & PERIOD COVERED: technical report

6. PERFORMING ORG. REPORT NUMBER: ARL-TR-80-56

7. AUTHOR(s)

Steven R. Rutherford, Susan G. Payne, and Robert A. Koch

8. CONTRACT OR GRANT NUMBER(s): N00014-78-C-0113

9. PERFORMING ORGANIZATION NAME AND ADDRESS

Applied Research Laboratories
The University of Texas at Austin
Austin, Texas 78712

10. PROGRAM ELEMENT, PROJECT, TASK AREA & WORK UNIT NUMBERS

11. CONTROLLING OFFICE NAME AND ADDRESS

Naval Ocean Research and Development Activity
NSTL Station, MS 39529

12. REPORT DATE: 14 November 1980

13. NUMBER OF PAGES: 124

14. MONITORING AGENCY NAME & ADDRESS (if different from Controlling Office)

LEVEL II

15. SECURITY CLASS. (of this report): UNCLASSIFIED

15a. DECLASSIFICATION/DOWNGRADING SCHEDULE

16. DISTRIBUTION STATEMENT (of this Report)

Approved for Public Release; Distribution Unlimited.

DTIC ELECTE MAY 5 1981 C

17. DISTRIBUTION STATEMENT (of the abstract entered in Block 20, if different from Report)

18. SUPPLEMENTARY NOTES

19. KEY WORDS (Continue on reverse side if necessary and identify by block number)

bottom interaction
geoacoustics
mode/mode coupling
adiabatic propagation
computer model
range variable environments

20. ABSTRACT (Continue on reverse side if necessary and identify by block number)

This report summarizes the results of research carried out during 1980 at Applied Research Laboratories, The University of Texas at Austin (ARL:UT), on acoustic bottom interaction in a range variable environment. The major topics treated are adiabatic normal mode modeling in a range variable medium, the role of attenuation in upslope and downslope propagation, and further theoretical studies into the role of mode/mode coupling in a range variable environment. In addition, some possible future directions of work concerning bottom interaction in a range variable environment are described.

DD FORM 1 JAN 73 1473 EDITION OF 1 NOV 65 IS OBSOLETE

UNCLASSIFIED

SECURITY CLASSIFICATION OF THIS PAGE (When Data Entered)

AD A104434

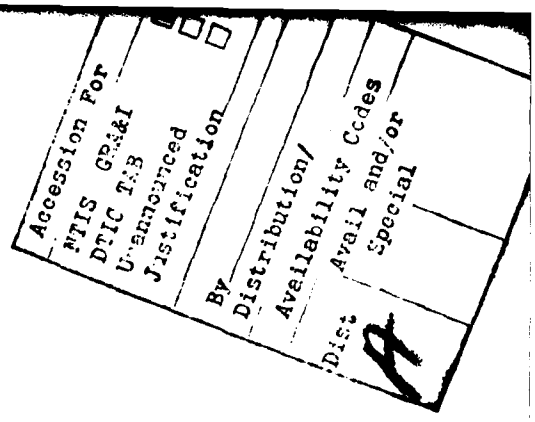

TABLE OF CONTENTS

LIST OF FIGURES

CHAPTER I

INTRODUCTION

In this report the results of an FY 80 study of bottom interaction in a range dependent environment are summarized and presented. Bottom interaction in a range variable environment represents one of three areas of study in the ARL:UT FY 80 bottom interaction program. The main thrust of this area of work is to determine the effects and relative importance of lateral subbottom variability and sloping boundaries on the propagation of low frequency underwater sound.

The range variability study is now in its third year. The FY 78 work focused primarily on the assessment of analytical tools for describing sound propagation in a range variable environment and began a line of work concerned with determining the importance of lateral subbottom variability and sloping boundaries. The FY 78 results are summarized in Ref. 1.

The FY 79 range variability work was a continuation of the work begun in FY 78 and had several foci. In FY 78 it was determined that coupled normal mode theory[2,3] offered the best means for modeling and investigating bottom interaction mechanisms in a range variable environment. One phase of the FY 79 work involved establishing a firm theoretical foundation for the application of coupled mode theory to problems of interest. One particular problem investigated was the effect of boundary condition approximations[4,5] on coupled mode theory in sloping bottom problems, and a corrected theory to counteract the undesirable aspects of the approximation was derived. The implications of the adiabatic approximation[6] were also studied and the FY 78 work, concerning the importance of lateral variability and sloping boundaries, was continued.

Another phase of the FY 79 work concerned building the appropriate tools necessary to investigate the effects of range variability. In FY 79 the groundwork was laid for an adiabatic normal mode model, and work was begun on the development of the model. This work continued into FY 80 where it was completed. All the FY 79 bottom interaction work is summarized in Ref. 8.

The work summarized in this report is presented in Chapters II-IV. Chapter II reports on the adiabatic normal mode modeling effort that was begun in FY 79 and recently completed in FY 80. The basic propagation loss modeling scheme, which has been named ADIAB, is described in a general manner. The computation scenario and the theory of adiabatic normal mode propagation are described, but there is no discussion of computational algorithms, computer code, or details concerning input/output. The working details of ADIAB will be presented in a specific report to be issued later, but Chapter II contains some numerical examples of the outputs from ADIAB. These numerical examples are compared with actual propagation loss data to illustrate the power of the modeling method.

In Chapter III the results of a study of the sensitivity of upslope and downslope propagation to subbottom attenuation are presented. The numerical modeling results that are shown are produced using the model ADIAB described in Chapter II. The conclusions of Chapter III are listed below.

It has been determined that the gross structure (minus phase effects) of acoustic propagation over a sloping bottom can be explained in terms of bottom attenuation effects, renormalization effects, spreading loss, and mode cutoff effects. The renormalization effects produce a gain in upslope propagation and a loss in downslope propagation. The mode cutoff effects are not operational in downslope propagation.

Concerning downslope propagation, the following determinations have been made.

(1) The deep water acoustic field is particularly sensitive to the shallow water bottom attenuation profile.

(2) The importance of bottom interaction mechanisms decreases as sound propagates from shallow to deep water and becomes negligible when the deep water sound channel becomes fully developed.

(3) The sensitivity of the acoustic field to the bottom attenuation greatly increases as sound propagates from shallow to deep water.

(4) Downslope acoustic propagation is not particularly sensitive to bottom slope.

With regard to upslope acoustic propagation, the following determinations have been made.

(1) The shallow water acoustic field is particularly sensitive to the shallow water bottom attenuation profile.

(2) The importance of bottom interaction mechanisms increases as sound travels upslope from deep to shallow water where it reaches a maximum.

(3) The sensitivity of the acoustic field to the bottom attenuation greatly increases as sound travels from deep to shallow water.

(4) Upslope sound transmission is sensitive to slope angle, especially for deep or shallow source depths.

(5) A slope enhancement effect is possible in upslope propagation and is most apparent for source depths in the deep sound channel.

Chapter IV considers some further theoretical work on the coupled mode theory of sound propagation. In this chapter the solutions to the coupled radial equations that describe the normal mode amplitudes with range are studied in detail. Several expressions for the radial functions are obtained employing a WKB approximate radial Green's function. First order perturbation theory is applied to these expressions to obtain functions of utility for numerical computation. The attenuation process is also introduced into the mathematical formalism. The second part of Chapter IV concerns application of the theory developed in the first part. In this section arguments for the neglect of backscattering in a range

dependent waveguide and ways of estimating the importance of mode coupling effects are given. Also, approximate ways of introducing mode/mode coupling that could be incorporated into ADIAB are discussed.

This report concludes with Chapter V, which looks at possible future directions of the bottom interaction study concerning range variability. There are many problems to be addressed, such as the level of detail required to characterize the range variability of the ocean bottom, range averaging, and energy partitioning. An attempt is made to pose the appropriate questions to these concerns.

CHAPTER II

AN ADIABATIC NORMAL MODE THEORY PROPAGATION LOSS MODEL

In this chapter an adiabatic propagation loss model, developed at ARL:UT as a tool for investigating the propagation of sound in a range variable waveguide, is described and discussed. First, the basic theory of an adiabatic normal mode description of underwater sound propagation in a range dependent medium will be discussed. Next, the numerical implementation of adiabatic mode theory is described. Finally, numerical examples are given illustrating various output options of the model. The numerical examples are then compared to actual propagation loss data.

A. Theory

Adiabatic normal mode theory is an approximate form of the coupled mode theories of sound propagation proposed independently by Pierce[2] and Milder.[3] In a coupled mode theory of sound propagation the acoustic field due to a point source in a range variable medium is expressed as

$$\psi(z,r) = \sum_n R_n(r)\ \phi_n(z,r) \quad . \tag{2.1}$$

Implicit in Eq. (2.1) is the neglect of the continuous spectrum of eigenvalues. The field ψ is the velocity potential and satisfies the following partial differential equation in cylindrical coordinates,

$$\nabla^2\psi + k^2(z,r)\psi = -4\pi\delta(\vec{r}-\vec{r}_o) \quad . \tag{2.2}$$

In Eq. (2.2) $k(z,r)$ is the wave number of the medium, which can vary with depth and range, and $\vec{r}_o$ denotes the position of the point source. The particle velocity and acoustic pressure are to be continuous across all discontinuities in the medium. This requirement translates into the following boundary conditions on ψ. The continuity of particle velocity requires that the normal derivative of ψ, $(\partial\psi/\partial n)$, be continuous across surfaces of discontinuity. The continuity of pressure requires that $\rho\psi$ be continuous, where ρ is the material density of the medium. The boundary condition requiring continuity of the normal derivative of ψ gives rise to an additional source of range dependence whenever sloping interfaces are present. In practice, the partial separation of range and depth variables implied in Eq. (2.1) requires that the normal derivative boundary conditions be approximated whenever sloping boundaries are present. Since this boundary condition approximation does not affect the adiabatic approximation to coupled mode theory, it will not be discussed here. The nature of the boundary condition approximation and a method for correcting it are discussed in detail in Refs. 4 and 5.

In Eq. (2.1) the ϕ_n functions are normal mode depth functions that satisfy

$$\left[\frac{d^2}{dz^2} + k^2(z,r) - k_n^2(r)\right] \phi_n(z,r) = 0 \tag{2.3}$$

at each range point throughout the waveguide. Across any interfaces in the waveguide, $\rho\phi_n$ and $d\phi_n/dz$ are required to be continuous. In Eq. (2.3) the $k_n(r)$ are the normal mode eigenvalues which depend on range whenever the waveguide varies in range. The radial functions $R_n(r)$, Eq. (2.1), satisfy the following set of coupled differential equations.

$$\left[\frac{d^2}{dr^2} + \frac{1}{r}\frac{d}{dr} + k_m^2(r)\right] R_m(r) = -\sum_n \left\{A_{mn} R_n + B_{mn}\left(\frac{R_n}{r} + 2\frac{dR_n}{dr}\right)\right\} \tag{2.4}$$

The A_{mn} and B_{mn} are referred to as the coupling coefficients and are given by

$$A_{mn}(r) = \int_{\bullet}^{\infty} \rho(z)\phi_m(z,r) \frac{\partial^2}{\partial r^2} \phi_n(z,r)dz \quad , \qquad (2.5)$$

$$B_{mn}(r) = \int_{\bullet}^{\infty} \rho(z)\phi_m(z,r) \frac{\partial \phi_n}{\partial r}(z,r)dz \quad . \qquad (2.6)$$

In the adiabatic approximation to coupled mode theory,[2,3,10,11,12] the possibility of the coupling of energy between normal modes is ignored. This entails neglecting the coupling terms on the right-hand side of Eq. (2.4). The validity of the adiabatic approximation depends on the rate with which the medium is varying in range. References 4, 6, and 7 investigate the adiabatic approximation as a function of lateral geoacoustic parameter variability and sloping boundaries. In Chapter IV some new methods for determining the validity of the adiabatic approximation are proposed and discussed. The work discussed in this chapter will assume the validity of the adiabatic approximation and will defer a discussion of mode coupling effects to Chapter IV and future work.

The radial equation in the adiabatic approximation therefore satisfies the following differential equation,

$$\left[\frac{d^2}{dr^2} + \frac{1}{r}\frac{d}{dr} + k_m^2(r)\right] R_m(r) = 0 \quad . \qquad (2.7)$$

The acoustic field given by Eq. (2.1) with $R_n(r)$ given in the adiabatic approximation can be shown to conserve energy (see Refs. 4 and 5). The power associated with a particular mode at the source remains associated with that mode as long as the mode continues to exist in the waveguide.

In the past, several adiabatic propagation loss models have been developed. One such model is SNAP,[13] a shallow water adiabatic propagation

loss model that was developed at SACLANTCEN. Another modeling scheme,[11] which is based on the assumption of segment-wise linear variation of the wave number squared with depth and the eigenvalues squared with range, employs Airy functions for both the depth and radial functions. The model that is described in this chapter is a numerical tool in which the user is allowed a very general description of the propagation medium, particularly in the local depth variability of the bottom sound speed and attenuation and the layering structure of the bottom.

B. Numerical Implementation

The implementation of adiabatic normal mode theory to produce a numerical propagation loss model is accomplished in three basic steps. First, the medium is partitioned into range bins and a set of normal modes and eigenvalues for each range bin is computed. Second, the mode attenuation coefficients are computed for each range bin, and the mode eigenvalues are fit by a cubic spline function. Third, radial functions are computed and the appropriate mode summations are performed to produce the desired propagation loss output such as propagation loss versus depth or range.

1. Stage One

The partitioning of the medium is presently left to the discretion of the user. This process is schematically illustrated in Fig. II.1. At the midpoint of each range bin a set of normal mode depth functions and eigenvalues are computed, retained, and become associated with that range bin. The mode calculations are carried out using NEMESIS,[14] which numerically integrates Eq. (2.3) at the midpoint of the range bin, assuming locally horizontal interfaces. The sound speed variations with depth at this range point may be completely general in nature.

The partitioning of the medium and the normal mode computations are by far the most time consuming part of the computational scheme. As stated before, the partitioning of the medium is left to the user who,

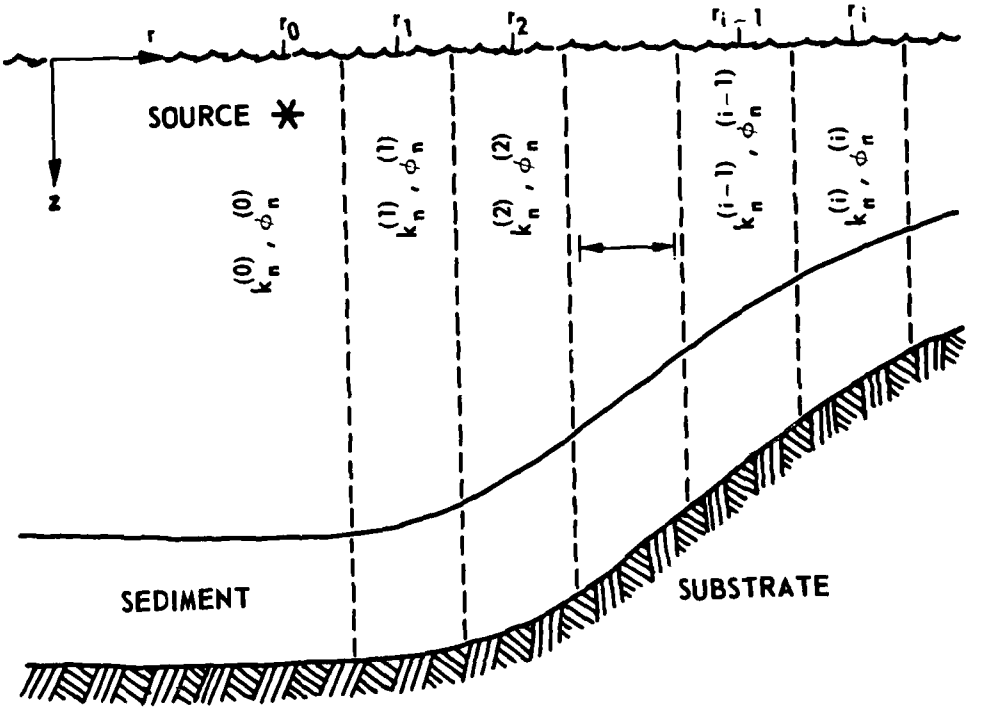

FIGURE II.1
SCHEMATIC DIAGRAM OF PARTITIONING OF A WAVEGUIDE INTO RANGE BINS

ARL:UT
AS-80-855-P
SRR - GA
3 - 6 - 80

in principle, can sample the medium in range as finely as desired. Of course, the finer the partitioning of the medium the more lengthy and time consuming are the mode calculations. In practice there must be some compromise between the added accuracy obtained by fine sampling and the computational time requirements.

2. Stage Two

The second and third stages of the adiabatic calculations are linked loosely together under the model name ADIAB. ADIAB assumes that the medium has been partitioned and the normal modes computed and stored on disk files and proceeds with the calculations required to produce propagation loss.

The second stage of the adiabatic calculations involves the calculation of mode attenuation coefficients for each range bin and fitting the eigenvalues through all the range bin midpoints using a cubic spline. The fitting procedures are applied to the eigenvalues to facilitate the computation of the radial functions, which are computed using the WKB approximation rather than solving Eq. (2.7) numerically. In the WKB approximation the solution of Eq. (2.7) is given by

$$R_n(r) = \frac{A_n \exp(i\int^r k_n[x]dx)}{\sqrt{k_n(r)r}} \quad , \qquad (2.8)$$

where A_n is a constant that depends on mode number. The fitting of the eigenvalues allows the phase integration in Eq. (2.8) to be done analytically rather than numerically, with significant savings in computational time. The phase integral for each mode is evaluated at the midpoint of each range bin, and these values are then fitted with a cubic spline. This is done to enable the value of the phase integral to be easily and quickly computed at any range point.

The mode attenuation coefficients, which are also evaluated in the second computational stage, are used to incorporate the effects of attenuation into the radial functions. The mode attenuation coefficients are computed by first order perturbation theory using the following integral.

$$\delta_n(r) = \frac{1}{k_n(r)} \int_0^\infty \alpha(z,r)k(z,r)\rho(z)\phi_n^2(z,r)dz \quad . \qquad (2.9)$$

In Eq. (2.9), $\alpha(z,r)$ is the attenuation profile, $k(z,r)$ the wave number, and $\rho(z)$ the density, which is assumed to be constant within a layer. One set of mode attenuation coefficients is computed for each range bin using the attenuation and sound speed profiles at the midpoint of the range bin in question. After the attenuation coefficients are computed for each range bin, attenuation can be incorporated into Eq. (2.8) as follows.

$$R_n(r) = \frac{A_n}{\sqrt{k_n(r)r}} \exp\left(i\int^r k_n(x)dx - \int^r \delta_n(x)dx\right) \quad , \qquad (2.10)$$

with the δ_n being independent of range within a bin. For a more detailed discussion concerning first order perturbation theory and normal mode attenuation coefficients, consult Ref. 4.

3. Stage Three

The desired propagation loss calculations are performed in the third stage of the adiabatic field calculation, i.e., the second part of program ADIAB. The computed propagation loss is given by

$$I(z,r;z_o,r_o) = 10 \log|\psi(z,r)|^2 \quad . \qquad (2.11)$$

In Eq. (2.11) I is the propagation loss between the field point (z,r) and a point source at (z_o,r_o). At present the second part of ADIAB is set up to compute propagation loss versus range for given source-receiver depths or propagation loss versus depth for given source-receiver ranges. Both coherent and incoherent computations of propagation loss are performed. Another option available to the user is the capability to compute propagation loss between a fixed source and a receiver that moves along an interface at a fixed distance above or below the boundary. This option can conceivably be used to examine the response of arrays of receivers located along a sloping boundary.

The propagation loss computation phase of ADIAB can be run only after stage one is accomplished. The fitting coefficients and mode attenuation coefficients computed in the first phase of ADIAB can be saved and used repeatedly in propagation loss calculations. In the standard propagation loss calculation in ADIAB, a fixed source is assumed while the receiver position changes with range. There is, however, an option where the receiver is fixed and the source position changes.

The coherent propagation loss is computed from the velocity potential ψ using the following expression.

$$\psi(z,r) = i\rho(z_o)\exp(-i\pi/4)\sqrt{\frac{2\pi}{|r-r_o|}} \sum_n \frac{\exp\left(i \int_{r_o}^{r} k_n[x]dx - \int_{r_o}^{r} \delta_n[x]dx \right)}{\sqrt{k_n(r)}}$$

$$\times \phi_n(z,r)\phi_n(z_o,r_o) \quad . \tag{2.12}$$

In Eq. (2.12) the source is stationary at (z_o,r_o) and the receiver is at (z,r). The constants and the mode function evaluated at the receiver in Eq. (2.12) arise from the requirement that the adiabatic field match the field for a horizontally stratified medium in the source region. The velocity potential as expressed by Eq. (2.12) neglects any backscattered field, because the adiabatic approximation is an approximation of zero

order in the rates of change of the medium. The backscattered field can be shown to be of first order in these same quantities and cannot be consistently retained.

In the propagation loss computation phase of ADIAB the mode functions and attenuation coefficients that enter into Eq. (2.12) are fixed within a range bin. The fitted cubic polynomials describing the range behavior of the phase integral are used to analytically evaluate the phase integral and the $k_n(r)$ term in the denominator of Eq. (2.12). The accumulated attenuation between source and field point for each mode is also easily computed analytically, since the mode attenuation coefficients are constant within a range bin. After the velocity potential has been computed for a particular source/field point geometry, the coherent propagation loss is computed from Eq. (2.11). The term "coherent" is used to indicate that phasing effects between modes are included. The complex velocity potential is used to compute the propagation loss because it is more computationally efficient, i.e., a single mode sum is performed rather than a double mode sum.

The incoherent evaluation of propagation loss is obtained by summing the normal modes without regard to phase. The expression evaluated in ADIAB is obtained from Eqs. (2.11) and (2.12) by ignoring the off-diagonal terms in the resulting double summation. This expression is given by

$$I_{inc}(z,r;z_o,r_o) = 10 \log \left\{ \frac{2\pi\rho^2(z_o)}{|r-r_o|} \sum_n \frac{\exp\left(-2\int_{r_o}^{r} \delta_n(x)dx\right)}{k_n(r)} \phi_n^2(z,r) \right. \times \left. \phi_n^2(z_o,r_o) \right\} . \tag{2.13}$$

In Eqs. (2.12) and (2.13) the summation over mode number n goes from the lowest mode number to an upper limit, which is the number of discrete modes that can propagate between the source and field points. Therefore, for a fixed source in deep water and a receiver moving upslope to shallower water, the number of terms in the summations of Eqs. (2.12)

and (2.13) decreases with increasing range. Conversely, for a fixed source in shallow water and a field point moving downslope into deeper water, the number of terms in the mode summations stays the same, since the fixed shallow water source position usually has the least number of modes, assuming a monotonic increase in water depth with range. Once a normal mode reaches cutoff, it can be ignored within the adiabatic approximation because there is no mechanism to impart energy to it should it reappear farther down range.

As mentioned earlier, the standard calculation in ADIAB assumes a fixed source and a range variable receiver. The converse situation of a fixed receiver and a varying source position is obtained by interchanging the source-receiver locations in Eq. (2.12) and letting the source position vary in range. For a receiver fixed at (z_o, r_o) and a variable source position denoted by the field point (z,r), the field is given by

$$\psi(z_o,r_o) = i\rho(z)\exp(-i\pi/4)\sqrt{\frac{2\pi}{|r-r_o|}}\sum_n \frac{\exp\left(\int_r^{r_o}[ik_n(x) - \delta_n](x)]dx\right)}{\sqrt{k_n(r_o)}}$$

$$\times \phi_n(z_o,r_o)\phi_n(z,r) \quad . \tag{2.14}$$

Since only the absolute square of ψ is needed to compute transmission loss, the fixed receiver calculation is obtained in precisely the same way as for the fixed source with the exception that the eigenvalues $k_n(r_o)$ in the denominator of the mode sum are now fixed in range. This is the only difference between the fixed source and the fixed receiver transmission loss calculations, and in numerous situations is of negligible importance.

4. Peripheral Programs

Program ADIAB is basically a transmission loss computational package. Two other peripheral programs which can be used in conjunction with ADIAB are under development at ARL:UT. The first of these programs

is an eigenvalue plotting package that produces plots of mode eigenvalues as a function of range and printouts of mode eigenvalues at user specified ranges. This particular program takes the fitting splines of the phase integrals, which were computed and stored in the first part of ADIAB, and computes the derivatives (i.e., $k_n(r)$) at required range points.

The second peripheral program under development computes various energy flux quantities. The total power transported radially by a point source through a cylindrical surface centered about the source is given in the adiabatic approximation by (see Ref. 4)

$$J_r = \sum_n J_r^{(n)} \quad , \tag{2.15}$$

$$J_r^{(n)} = 2\pi^2 \omega \rho^2(z_o) \phi_n^2(z_o, r_o) \quad . \tag{2.16}$$

In Eqs. (2.15) and (2.16), (z_o, r_o) denotes the source location and $J_r^{(n)}$ is the power transported radially by mode n. The modal power amplitudes as well as the total power are independent of range, excluding mode cutoff effects, in the absence of attenuation. The effects of attenuation may be included by altering Eq. (2.16) so that

$$J_r^{(n)}(r) = 2\pi^2 \omega \rho^2(z_o) \phi_n^2(z_o, r_o) \exp\left(-2 \int_{r_o}^{r} \delta_n(x) dx\right) \quad . \tag{2.17}$$

The energy flux program that is being developed calculates J_r and $J_r^{(n)}$ as a function of range using Eqs. (2.17) and (2.15) and the mode attenuation coefficients computed and stored in the first part of ADIAB. The program will also compute some other quantities that are defined and discussed below.

The power transported by waterborne modes, J_w, and bottom interacting modes, J_B, can be defined as follows.

$$J_w(r) = \sum_{n=1}^{M(r)} J_r^{(n)}(r) \quad , \tag{2.18}$$

$$J_B(r) = \sum_{n=M(r)+1}^{N(r)} J_r^{(n)}(r) \quad , \tag{2.19}$$

$$J_r(r) = J_w(r) + J_B(r) \quad . \tag{2.20}$$

In Eqs. (2.18) and (2.19) M(r) denotes the last mode with a turning point in the water and N(r) denotes the maximum number of discrete modes allowed to exist. Both M(r) and N(r) can vary with range.

The energy flux program, which evaluates J_r and $J_r^{(n)}$, also computes J_w and J_B as well as various ratios such as J_w/J_B, J_w/J_r, and J_B/J_r as functions of range. These functions are of potential use in investigating bottom interaction effects in range variable environments. For example, using ratios such as J_w/J_r and J_B/J_r one could examine the partitioning of energy between the water column and the bottom and how it changes as a function of range. The ratio of waterborne energy flux to bottom interacting flux, J_w/J_B, could be used as a measure of the importance of bottom interaction as a function of range. It is conceivable that the behavior of this ratio as a function of range upslope could be used to find positions along a slope where the contaminating effects of bottom interacting energy are minimized through the combined effects of bottom attenuation and slope geometry. The potential applications to slope mounted arrays looking into deep water are obvious.

Figure II.2 is a schematic diagram indicating the present adiabatic computational capabilities and those soon to be completed. A detailed report concerning the adiabatic propagation loss program ADIAB will be published at a later date. This report will include a listing of the computer code, detailed user instructions, and discussions of input/output procedures, run times, and computational algorithms.

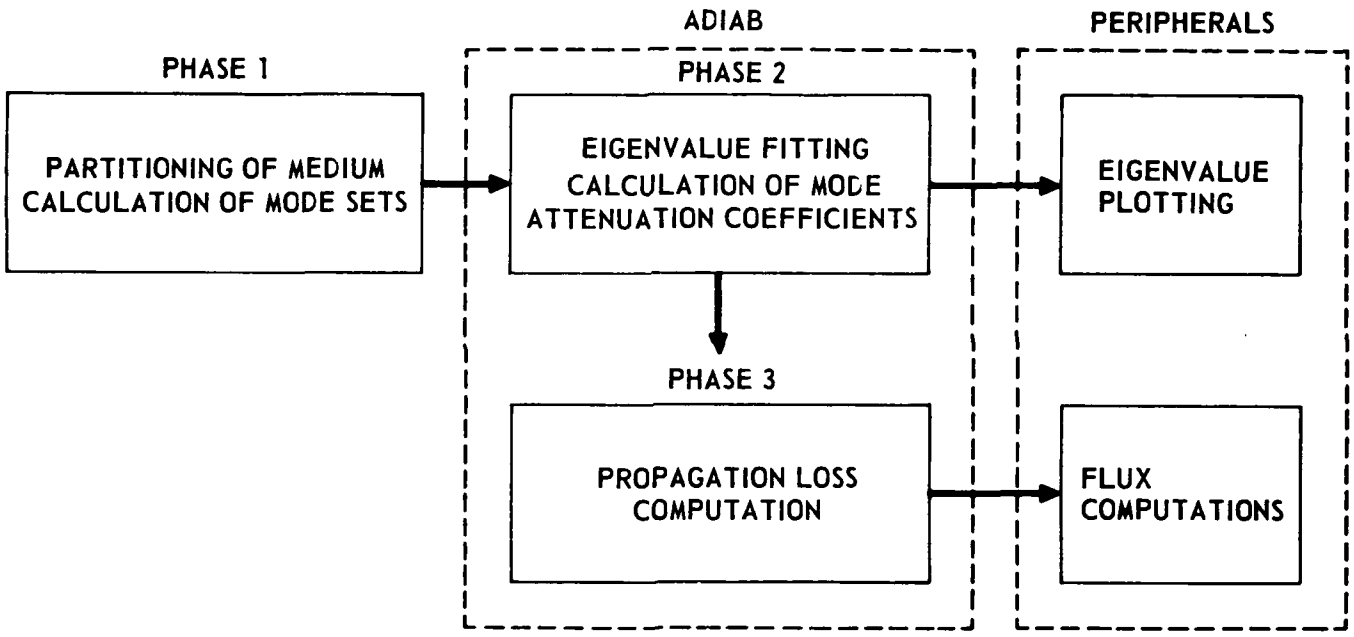

FIGURE II.2
SCHEMATIC DIAGRAM OF ADIABATIC MODELING CAPABILITIES

ARL:UT
AS-80-856-P
SRR-GA
3-6-80

C. Numerical Examples

In this section numerical examples illustrating some of the previously described adiabatic computational capabilities will be presented. Comparisons are made between model calculations and propagation loss data generated from experiments involving upslope and downslope runs and explosive sources. The sound speed profiles and bathymetry for a representative downslope propagation run will be used to generate the examples presented in this section.

The bathymetry for the propagation loss track in question is shown in Fig. II.3. A source that moved downslope to deep water was located at a depth of 91 m, and receivers at depths of 18, 91, and 305 m were fixed in the shallow water at range zero. Although the propagation loss for this run was processed in many frequency bands, the results presented here will consist of the 50 Hz data only. In Fig. II.3 the compressed range scale indicates a drastic slope even though the average slope is only about 1°. For this small slope the adiabatic approximation should work quite well.

Figure II.4 shows some representative deep water velocity profiles along the propagation loss track, and Fig. II.5 shows the average sound speed profile used in the propagation loss calculations. The shallow water profiles were obtained by truncating Fig. II.5 at the appropriate depths. The subbottom structure in the propagation area was not known in any detail, but the layering and attenuation structure of the bottom were inferred from the shallow water portion of the data (see Ref. 9). A geoacoustic model of the sediment structure that produced good agreement with the data is given in Table I. In this model the sound speed was taken to be continuous across the water-sediment interface and throughout the sediment, and the attenuation was assumed to be constant within a sediment layer. The substrate began at a depth of 200 m below the water-sediment interface. The substrate shear and compressional wave speeds were 2700 and 5000 m/sec, respectively, and the density was 2.7 g/cm^3.

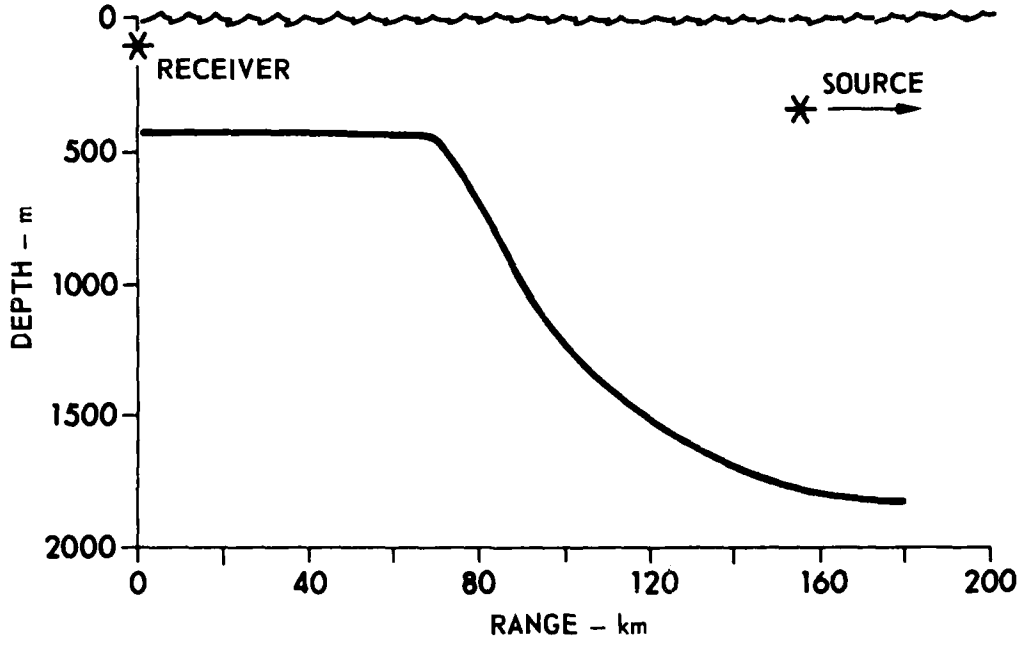

FIGURE II.3
BATHYMETRY FOR PROPAGATION LOSS RUN
(AVERAGE SLOPE ANGLE $\approx 1^{\circ}$)

ARL:UT
AS-80-857-P
SRR-GA
3-6-80

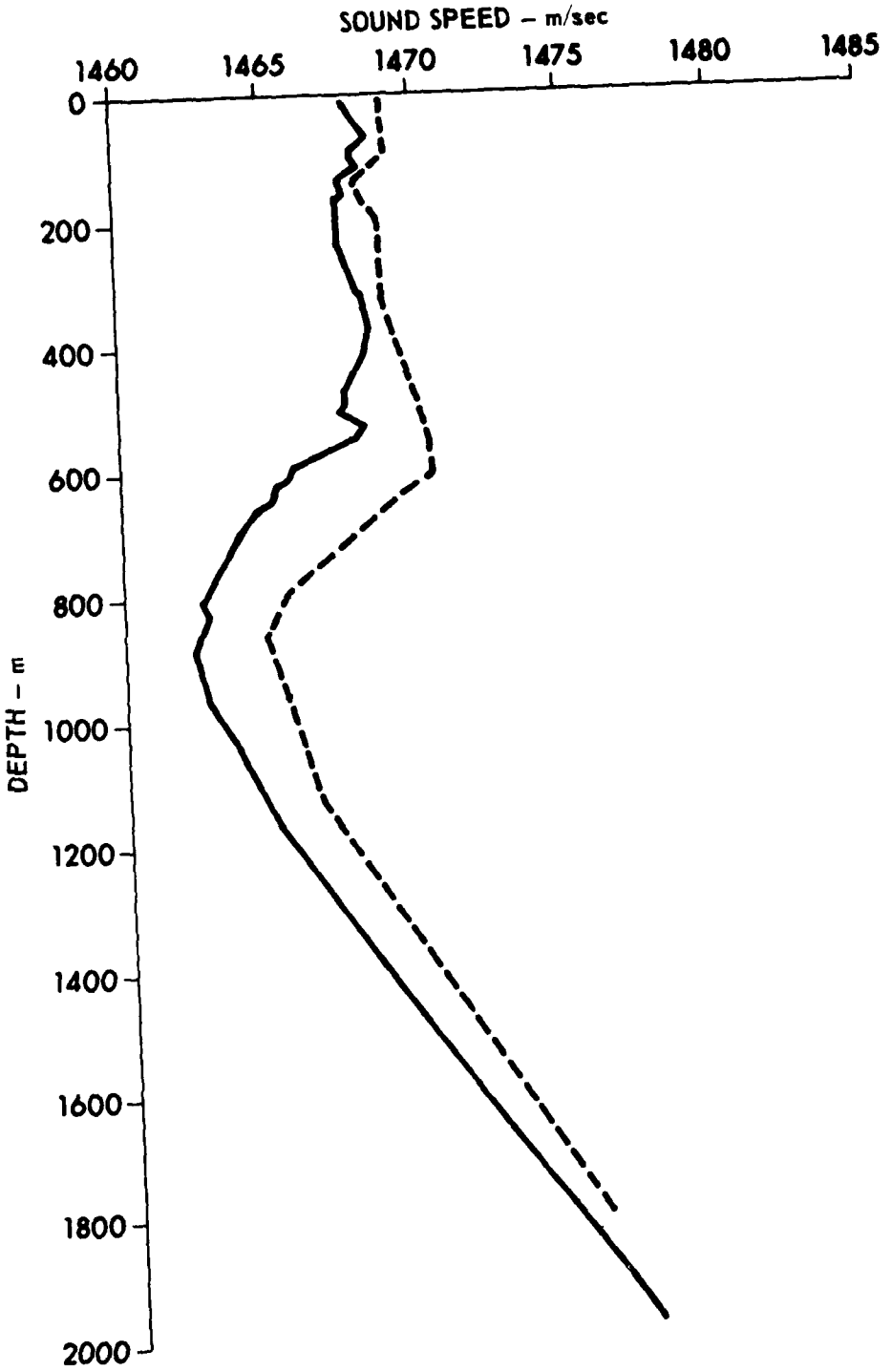

FIGURE II.4
SOUND SPEED PROFILES ALONG PROPAGATION LOSS TRACK

ARL:UT
AS-80-858-P
SRR-GA
3-6-80

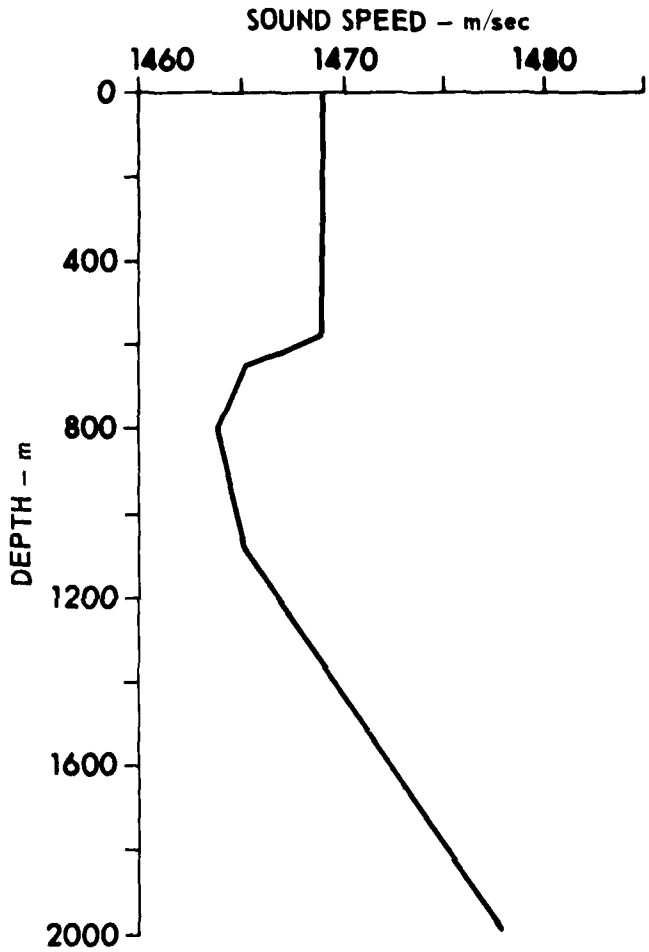

FIGURE II.5
DEEP WATER SOUND SPEED versus DEPTH

ARL:UT
AS-80-850-P
SRR-GA
2-27-80

TABLE I

SEDIMENT GEOACOUSTIC MODEL

Layer	Thickness (m)	Sound Speed Ratio at Top of Layer	Sound Speed Gradient (sec^{-1})	Density (g/cm^3)	Attenuation (dB/m/kHz)
1	15	1	1	1.4	0.01
2	35	1	1	1.4	0.0075
3	150	1	1	1.4	0.004

The substrate attenuations were taken as 0.03 dB/m/kHz for compressional waves and 0.2 dB/m/kHz for shear waves. This sediment-substrate model was retained throughout the propagation loss run.

Figures II.6 and II.7 show the incoherent propagation loss versus range for the 305 m receiver and the 91 m source depths. The stairstepped curve in Fig. II.6 is the raw computation and the curve in Fig. II.7 is a version that has been smoothed in range over a sliding window of 25 km. The stairstepped nature of the first curve results when a new range bin is entered and the mode functions change abruptly from those in the previous bin. Throughout the rest of this chapter and report, whenever incoherent propagation loss versus range is shown, it will be a smoothed version of the raw calculation. In the shallow water regions 36 discrete modes were possible. This number increased monotonically bin by bin until, in the deep water, 115 modes were possible. However, since the receiver was fixed in the shallow water, only 36 modes were included in the mode sums. Figure II.8 shows the coherent version of the curve in Fig. II.6.

Figure II.9 shows a comparison of the experimental data (illustrated by the crosses) with the smoothed model calculations (Fig. II.7) for 50 Hz. The calculations were generated with the geoacoustic model of Table I. Note the good agreement between data and calculations over most of the ranges. In the region of 140-180 km the data show some added structure and generally less propagation loss than the calculations. A comparison of Fig. II.8 with Fig. II.9 in the range interval in question indicates that the structure of the data in this region might be real and related to intermode phasing effects.

Figure II.10 shows a comparison of the propagation loss for the experimental data with the smoothed, incoherent, model transmission loss calculations for 91 m source and receiver depths. Figure II.11 shows the same comparison for 91 m source and 18 m receiver depths. The data for ranges greater than 120 km are missing in Fig. II.10, and the last two points near the 120 km range are suspect. However the shallow water

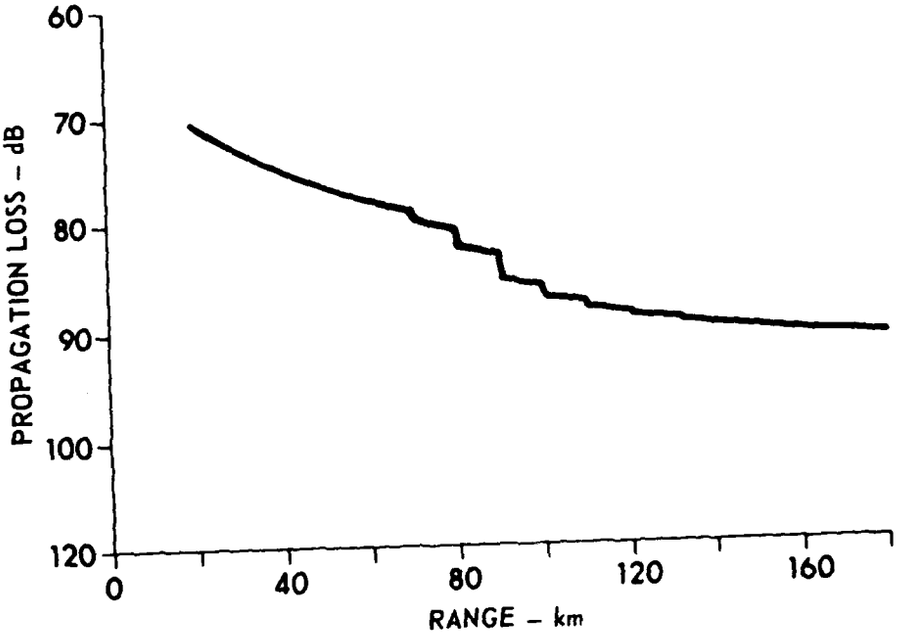

FIGURE II.6
RAW INCOHERENT PROPAGATION LOSS versus RANGE
SOURCE DEPTH: 91 m, RECEIVER DEPTH: 305 m
FREQUENCY: 50 Hz

ARL:UT
AS-80-859-P
SRR-GA
3-6-80

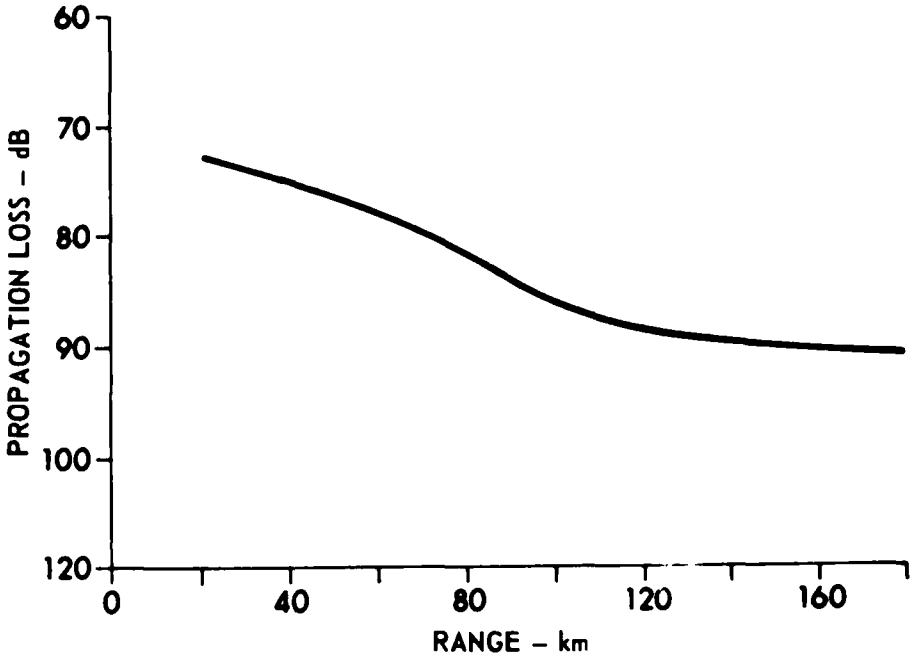

FIGURE II.7
SMOOTHED INCOHERENT PROPAGATION LOSS versus RANGE
SOURCE DEPTH: 91 m, RECEIVER DEPTH: 305 m
FREQUENCY: 50 Hz, SMOOTHING WINDOW: 25 km

ARL:UT
AS-80-860-P
SRR-GA
3-6-80

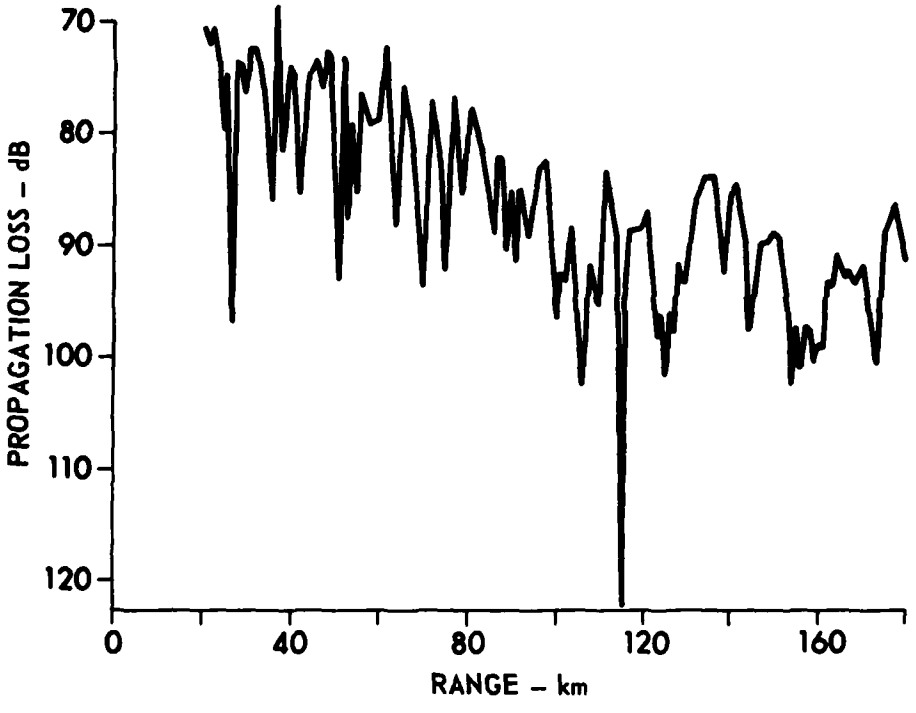

FIGURE II.8
COHERENT PROPAGATION LOSS versus RANGE
SOURCE DEPTH: 91 m, RECEIVER DEPTH: 305 m
FREQUENCY: 50 Hz

ARL:UT
AS-80-861-P
SRR-GA
3-6-80

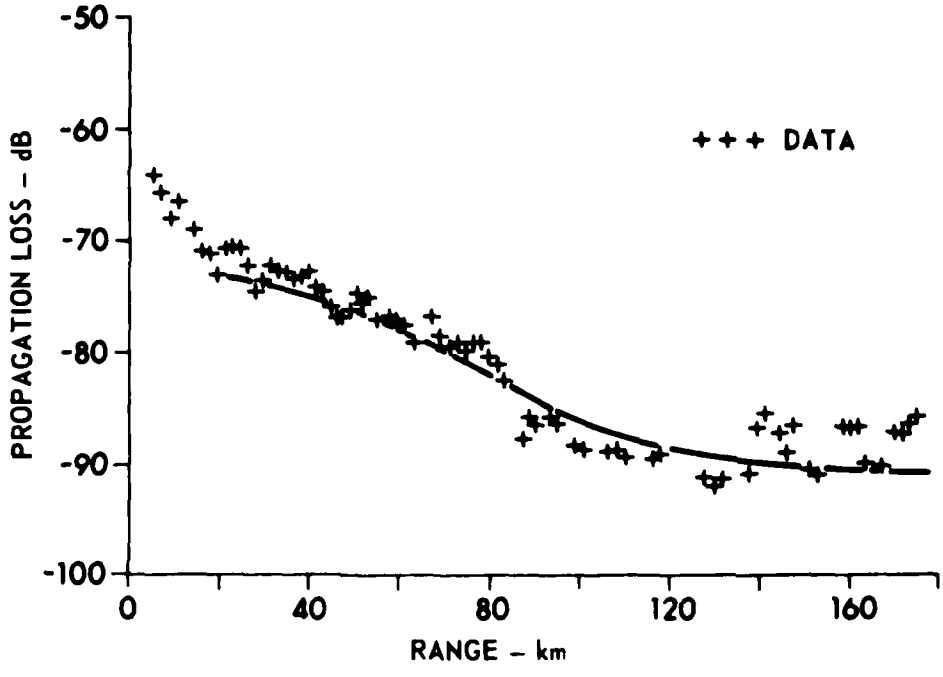

FIGURE II.9
COMPARISON OF DATA AND SMOOTHED
INCOHERENT PROPAGATION LOSS CURVE
SOURCE DEPTH: 91 m, RECEIVER DEPTH: 305 m
FREQUENCY: 50 Hz

ARL:UT
AS-80-862-P
SRR-GA
3-6-80

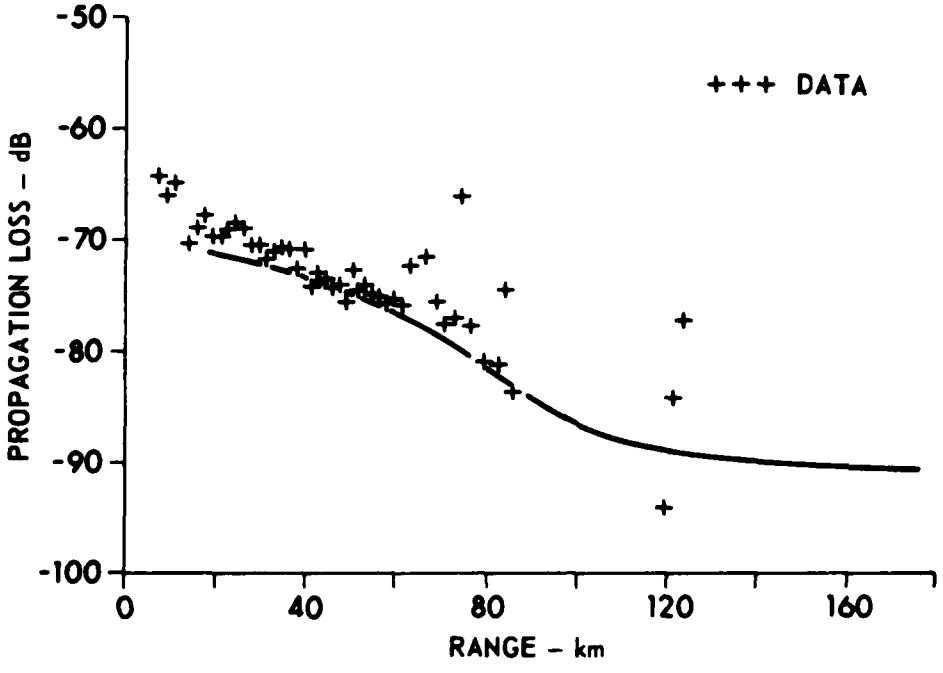

FIGURE II.10
COMPARISON OF DATA AND SMOOTHED
INCOHERENT PROPAGATION LOSS CURVE
SOURCE DEPTH: 91 m, RECEIVER DEPTH: 91 m
FREQUENCY: 50 Hz

ARL:UT
AS-80-863-P
SRR-GA
3-6-80

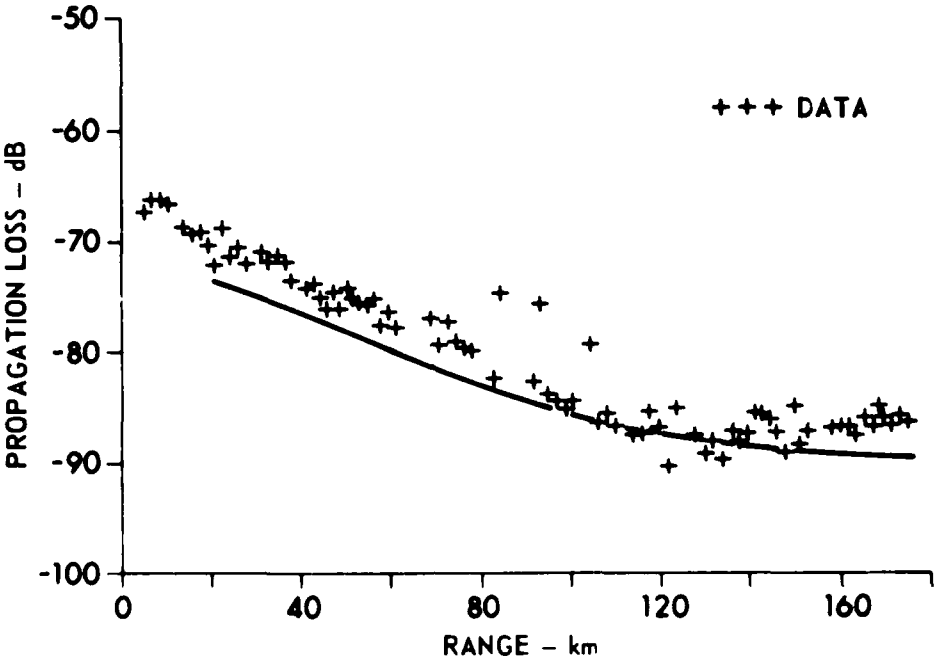

FIGURE II.11
COMPARISON OF DATA AND SMOOTHED
INCOHERENT PROPAGATION LOSS CURVE
SOURCE DEPTH: 91 m, RECEIVER DEPTH: 18 m
FREQUENCY: 50 Hz

ARL UT
AS-80-864-P
SRR-GA
3-6-80

portions of Fig. II.10 agree fairly well and the calculations show the rolloff that occurs near 80 km where the sloping bottom region begins. In Fig. II.11 the agreement is not as good as in the previous two cases. The calculations seem to be biased downward from the data by about 2 dB. There is reason to suspect that the receiver depth for this data set is incorrect, which might easily account for the apparent bias between the data and calculations.

The examples discussed in this section have compared model calculations with propagation loss from experimental data. In the next chapter, which explores the sensitivity of upslope and downslope propagation to sediment attenuation, additional examples of calculations using ADIAB will be presented.

CHAPTER III

A STUDY OF UPSLOPE AND DOWNSLOPE ACOUSTIC PROPAGATION

The purpose of this chapter is to report on the results of a sensitivity study of the effects of sediment attenuation on upslope and downslope acoustic propagation and to identify the important bottom interaction mechanisms. In the past, similar investigations[15] have been undertaken. These studies have, however, relied on modeling methods that employed a relatively crude description of the bottom. For example, in Ref. 15 the phenomena of slope enhancement were studied using the parabolic equation (PE)[16-19] and the Trimain ray[20] trace models. Both of these models use a restrictive description of the bottom involving a critical angle below which there is zero loss and above which there is some constant loss. The work reported in this chapter will delve deeper into the role played by sediment attenuation and will describe the bottom in much greater detail.

The modeling tool to be used to investigate attenuation effects in upslope and downslope propagation is the adiabatic normal mode model described in Chapter II. The upslope and downslope propagation geometries are shown in Fig. III.1 and III.2. The source position is at r=0 and $z=z_o$, and the bathmetric variations, assumed to be linear, occur between r_1 and r_2. The substrate is assumed to have solid properties and follows the water-sediment bathymetry at a depth of 200 m.

To isolate the attenuation and sloping bottom effects from any other bottom interaction effects, the following waveguide sound speed profile was assumed. The water waveguide sound speed profile was held constant in range and was truncated as the water depth varied from deep to shallow. This profile is illustrated in detail in Fig. II.5. The sound speed was taken to be continuous across the water-sediment interface and was assumed

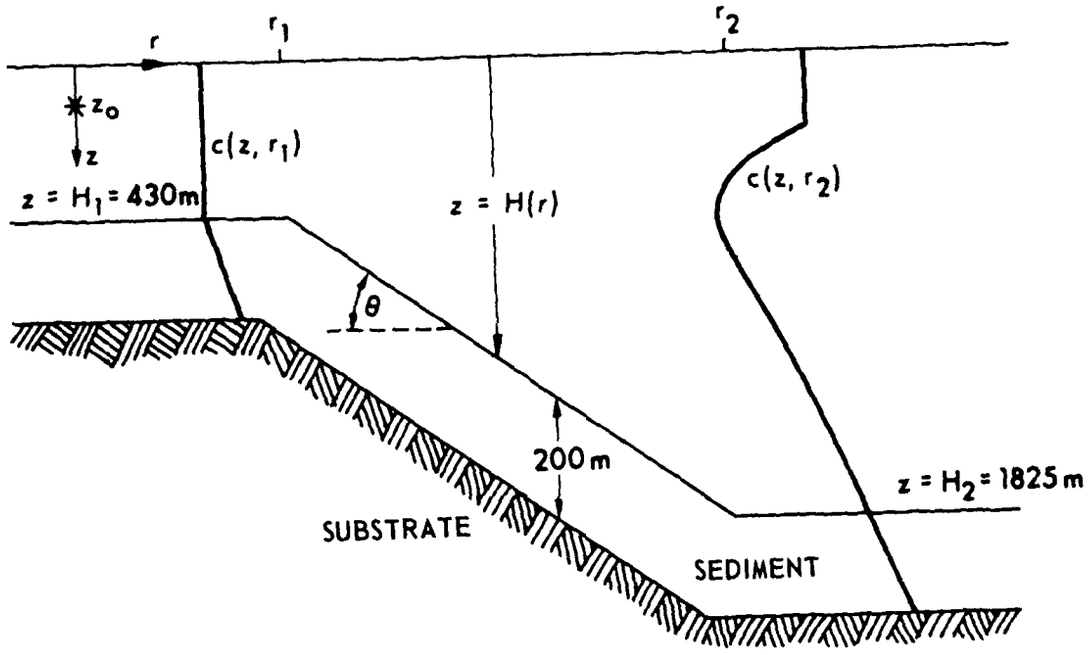

FIGURE III.1
DOWNSLOPE PROPAGATION GEOMETRY

ARL:UT
AS-80-792-P
SRR-GA
2-21-80

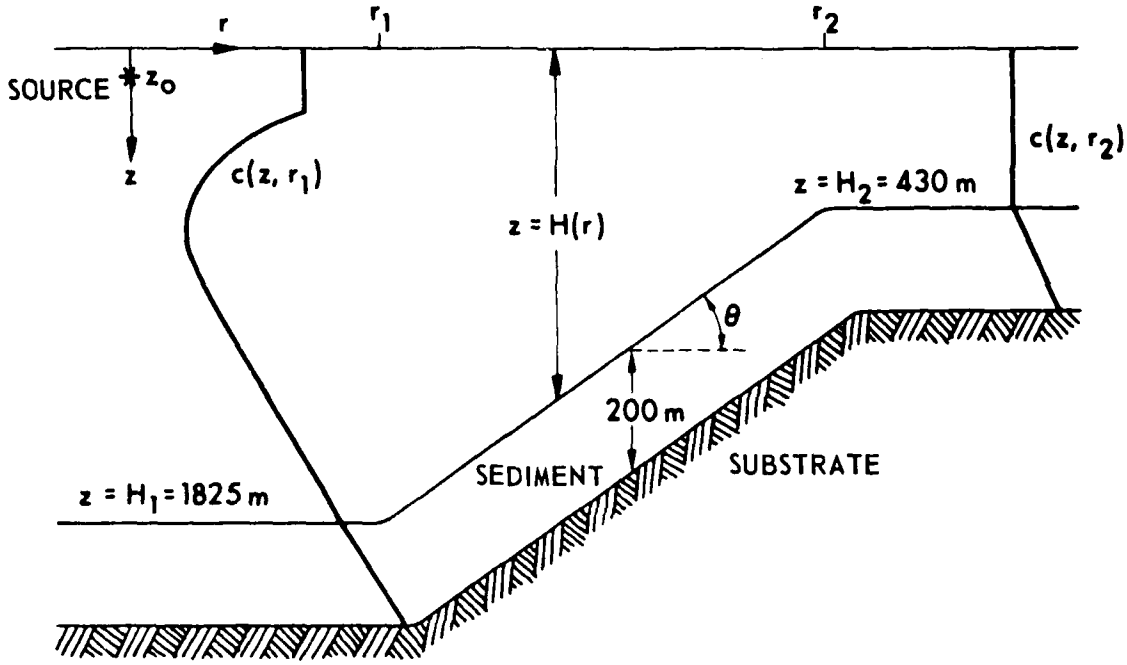

FIGURE III.2
UPSLOPE PROPAGATION GEOMETRY

ARL:UT
AS-80-807-P
SRR - GA
2 - 21 - 80

to increase linearly with depth into the sediment with a gradient of 1 sec^{-1}. The substrate, which began at a depth of 200 m below the water-sediment interface, was assumed to have a density of 2.7 g/cm^3 and constant shear and compressional wave velocities of 2700 and 5000 m/sec, respectively. The substrate shear and compressional wave attenuations were taken to be 0.2 and 0.03 dB/m/kHz, respectively. The sediment, which was treated as a fluid, of density 1.4 g/cm^3, was assumed to have an attenuation that was constant in depth and range. The values of sediment attenuation were selected from a range of values[21,22] appropriate for a high porosity sediment. Other questions concerning lateral sediment variability along the slope were deferred to later investigations.

A. Downslope Propagation

1. Basic Mechanism

The basic mechanisms involved in acoustic propagation in a horizontally stratified waveguide are: spreading loss, attenuation loss due to bottom interaction effects, and intermode phasing effects. For a range variable bathymetry, an additional mechanism must be considered. This mechanism has been called the megaphone and inverse megaphone effect and is related to the changing acoustic energy density that accompanies bathymetry changes. In downslope propagation this mechanism will act to produce additional loss and will be referred to as renormalization loss (RL) in this section. The term renormalization is used because the megaphone effects can conveniently be thought of in terms of changes in the normalization of the normal mode depth function that arise because of bathymetry changes.

In an isovelocity waveguide with perfect, sloping boundaries, the mode depth function normalization factor is proportional to $H^{-1/2}$, where H is the local water depth. In the more general case involving penetrable boundaries, the normalization factor will be approximately proportional to $H_{eff}^{-1/2}$, where H_{eff} is an effective interval between

which the majority of the modal energy is contained. This effective interval will be approximately the difference between mode turning points.

To illustrate the concept of renormalization loss, consider Fig. III.3. Figure III.3 depicts propagation loss versus depth for two ranges computed for the waveguide of Fig. III.1. In this computation the slope begins at range r_1 = 70 km and ends at r_2 = 160 km. The initial water depth is 430 m and the final water depth is 1825 m. The slope angle is about 1° and the frequency is 50 Hz. All attenuations are set to zero and the mode sums are done incoherently so that only spreading loss and renormalization loss mechanisms are active. The spreading loss between the two ranges of 65 and 200 km is given by

$$SL = 10 \log\left(\frac{200}{65}\right) = 4.88 \text{ dB} \quad .$$

The renormalization loss can be estimated by assuming that the acoustic energy is effectively confined between the surface and substrate interfaces. With this assumption the RL is given by

$$RL \approx 10 \log\left(\frac{2025}{630}\right) = 5.07 \text{ dB} \quad ,$$

and the total loss between the two ranges is given by

$$SL + RL \approx 10 \text{ dB} \quad .$$

This result appears to be consistent with the difference between the two curves of Fig. III.3.

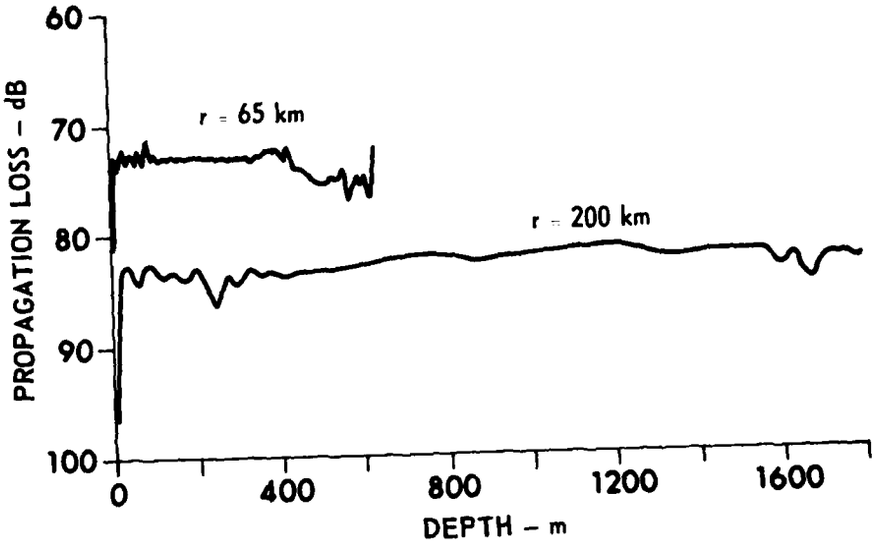

FIGURE III.3
DOWNSLOPE PROPAGATION LOSS versus DEPTH
FOR RANGES OF 65 AND 200 km
SEDIMENT ATTENUATION: 0 dB/m/kHz, SOURCE DEPTH: 91 m
BOTTOM SLOPE: 1°, FREQUENCY: 50 Hz

ARL:UT
AS-80-851-P
SRR-GA
2-27-80

2. Attenuation Effects

Figures III.4-III.7 depict the computed propagation loss versus range for the waveguide geometry of Fig. III.1. Three curves corresponding to sediment attenuations of 0, 0.025, and 0.070 dB/m/kHz are presented on each figure. These attenuation values span a range[21,22] appropriate for a high porosity sediment. Figures III.4 and III.5 consider a 1° bottom slope and receiver depths of 91 and 400 m, respectively, while Figs. III.6 and III.7 consider a 3° slope with the same receiver depths. For all four plots the source is fixed in the shallow water at zero range and a depth of 91 m. The edge of the slope begins at r_1 = 70 km and ends at about r_2 = 160 km for the 1° slope and at about r_2 = 97 km for the 3° slope.

One factor common to all four of the previously described plots is the increased sensitivity of the propagation loss to the sediment attenuations in the deep water regions ($r \gtrsim 120$ km). This increased sensitivity can be attributed to the changing character of the normal mode depth functions with range and is strongly dependent on source and receiver depths. For this reason the behavior of the plots in Fig. III.4-III.7 will be discussed in detail next, and the effects due to different source-receiver depths will be discussed later.

As mentioned above, the increased sensitivity to the sediment attenuation in the deep water regions is due to the changing character of the mode depth functions. The deep water sound speed profile is shown again in Fig. III.8. The profiles for the shallow water regions were obtained by truncating this profile at the appropriate depth. Simply stated, the increased sensitivity to attenuation for the source-receiver depths occurs because the deep water sound field is dominated by a different set of normal modes than the shallow water field. To see how this arises consider Figs. III.9 and III.10. Figure III.9 depicts the normal mode depth function of mode 1 in the shallow water region, and Fig. III.10 depicts mode 1 in the deep water region. In the shallow water region, mode 1 is a dominant mode because it interacts least with the bottom.

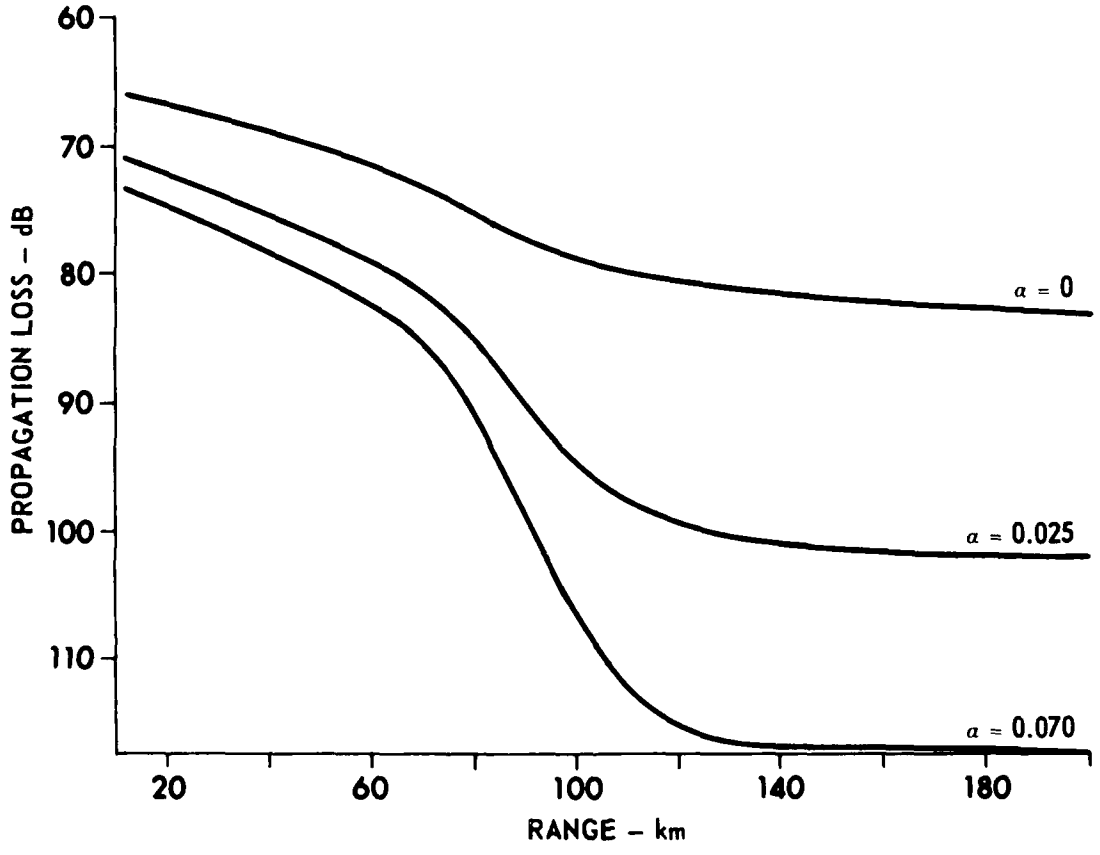

FIGURE III.4
DOWNSLOPE PROPAGATION LOSS versus RANGE FOR SEDIMENT ATTENUATIONS OF 0, 0.025, AND 0.070 dB/m/kHz
SOURCE DEPTH: 91 m, RECEIVER DEPTH: 91 m
BOTTOM SLOPE: 1°

ARL:UT
AS-80-796-P
SRR-GA
2-21-80

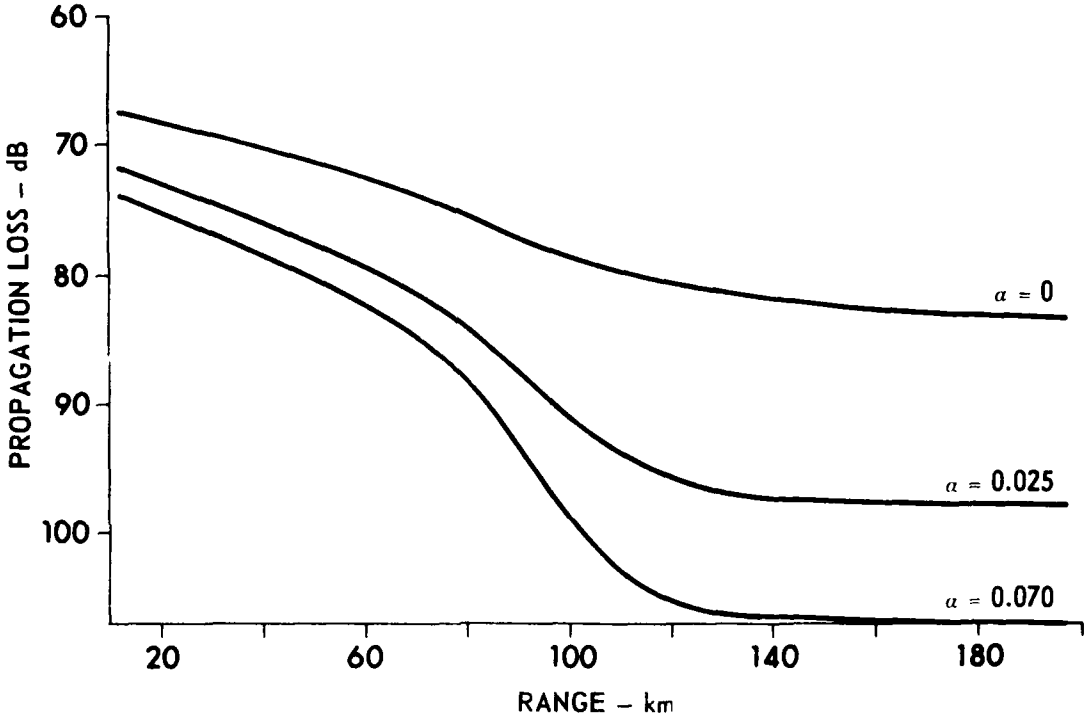

FIGURE III.5
DOWNSLOPE PROPAGATION LOSS versus RANGE FOR SEDIMENT ATTENUATIONS OF 0, 0.025, AND 0.070 dB/m/kHz

SOURCE DEPTH: 91 m, RECEIVER DEPTH: 400 m
BOTTOM SLOPE: 1°

ARL:UT
AS-80-795-P
SRR-GA
2-21-80

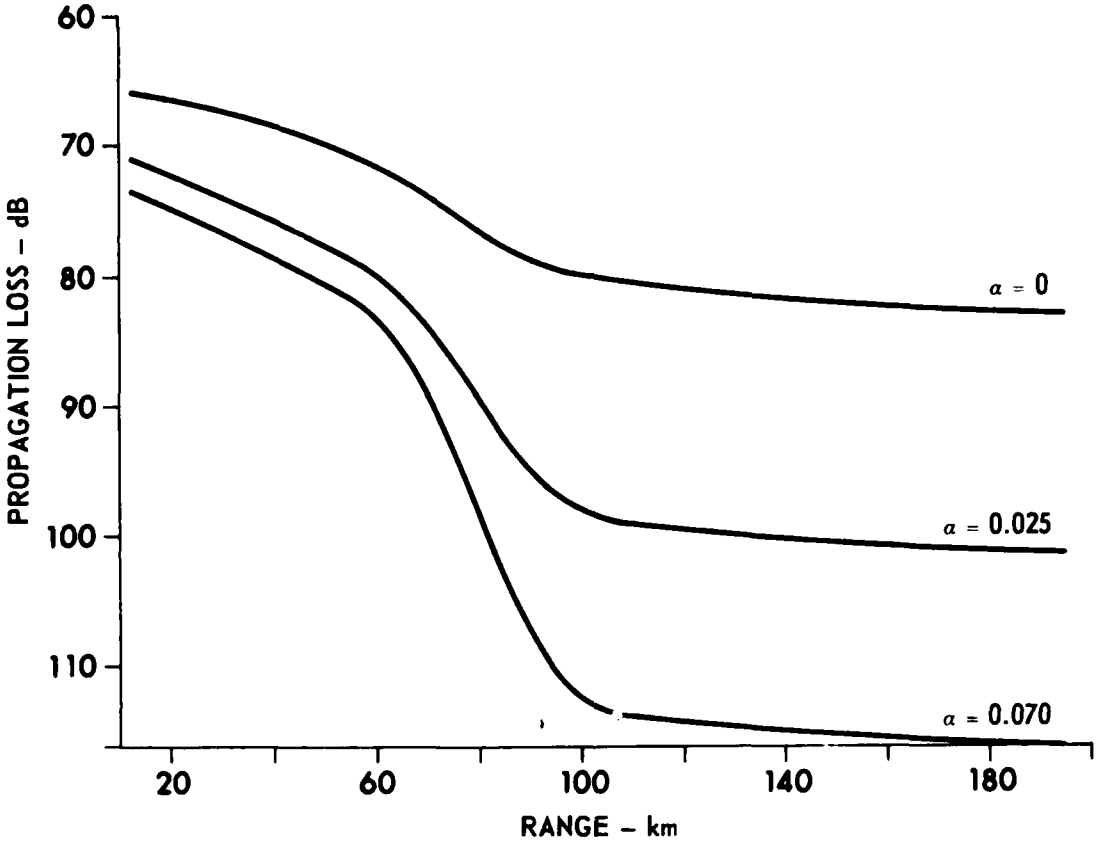

FIGURE III.6
DOWNSLOPE PROPAGATION LOSS versus RANGE FOR SEDIMENT ATTENUATIONS OF 0, 0.025, AND 0.070 dB/m/kHz

SOURCE DEPTH: 91 m, RECEIVER DEPTH: 91 m
BOTTOM SLOPE: 3°

ARL:UT
AS-80-793-P
SRR-GA
2-21-80

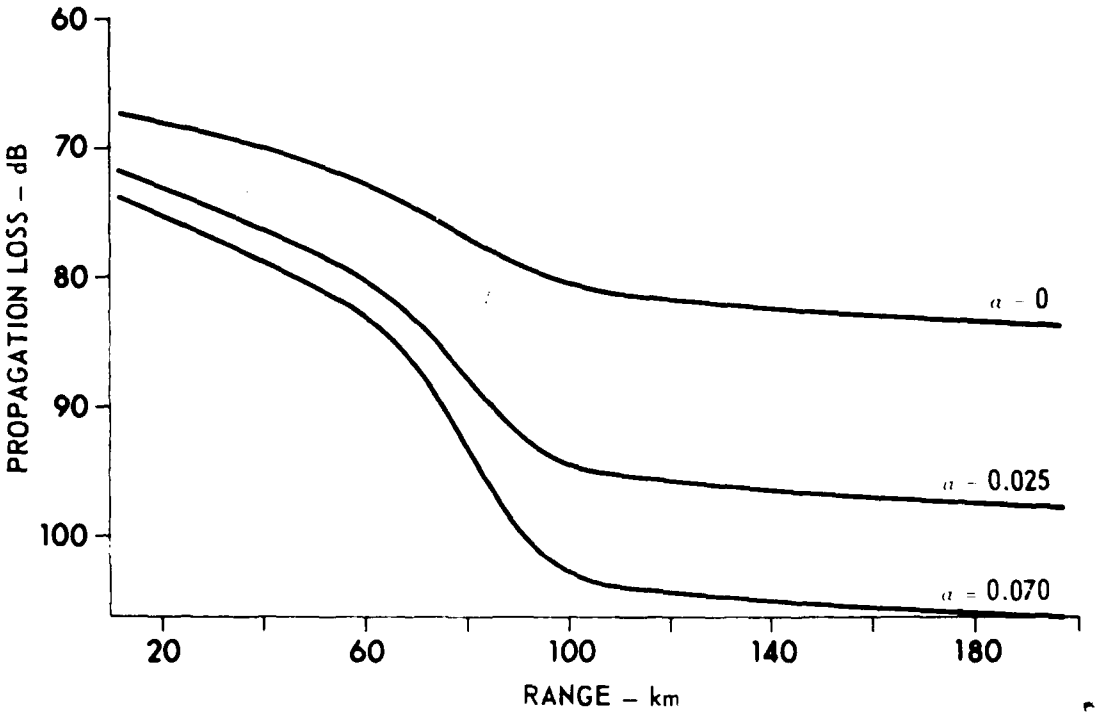

FIGURE III.7
DOWNSLOPE PROPAGATION LOSS versus RANGE FOR SEDIMENT ATTENUATIONS OF 0, 0.025, AND 0.070 dB/m/kHz

SOURCE DEPTH: 91 m, RECEIVER DEPTH: 400 m
BOTTOM SLOPE: 3°

ARL:UT
AS-80-794-P
SRR-GA
2-21-80

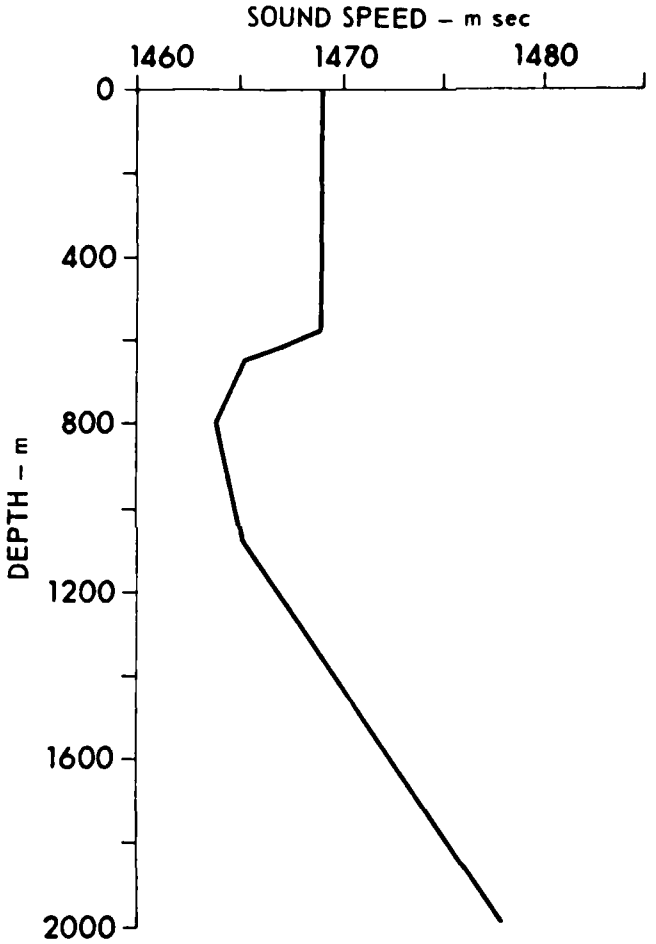

FIGURE III.8
DEEP WATER SOUND SPEED versus DEPTH

ARL:UT
AS-80-850-P
SRR-GA
2-27-80

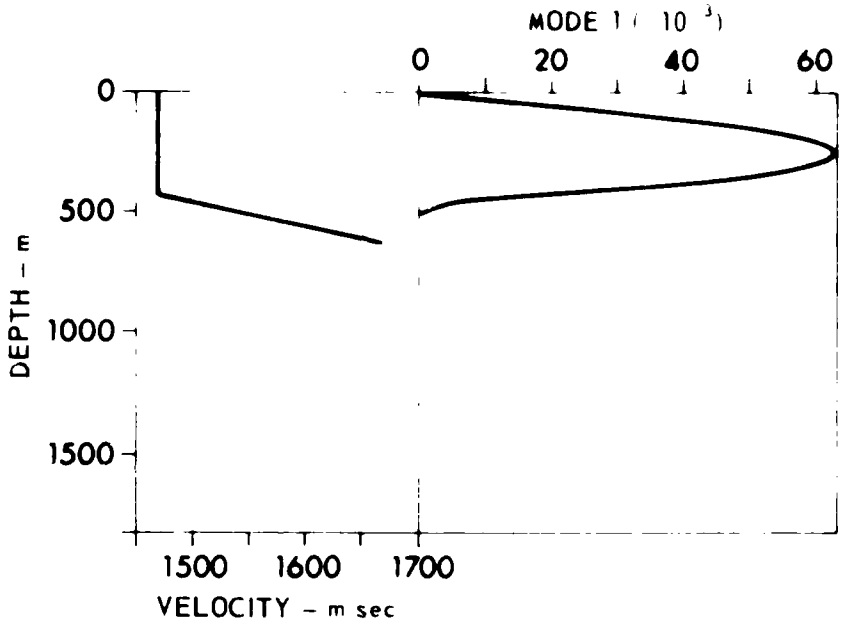

FIGURE III.9
SHALLOW WATER SOUND SPEED PROFILE AND MODE FUNCTION FOR MODE NUMBER 1
FREQUENCY 50 Hz

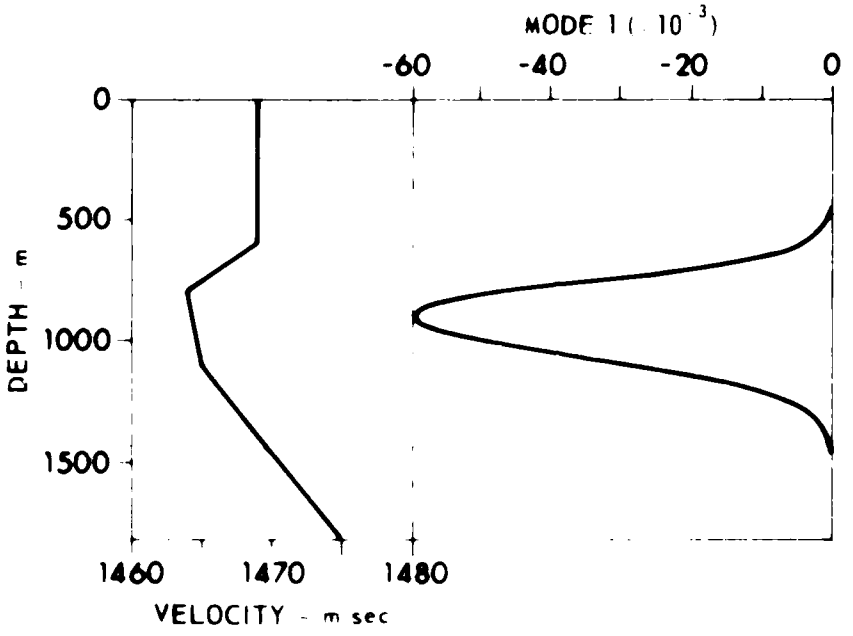

FIGURE III.10
DEEP WATER SOUND SPEED PROFILE AND MODE FUNCTION FOR MODE NUMBER 1
FREQUENCY - 50 Hz

ARL UT
AS-80-848-P
SRR-GA
2-27-80

Following mode 1 into the deep water, one would expect it to remain a dominant mode since it would have suffered less attenuation as it propagated through the shallow water. This, however, does not occur when the receiver is located at a shallow depth because mode 1 is evanescent at shallow depths. Therefore, even though mode 1 was dominant in the shallow water, it does not contribute to the field in the deep water because of its changed character. This type of behavior is experienced to some extent by all the dominant shallow water modes with the net result that the field in the deep water is dominated by a different set of modes that have been attenuated more and in a different manner than the shallow water dominant modes. Hence, it is not surprising that the sensitivity to attenuation varies from shallow to deep water. The previous analysis will of course depend on the water sound speed profile and its range behavior to some extent, but it is believed to be of general validity.

To better understand how the above picture changes with receiver depth, consider Figs. III.11 and III.12. These curves depict propagation loss versus depth for sediment attenuations of 0 and 0.025 dB/m/kHz and ranges of 75 and 200 km. A comparison of Figs. III.11 and III.12 shows that, over a wide range of potential receiver depths, the deep water field is more sensitive to an attenuation change than the shallow water field. The deep water profile at 200 km has a fully developed sound channel between about 600 and 1400 m with minimum loss at around 800 m. Note from Fig. III.12 that, as the receiver depth moves into the sound channel, the increased sensitivity in the deep water becomes less or becomes nonexistent. This behavior is not surprising since the shallow water dominant modes, which have the low mode numbers, are precisely those modes that become SOFAR deep water modes. Therefore, for receiver depths in the deep water SOFAR channel, the shallow water modes retain their dominance over the other modes in the deep water.

The influence of source depth on the sensitivity to attenuation is not expected to be significant, because the source is located in shallow water where the sound speed profile is essentially isovelocity,

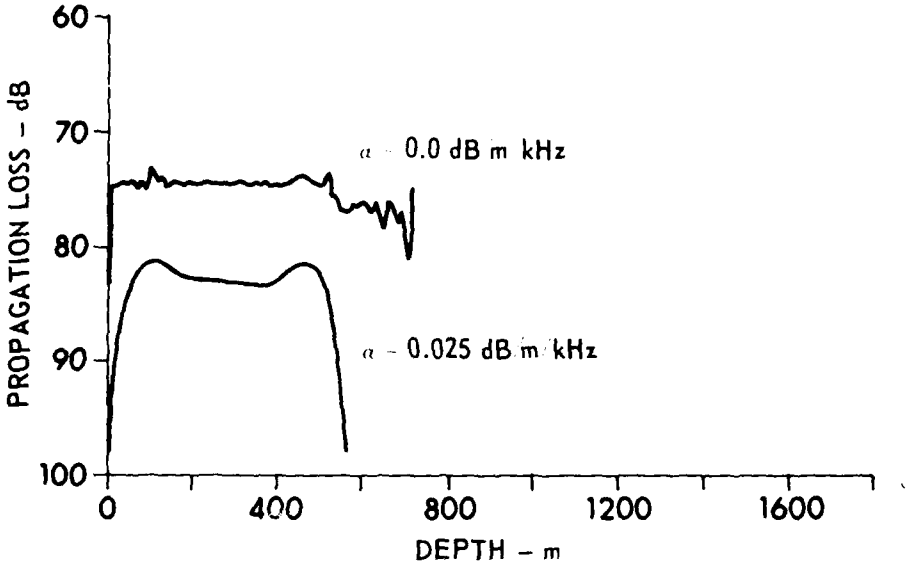

FIGURE III.11
DOWNSLOPE PROPAGATION LOSS versus DEPTH FOR SEDIMENT ATTENUATIONS OF 0 AND 0.025 dB/m/kHz
SOURCE DEPTH: 91 m, BOTTOM SLOPE: 1°
RANGE: 75 km, FREQUENCY: 50 Hz

ARL:UT
AS-80-847-P
SRR-GA
2-27-80

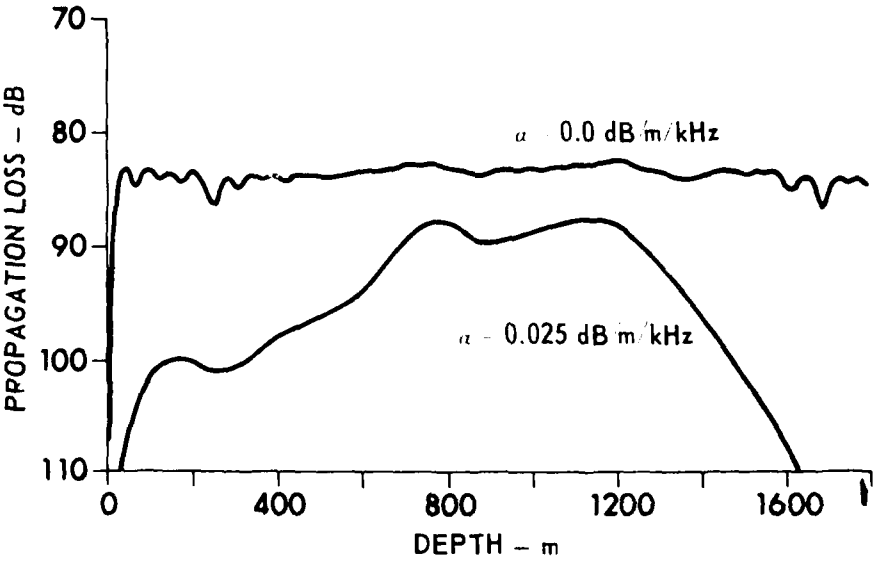

FIGURE III.12
DOWNSLOPE PROPAGATION LOSS versus DEPTH FOR SEDIMENT ATTENUATIONS OF 0 AND 0.025 dB/m/kHz
SOURCE DEPTH: 91 m, BOTTOM SLOPE: 1°
RANGE: 200 km, FREQUENCY: 50 Hz

ARL:UT
AS-80-846-P
SRR-GA
2-27-80

and all the modes have turning points near or in the bottom. Hence, all the modes have approximately equal amplitudes and are all equally likely to become excited.

An important conclusion to be drawn from the work concerning attenuation effects is that, when attempting to model acoustic data for downslope propagation, one must use the most accurate description of the shallow water attenuation profile that is available. This conclusion is based on the previous findings that show increased sensitivity to attenuation in deep water regions. For example, the behavior shown in Figs. III.4-III.7 indicates that a small error or change in the attenuation might produce negligible changes in the shallow water field while giving rise to substantial changes in the deep water field. This line of thought also points to the importance of as accurate a representation of the depth variation of the shallow water attenuation as possible, since the details of the depth variation of the sediment attenuation profile (particularly the deeper portions), while being insignificant in the shallow water regions, could conceivably become important as the dominant mode groups vary from shallow to deep water.

3. Slope Angle Effects

In this subsection the effects of bottom slope angle on propagation loss will be described. The waveguide model is the same one used throughout the previous discussions except that bottom slope angles have been varied. In all cases the slope begins at r_1 = 70 km (see Fig. III.1).

Figures III.13 and III.14 show incoherent propagation loss versus range for receiver depths of 91 and 400 m. The source depth and attenuation for both figures are 91 m and 0 dB/m/kHz, respectively. Two curves are shown in each figure, one for a bottom slope of 1° and one for 3°. In the shallow (short ranges) and deep (long ranges) water regions the curves for both slopes coincide. In the range regions where the water depth is changing, the 1° curves show less loss than the 3° curves. This behavior occurs because renormalization loss for the 1° bottom slope

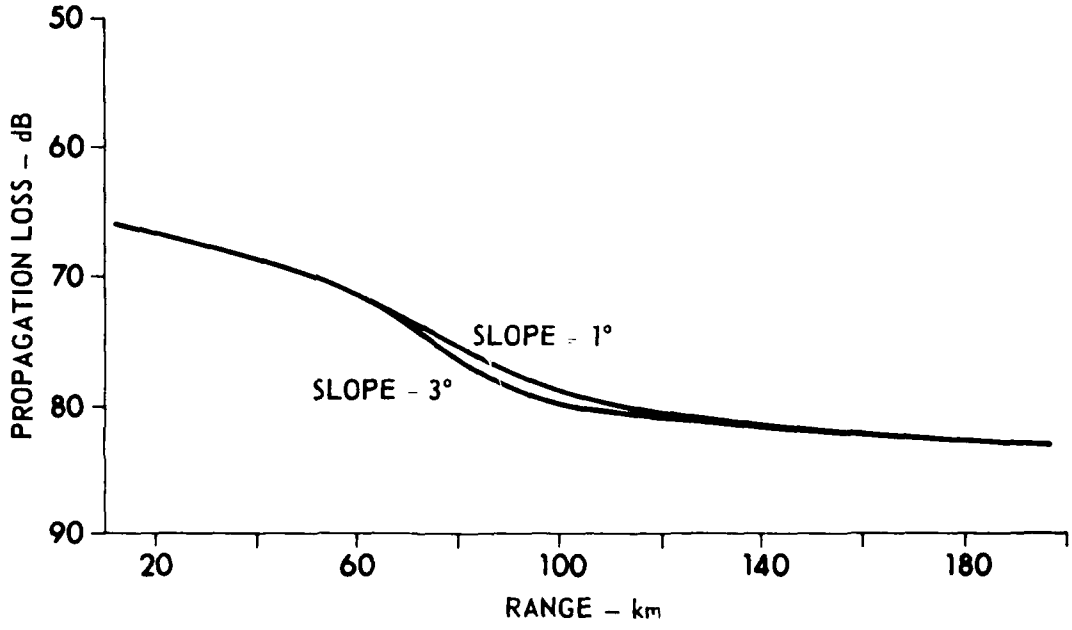

FIGURE III.13
DOWNSLOPE PROPAGATION LOSS versus RANGE
FOR BOTTOM SLOPES OF 1 AND 3°
SOURCE DEPTH: 91 m, RECEIVER DEPTH: 91 m
SEDIMENT ATTENUATION: 0 dB/m/kHz

ARL:UT
AS-80-800-P
SRR-GA
2-21-80

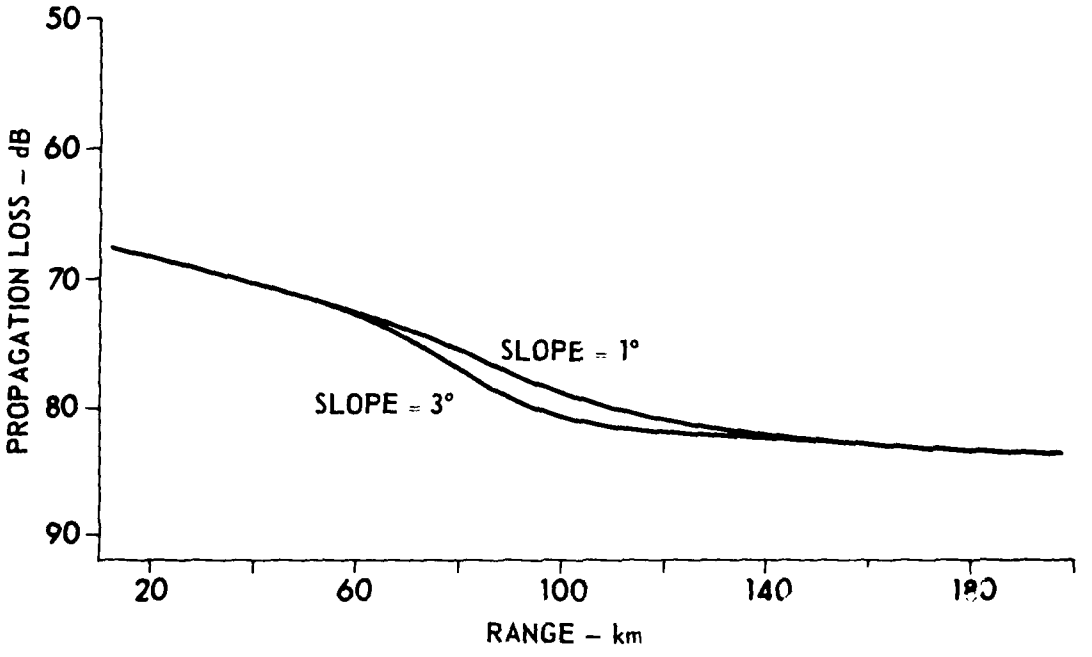

FIGURE III.14
DOWNSLOPE PROPAGATION LOSS versus RANGE
FOR BOTTOM SLOPES OF 1 AND 3°
SOURCE DEPTH: 91 m, RECEIVER DEPTH: 400 m
SEDIMENT ATTENUATION: 0 dB/m/kHz

ARL:UT
AS-80-799-P
SRR-GA
2-21-80

lags that for the 3° slope since the water depth is changing more slowly. The curves merge in the shallow and deep water regions since the water depths are the same in these regions.

Figures III.15 and III.16 are the same as Figs. III.13 and III.14 except that sediment absorption has been added. A sediment attenuation of 0.025 dB/m/kHz was used. The curves for bottom slopes of 1° and 3° again merge in the shallow water regions. As propagation over the slope begins, the 1° curve lies above the 3° curve; however, as the range increases the two curves intersect and the 1° curve falls below the 3° curve. This behavior occurs because the region of significant bottom interaction along the 1° slope is of greater extent than that along the 3° slope, i.e., the attenuation in propagating over a 1° slope surpasses that in propagating over a 3° slope. The curves in Figs. III.15 and III.16 indicate that the transmission of acoustic energy from shallow water into deep water is not too sensitive to bottom slope angle. The propagation loss shows differences over the slope regions, but the deep water propagation loss is little affected. As another illustration of this point, consider Fig. III.17, which shows the propagation loss versus depth at a range of 200 km for slope angles of 1° and 3°. Note the total insensitivity to bottom slope in the deep sound channel between 600 and 1400 m. The only effects are seen at the shallow and deep depths because the bottom interacting modes contribute more heavily to the field at these depths.

4. Level of Detail

The final topic with regard to downslope propagation concerns the level of detail with which one must describe the properties of the sloping bottom. Or more specifically, how far along the slope do the bottom properties have to be accurately described? The answer to this question is a measure of when acoustic bottom interaction along the slope ceases to be the driving mechanism influencing the field. This question is addressed in a rudimentary way in the following discussion.

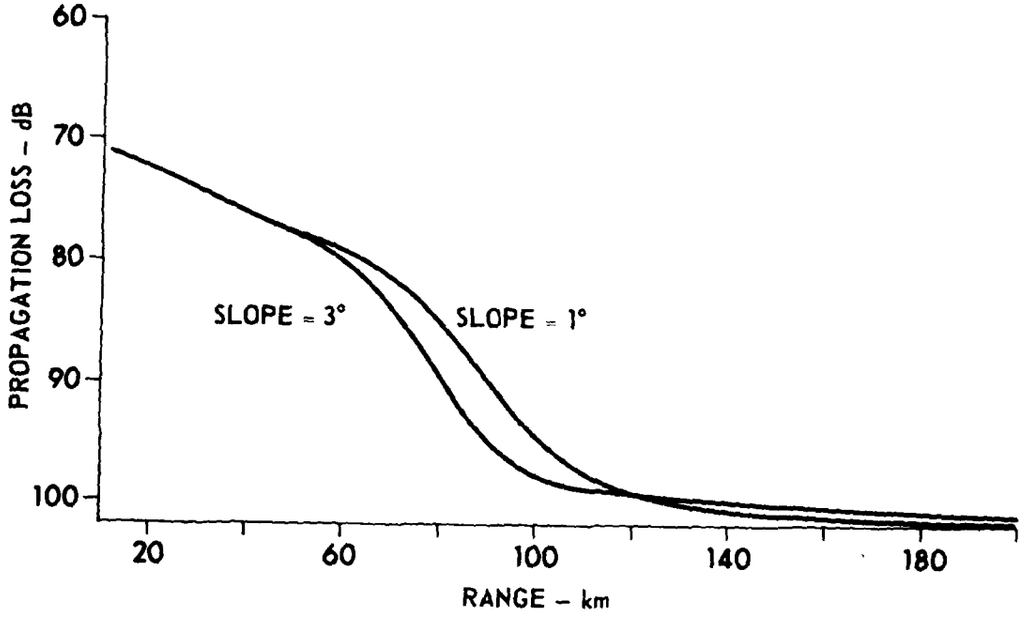

FIGURE III.15
DOWNSLOPE PROPAGATION LOSS versus RANGE FOR BOTTOM SLOPES OF 1 AND 3°
SOURCE DEPTH: 91 m, RECEIVER DEPTH: 91 m
SEDIMENT ATTENUATION: 0.025 dB/m/kHz

ARL:UT
AS-80-797-P
SRR-GA
2-21-80

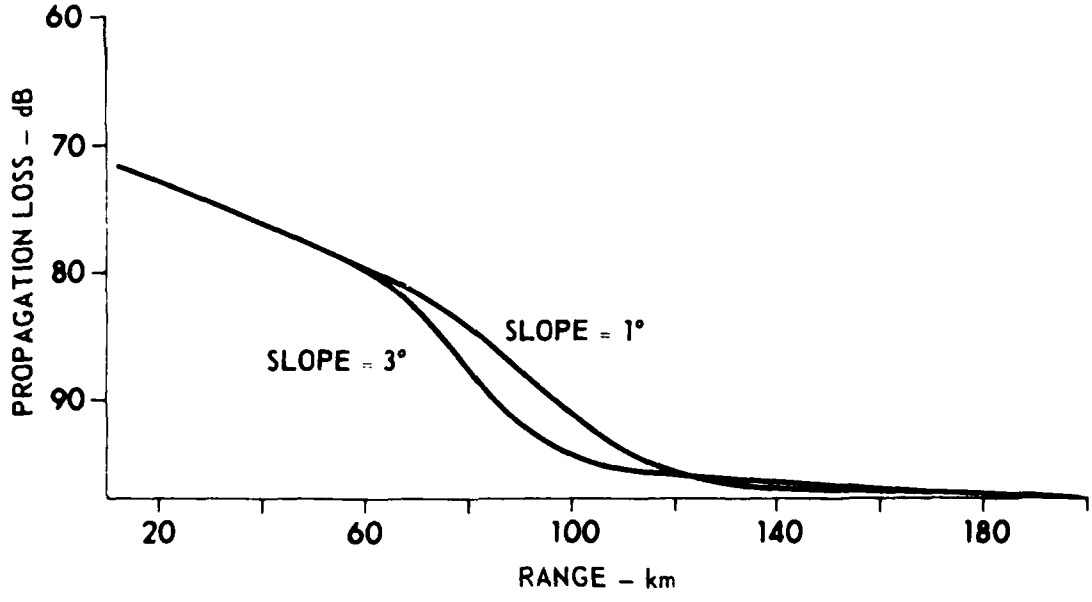

FIGURE III.16
DOWNSLOPE PROPAGATION LOSS versus RANGE
FOR BOTTOM SLOPES OF 1 AND 3°
SOURCE DEPTH: 91 m, RECEIVER DEPTH: 400 m
SEDIMENT ATTENUATION: 0.025 dB/m/kHz

ARL:UT
AS-80-798-P
SRR-GA
2-21-80

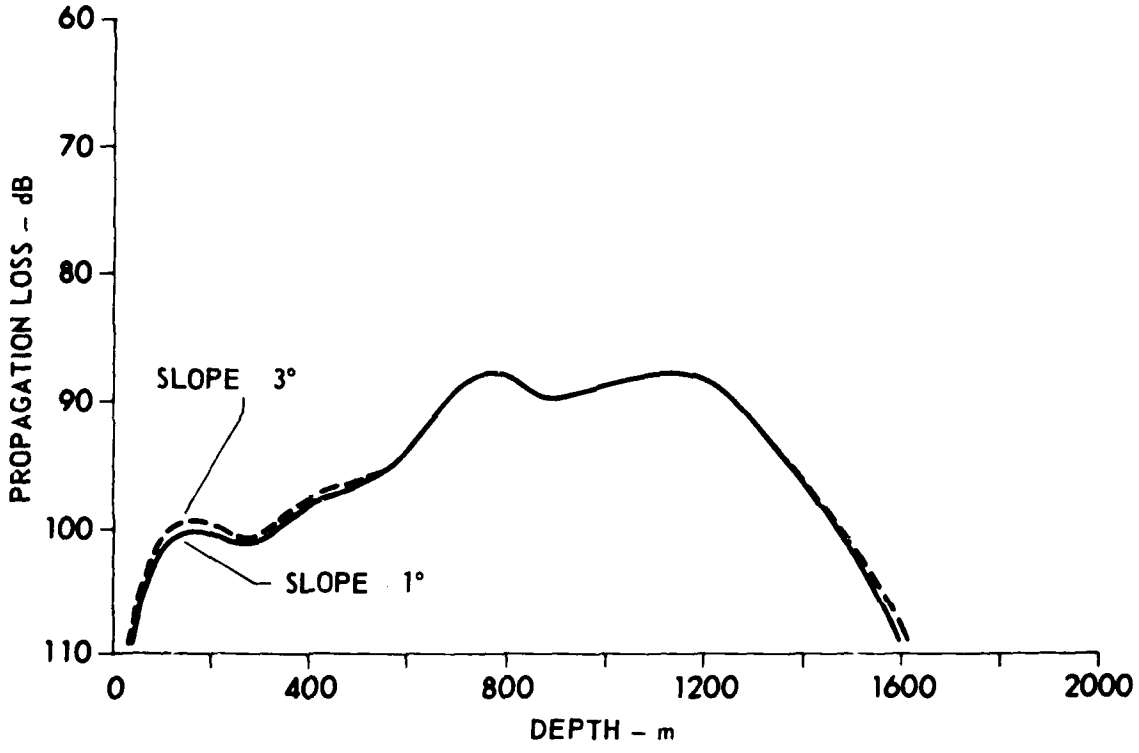

FIGURE III.17
DOWNSLOPE PROPAGATION LOSS versus DEPTH
FOR BOTTOM SLOPES OF 1 AND 3°
SEDIMENT ATTENUATION: 0.025 dB/m/kHz
SOURCE DEPTH: 91 m, RANGE. 200 km

ARL:UT
AS-80-802-P
SRR-GA
2-21-80

Figure III.18 depicts propagation loss versus range for a bottom slope of 1° and sediment attenuations of 0.025 and 0.070 dB/m/kHz. The source and receiver depths are 91 and 400 m, respectively. The circles represent attempts to predict the propagation loss at longer ranges from the known value at shorter ranges, assuming spreading loss and renormalization loss only. For example, if the loss at 100 km were 110 dB, the projected loss at 115 km would be given by

$$110 \text{ dB} + 10 \log \frac{115}{100} + \text{RL} \quad ,$$

where the RL is estimated assuming the acoustic energy is contained between the surface and range variable substrate.

The reason for making these projections is that, when the projected values of propagation loss begin to accurately predict the computed field, this indicates that the attenuation due to bottom interaction is no longer playing an important role. Figure III.18 shows that between 110 and 125 km the projected propagation loss values begin to follow the character of the computed curves but are biased slightly downward. An examination of the water profile and the truncation procedure reveals that between 115 and 125 km the profile is beginning to support SOFAR and RSR types of propagation as the sound channel is developed. That the projections begin to track the calculations past 125 km is not surprising, since the SOFAR and RSR modes of propagation that become possible are not strongly bottom interacting. The uniform downward bias of the projections at the longer ranges is most likely due to a systematic error induced by assuming the energy to be contained between the surface and substrate along the slope. In the slope region the bottom interacting energy is being stripped away and the energy transport is occurring higher in the waveguide.

Thus, one can conclude that the formation of the sound channel seems to mark the point along a slope at which bottom interaction ceases to be important. This conclusion seems intuitively correct and can

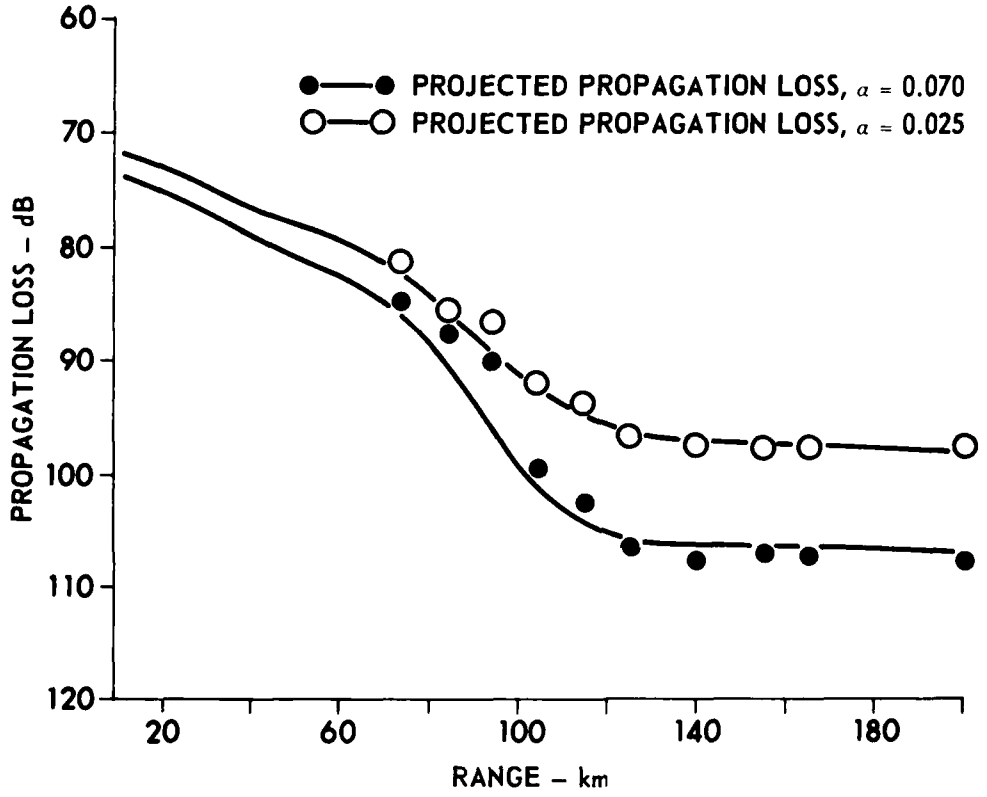

FIGURE III.18
DOWNSLOPE PROPAGATION LOSS versus RANGE FOR SEDIMENT ATTENUATIONS OF 0.025 AND 0.070 dB/m/kHz
SOURCE DEPTH: 91 m, RECEIVER DEPTH: 400 m
BOTTOM SLOPE: 1°

ARL:UT
AS-80-803-P
SRR-GA
2-21-80

easily be checked. To do so the solid curves in Fig. III.18 were recomputed in the same manner as before but with the bottom attenuation set to zero for ranges greater than 120 km. The resulting curves were indistinguishable from those of Fig. III.18.

B. Upslope Propagation

In this section the upslope propagation of sound and its dependence on bottom attenuation are investigated. As in the previous section concerning downslope propagation, the basic mechanism involved in upslope propagation will be described and the sensitivity of propagation loss to bottom attenuation will be examined as well as its sensitivity to bottom slope angle.

1. Basic Mechanisms

The basic mechanisms involved in upslope propagation are the same ones that are involved in downslope propagation with the addition of one extra mechanism involving mode cutoff. As sound propagates upslope the horizontal wave numbers decrease with range until mode cutoff is reached. This occurs when the equivalent bottom angle of the mode reaches the critical angle for the perfect transmission of sound into the substrate. At this point the mode passes into the continuous spectrum and the energy associated with that mode is removed from the field since it radiates into the substrate and is lost. This additional loss mechanism is not present in downslope propagation. It should be emphasized at this time that any mode-mode coupling effects are being ignored. The inclusion of mode-mode coupling would allow modes nearing cutoff to couple some of their energy into modes with larger wave numbers which are still far from cutoff. This process would tend to reduce the energy lost due to mode cutoff processes. Past work[3,6,7] supports the idea that mode coupling effects might be small for slope angles of practical interest, and they will be ignored in the following treatment. More sophisticated ways to estimate the importance of mode

coupling and approximate ways to include their effects will be discussed in Chapter IV.

To illustrate the effects of mode cutoff, consider Fig. III.19, which shows the results of propagation loss versus depth for two ranges, 35 and 200 km. The waveguide model used to compute these curves is shown in Fig. III.2 with r_1 = 40 km and r_2 about 130 km. The source depth was taken to be 91 m, the sediment attenuation was set to zero, and a frequency of 50 Hz was used. All other aspects of the waveguide were the same as those in the previous section.

If one were to estimate the difference between the two curves of Fig. III.19, assuming a spreading loss and a gain due to renormalization, the expected difference would be

$$10 \log\left(\frac{200}{35}\right) - 10 \log\left(\frac{2025}{630}\right) \approx 2.5 \text{ dB} \quad .$$

The average difference between the two curves in Fig. III.19 is of the order of 5-7 dB and is considerably more than the expected 2.5 dB. This difference in propagation loss will be attributed to losses due to energy radiated into the substrate. Again, the reader is reminded that the inclusion of mode coupling could act to reduce the loss due to radiation into the substrate.

2. Attenuation Effects

Figures III.20-III.22 depict propagation loss versus range versus sediment attenuation for three different combinations of source-receiver depths. The bottom slope was taken to be 1° with the arrows on the range axis denoting the beginning and end of the slope. Figures III.20 and III.22 have source depths that are above and below the deep water sound channel, respectively. The source depth for Fig. III.21 is 1200 m which is in the deep water sound channel. Figures III.23-III.25 show the same curves as Figs. III.20-III.22 with the exception that the bottom

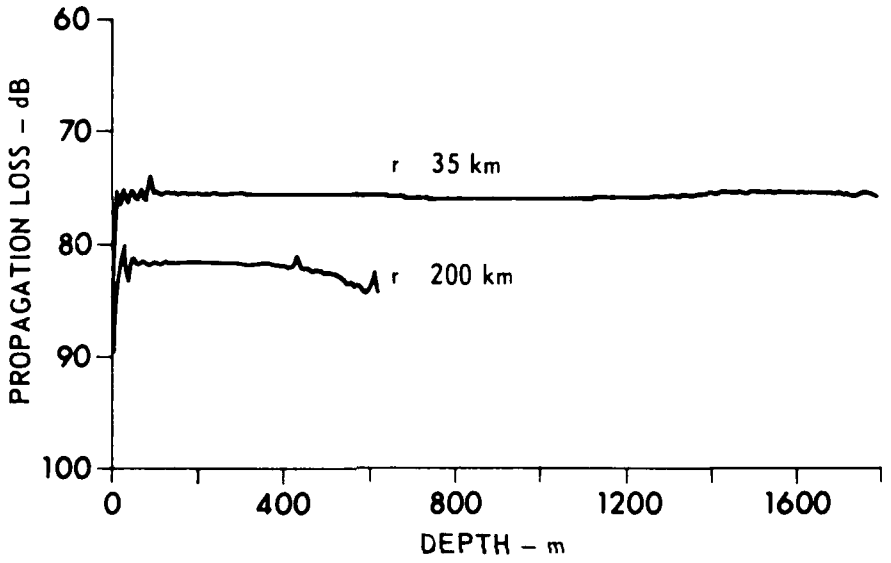

FIGURE III.19
UPSLOPE PROPAGATION LOSS versus DEPTH
FOR RANGES OF 35 AND 200 km

SEDIMENT ATTENUATION: 0 dB/m/kHz
SOURCE DEPTH: 91 m, BOTTOM SLOPE: 1°
FREQUENCY: 50 Hz

ARL:UT
AS-80-845-P
SRR-GA
2-27-80

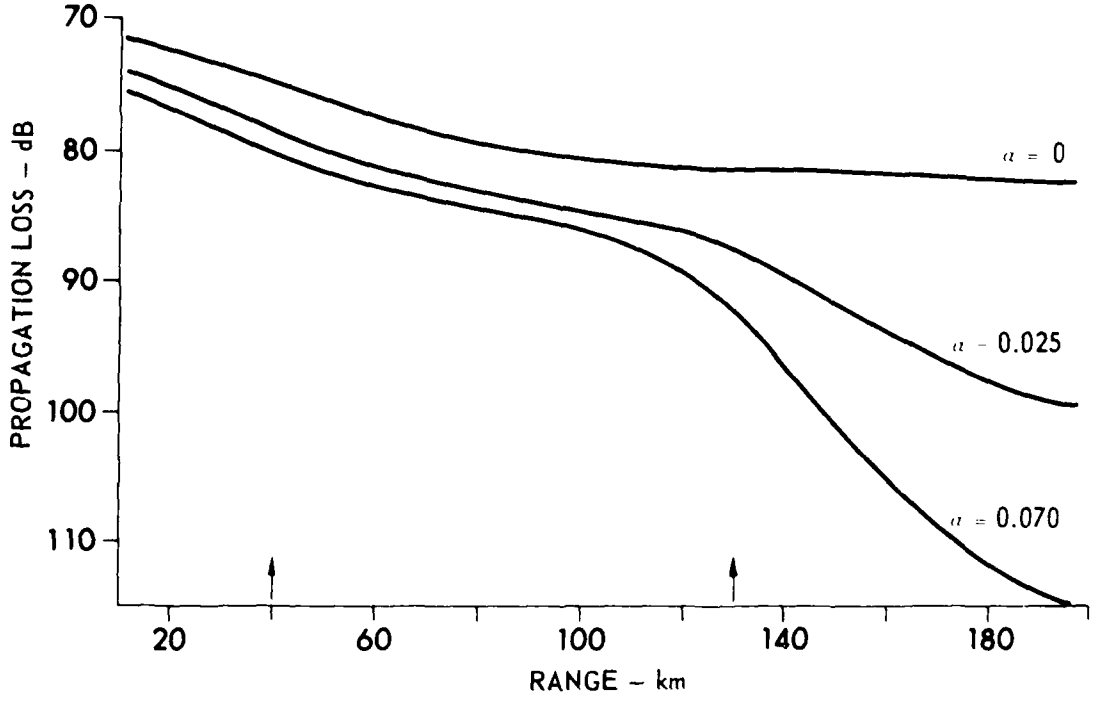

FIGURE III.20
UPSLOPE PROPAGATION LOSS versus RANGE FOR SEDIMENT ATTENUATIONS OF 0, 0.025, AND 0.070 dB/m/kHz
SOURCE DEPTH: 91 m, RECEIVER DEPTH: 91 m
BOTTOM SLOPE: 1°

ARL:UT
AS-80-813-P
SRR-GA
2-21-80

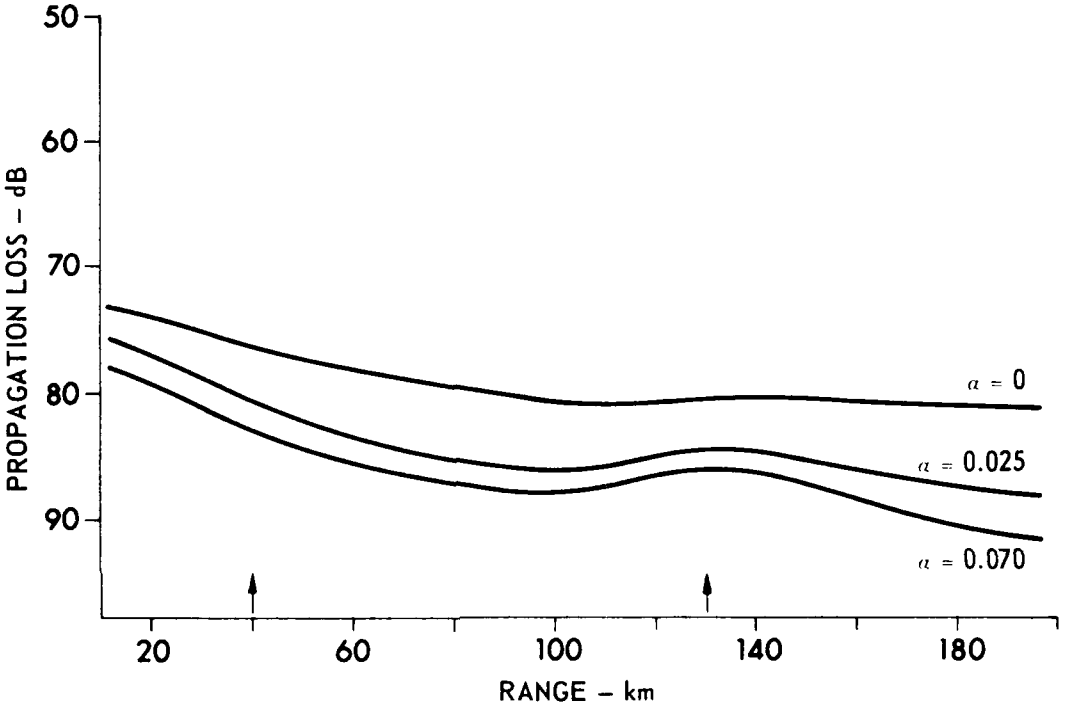

FIGURE III.21
UPSLOPE PROPAGATION LOSS versus RANGE FOR SEDIMENT ATTENUATIONS OF 0, 0.025, AND 0.070 dB/m/kHz
SOURCE DEPTH: 1200 m, RECEIVER DEPTH: 91 m
BOTTOM SLOPE: 1°

ARL:UT
AS-80-812-P
SRR-GA
2-21-80

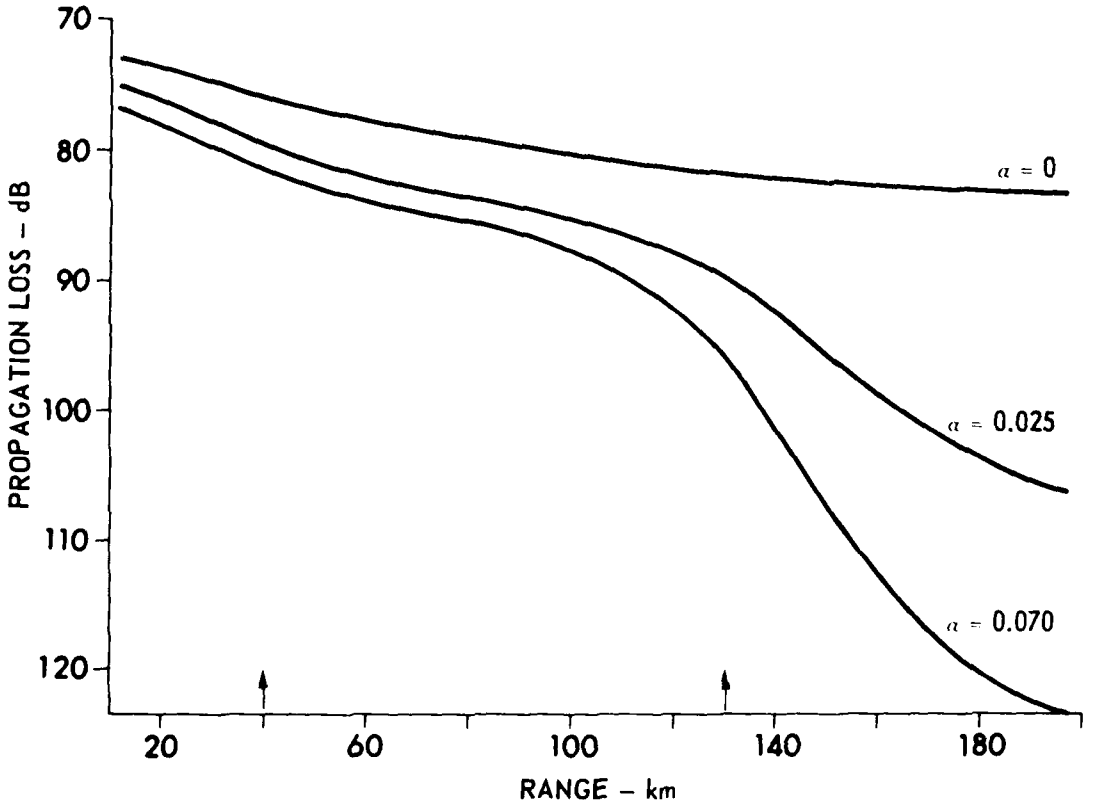

FIGURE III.22
UPSLOPE PROPAGATION LOSS versus RANGE FOR SEDIMENT ATTENUATIONS OF 0, 0.025, AND 0.070 dB/m/kHz

SOURCE DEPTH: 1600 m, RECEIVER DEPTH: 91 m
BOTTOM SLOPE: 1°

ARL:UT
AS-80-811-P
SRR-GA
2-21-80

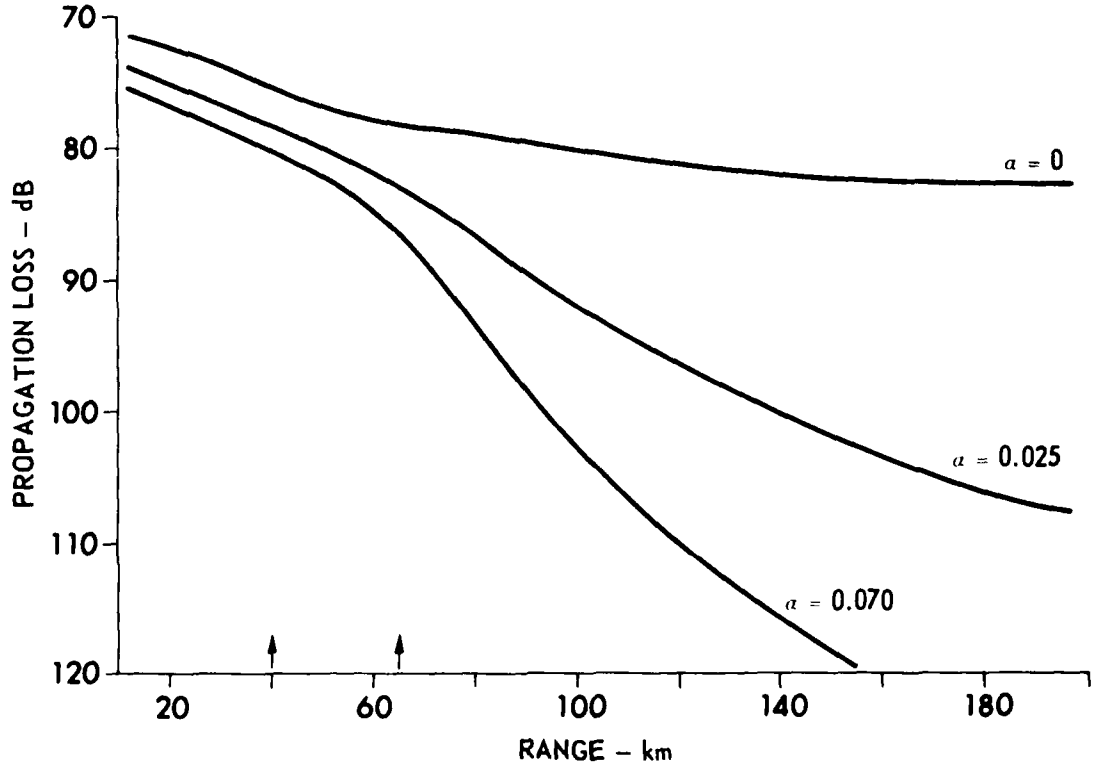

FIGURE III.23
UPSLOPE PROPAGATION LOSS versus RANGE FOR SEDIMENT ATTENUATIONS OF 0, 0.025, AND 0.070 dB/m/kHz
SOURCE DEPTH: 91 m, RECEIVER DEPTH: 91 m
BOTTOM SLOPE: 3°

ARL:UT
AS-80-810-P
SRR-GA
2-21-80

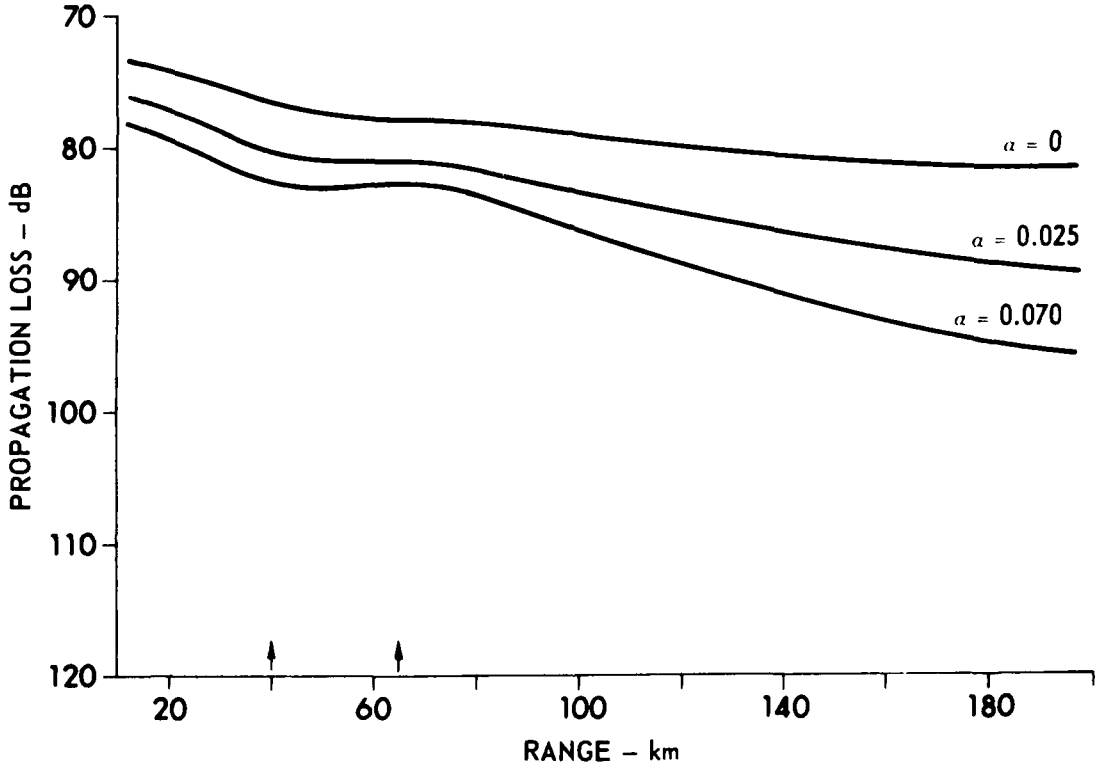

FIGURE III.24
UPSLOPE PROPAGATION LOSS versus RANGE FOR SEDIMENT ATTENUATIONS OF 0, 0.025, AND 0.070 dB/m/kHz
SOURCE DEPTH: 1200 m, RECEIVER DEPTH: 91 m
BOTTOM SLOPE: 3°

ARL:UT
AS-80-809-P
SRR-GA
2-21-80

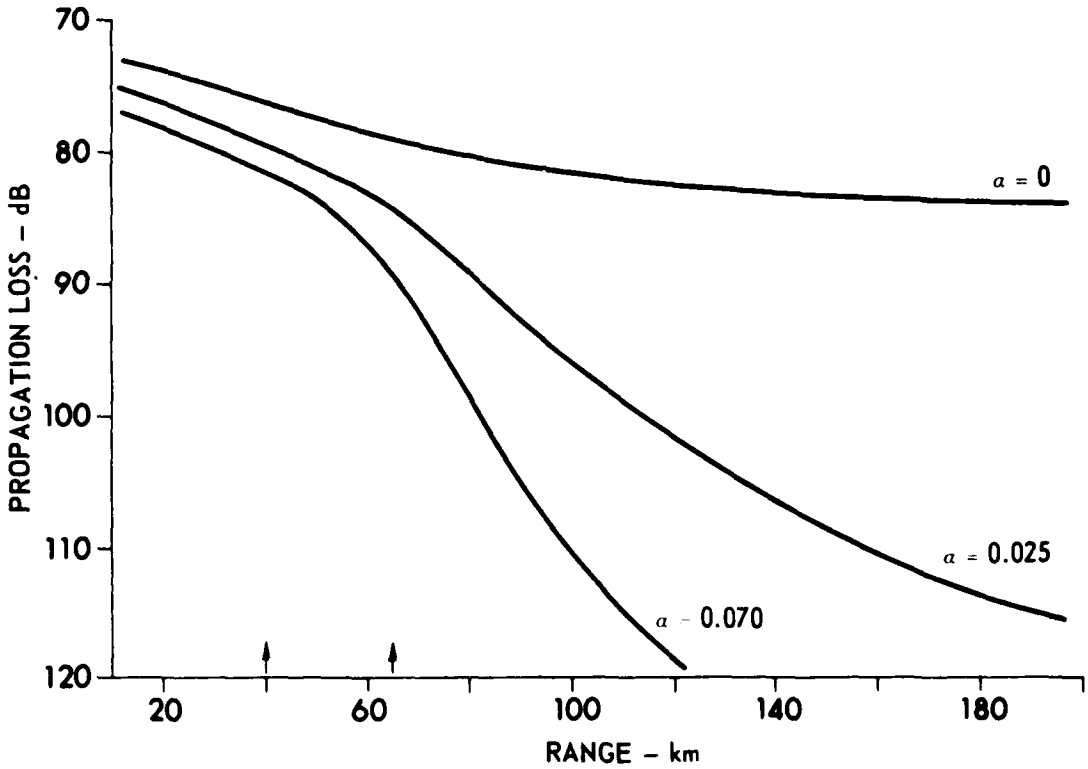

FIGURE III.25
UPSLOPE PROPAGATION LOSS versus RANGE FOR SEDIMENT ATTENUATIONS OF 0, 0.025, AND 0.070 dB/m/kHz

SOURCE DEPTH: 1600 m, RECEIVER DEPTH: 91 m
BOTTOM SLOPE: 3°

ARL:UT
AS-80-808-P
SRR-GA
2-21-80

slope angle is 3°. With reference to Fig. III.2, r_1 is 40 km and r_2 is about 130 and 67 km, respectively, for slopes of 1° and 3°. There are two notable characteristics of the six curves just described. First, increased sensitivity to attenuation in the shallow water (long ranges) regions is exhibited with source depths above or below the deep water channel (Figs. III.20, III.22, III.23, and III.25) when compared with sources in the channels. Second, the curves for sources in the deep water sound channel (Figs. III.21 and III.24) show a more uniform sensitivity to sediment attenuation from deep to shallow water and exhibit a slope enchancement effect that is maximal at the edge of the slope in shallow water.

The behavior of the curves for the deep and shallow source depths can be explained as follows. For shallow or deep source depths, the bottom interacting modes are excited to the greatest degree; i.e., little excitation of SOFAR modes occurs. Three mechanisms tend to reduce the number of effective modes as they travel upslope: (1) increasing mode attenuation due to increasing mode equivalent bottom angle coupled with the changing mode character, (2) mode cutoff processes, and (3) spreading loss. The first of these results in increased sensitivity to sediment attenuation and is analogous to the mechanism discussed in the previous section concerning downslope propagation. The strongly bottom interacting modes excited by deep or shallow sources become even more strongly bottom interacting as they propagate upslope, and are therefore more heavily attenuated. This results in increasing sensitivity to attenuation as the modes propagate upslope. The renormalization effect acts to counteract the above three mechanisms by increasing the acoustic energy density in the water as the water depth decreases, but for the shallow and deep source depths the renormalization gain (RG) is overcome by the strong bottom interaction.

When the source is located in the deep water sound channel, as in Figs. III.21 and III.24, the SOFAR modes (which do not significantly interact with the bottom) are excited along with the bottom interacting modes. In this case the renormalization gain overtakes the attenuation loss

and actually causes an increase in intensity with range. This increase peaks near the edge of the slope where the renormalization gain is maximum. This effect is referred to as "slope enhancement" and is readily apparent in Figs. III.21 and III.24. Another effect of the renormalization gain for sources in the deep water sound channel is to lessen the sensitivity of the propagation to sediment attenuation in the shallow water. Figure III.24 shows greater sensitivity than Fig. III.21 because the portion of the range interval that is in shallow water is much greater because of the steeper transition from deep to shallow water.

Another view of upslope propagation is given in Figs. III.26 and III.27. These curves present propagation loss versus depth for five ranges and source depths of 1200 and 1600 m. The bottom slope is 1° and the sediment attenuation is 0.025 dB/m/kHz. Note the slope enhancement effects in Fig. III.26, particularly at 125 km. This effect is absent in Fig. III.27. Also note the less efficient transfer of energy into shallow water at 200 km with the deeper source.

The same general conclusion reached in the section on downslope propagation can be drawn here. The work presented in this section reinforces the hypothesis that the bottom attenuation properties in the shallow water regions are most critical when attempting to model upslope sound propagation, particularly for shallow or deep sources.

3. Slope Angle Effects

In this subsection the dependence of upslope acoustic propagation on slope angle will be investigated. Figures III.28-III.30 depict propagation loss versus range for three different source-receiver depth combinations, slope angles of 1° and 3°, and a sediment attenuation of 0.025 dB/m/kHz. The first arrows along the range axes denote the starting range of the slope. The second and third denote the end of the upslope rise for 3° and 1° slope angles, respectively.

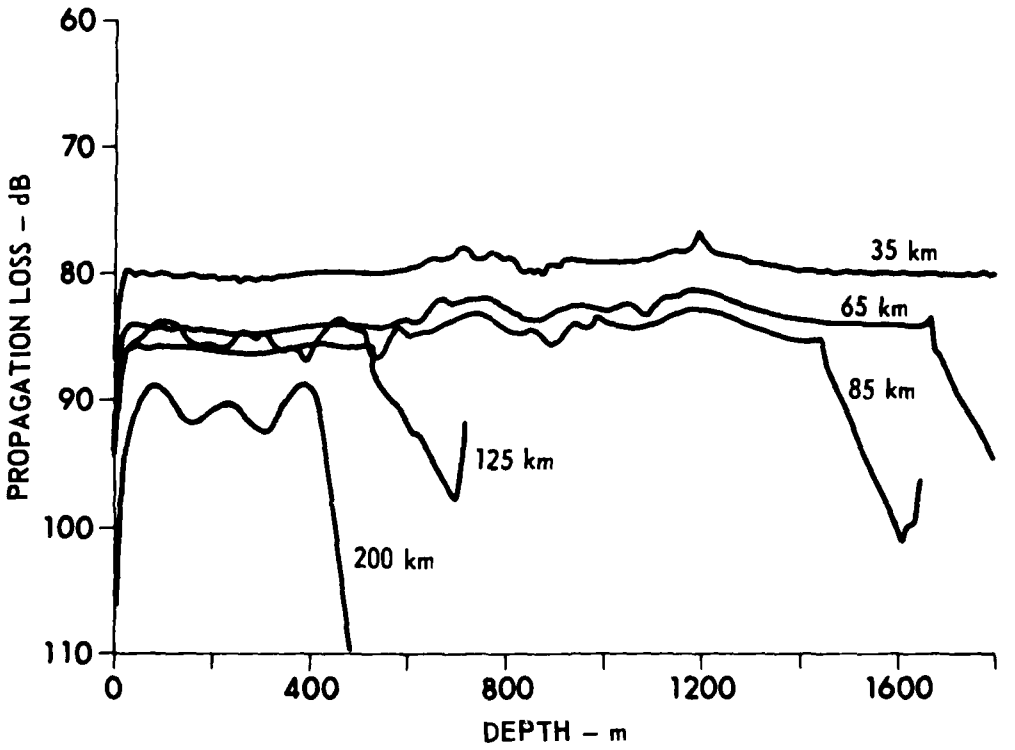

FIGURE III.26
UPSLOPE PROPAGATION LOSS versus DEPTH
FOR RANGES OF 35, 65, 85, 125, AND 200 km
SOURCE DEPTH: 1200 m, BOTTOM SLOPE: 1°
BOTTOM ATTENUATION: 0.025 dB/m/kHz

ARL:UT
AS-80-819-P
SRR-GA
2-21-80

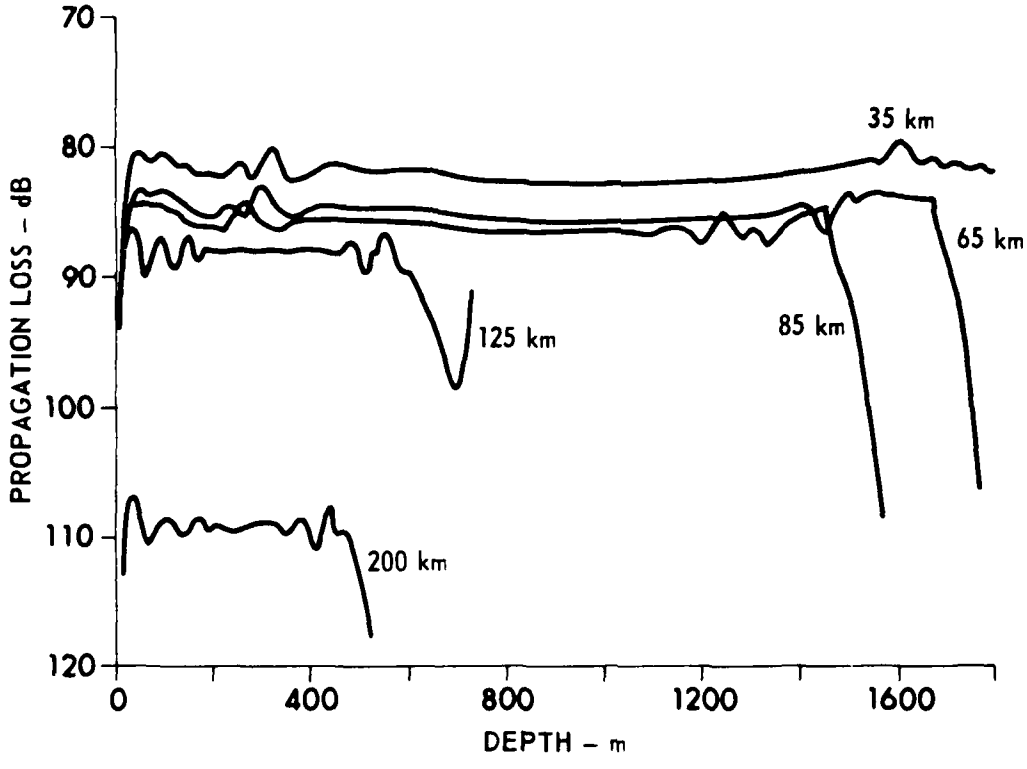

FIGURE III.27
UPSLOPE PROPAGATION LOSS versus DEPTH
FOR RANGES OF 35, 65, 85, 125, AND 200 km
SOURCE DEPTH: 1600 m, BOTTOM SLOPE: 1°
BOTTOM ATTENUATION: 0.025 dB/m/kHz

ARL:UT
AS-80-818-P
SRR-GA
2-21-80

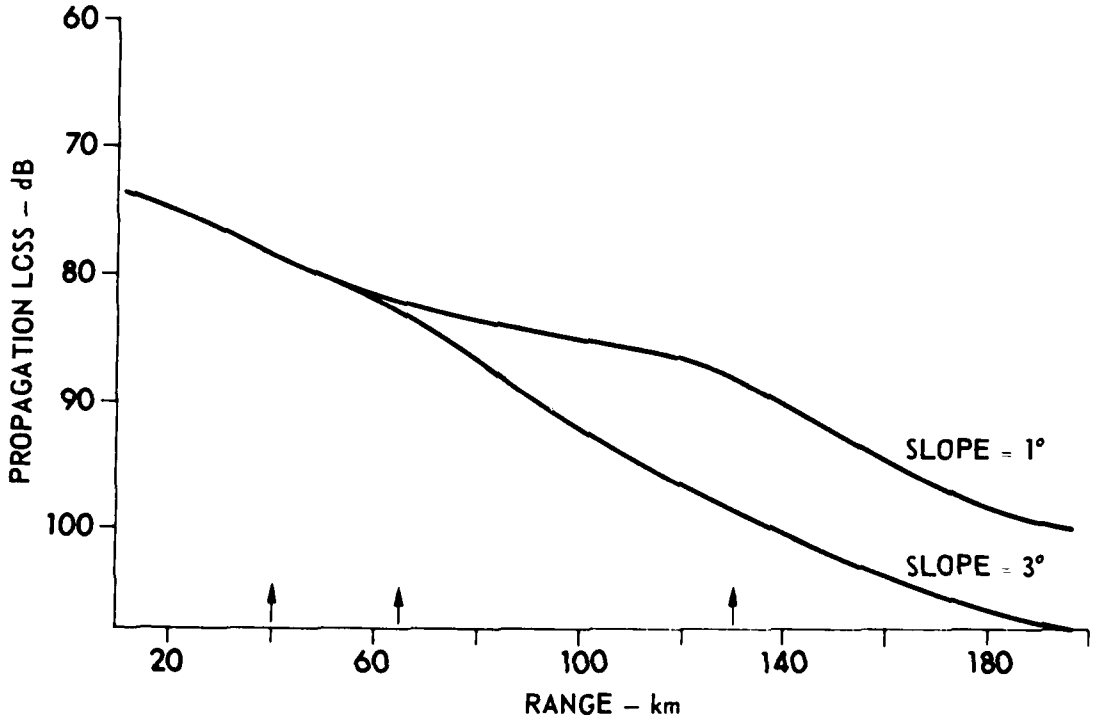

FIGURE III.28
UPSLOPE PROPAGATION LOSS versus RANGE
FOR BOTTOM SLOPES OF 1 AND 3°
SOURCE DEPTH: 91 m, RECEIVER DEPTH: 91 m
SEDIMENT ATTENUATION: 0.025 dB/m/kHz

ARL:UT
AS-80-814-P
SRR-GA
2-21-80

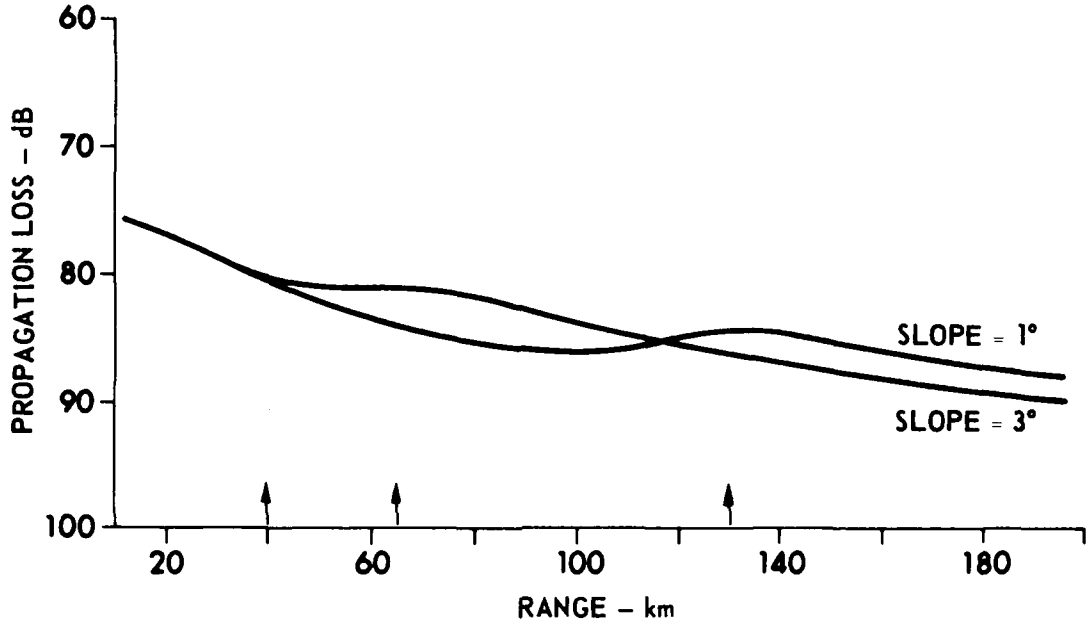

FIGURE III.29
UPSLOPE PROPAGATION LOSS versus RANGE
FOR BOTTOM SLOPES OF 1 AND 3°
SOURCE DEPTH: 1200 m, RECEIVER DEPTH: 91 m
SEDIMENT ATTENUATION: 0.025 dB/m/kHz

ARL:UT
AS-80-815-P
SRR-GA
2-21-80

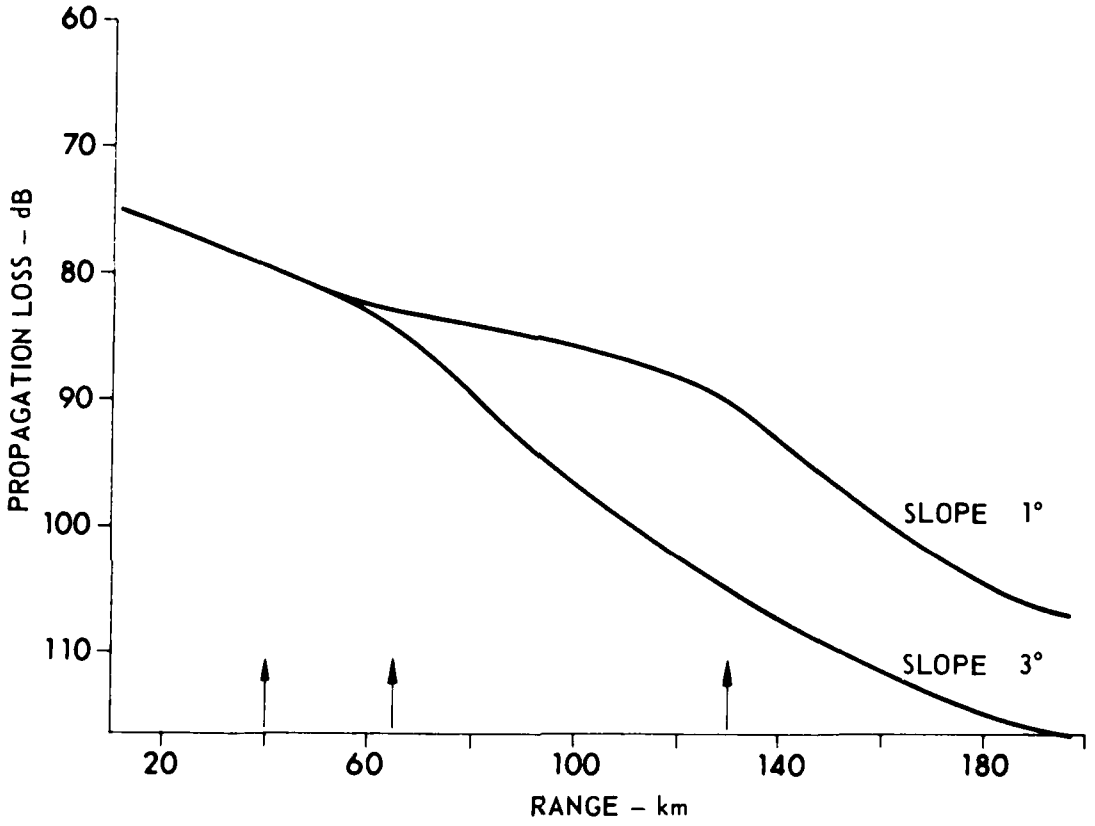

FIGURE III.30
UPSLOPE PROPAGATION LOSS versus RANGE
FOR BOTTOM SLOPES OF 1 AND 3°
SOURCE DEPTH: 1600 m, RECEIVER DEPTH: 91 m
SEDIMENT ATTENUATION: 0.025 dB/m/kHz

ARL:UT
AS-80-816-P
SRR-GA
2-21-80

The curves for shallow and deep sources (Figs. III.28 and III.30) show a much greater sensitivity to bottom slope angle than the downslope cases (see Figs. III.15 and III.16). Figure III.29 shows somewhat less sensitivity. The behavior of the curves in Figs. III.28 and III.30 is similar. The 1° and 3° curves are identical to a range of 60 km; beyond 60 km the 1° curves lie above the 3° curves, with the two curves becoming parallel in the shallow water flat bottom regions of the waveguide ($r > 130$ km). At these ranges all propagation mechanisms are the same, thus accounting for the parallel behavior of the curves. The downward bias of the 3° curve occurs because with the steeper slope the sound reaches the shallow water region sooner. Since bottom interaction is greatest in the shallow water region, sound is exposed to the highest loss areas over a greater distance for a steeper slope. For example, the 3° slope has a range duration of about 27 km and the 1° slope about 80 km. Therefore, one would expect the 3° curve to be biased downward from the 1° curve at the longer ranges by an amount proportional to the excess attenuation accumulated by longer exposure to the larger shallow water attenuation effects.

Figure III.29 exhibits a more complicated behavior than Figs. III.28 and III.30 because of the slope enhancement effects now possible with a source in the sound channel. The 1° curve is again above the 3° curve in the shallow water regions ($r \geq 130$ km) for the same reasons stated above. In the region between 40 and 115 km the 3° curve lies above the 1° curve because of slope enhancement, which is maximized first for the 3° slope.

Figures III.31 and III.32 depict upslope propagation loss versus depth at a range of 200 km for source depths of 1200 and 1600 m. Each figure contains a curve for bottom slope angles of 1° and 3°. By comparing these figures with Fig. III.17, one can see that the transmission of sound upslope is more sensitive to slope angle than downslope transmission. Figure III.31 shows less slope angle sensitivity than Fig. III.32 because the initial field has a larger portion of nonbottom interacting modes for the 1200 m source depth and therefore exhibits less

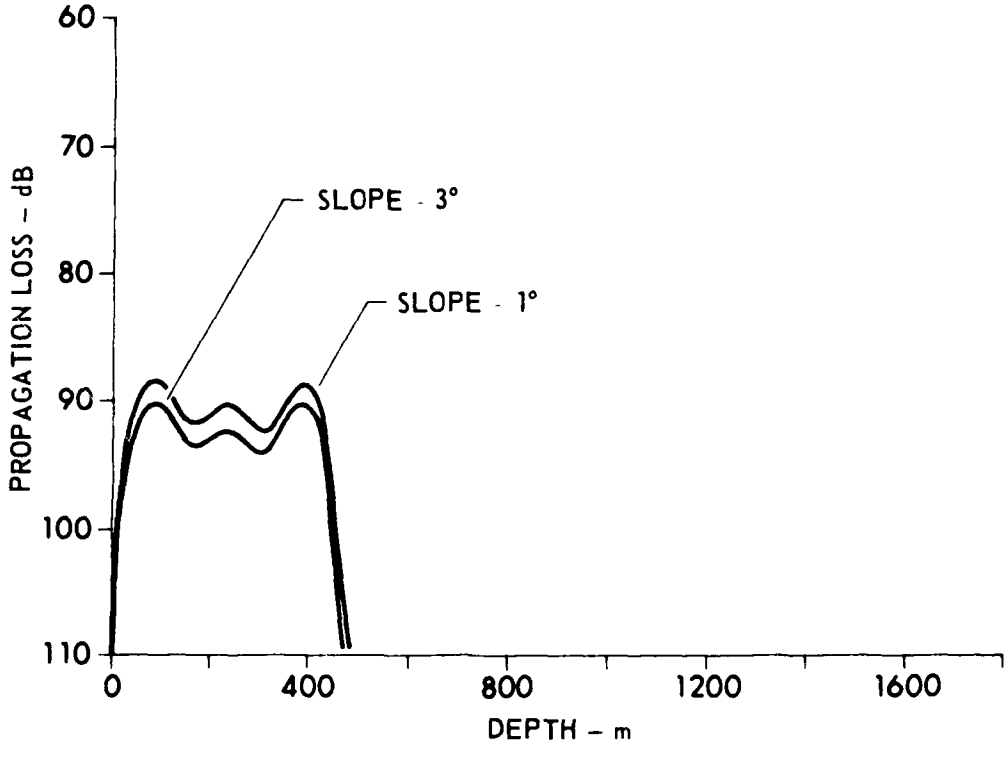

FIGURE III.31
UPSLOPE PROPAGATION LOSS versus DEPTH
FOR BOTTOM SLOPES OF 1 AND 3°
SEDIMENT ATTENUATION: 0.025 dB/m/kHz
SOURCE DEPTH: 1200 m, RANGE: 200 km

ARL:UT
AS-80-817-P
SRR-GA
2-21-80

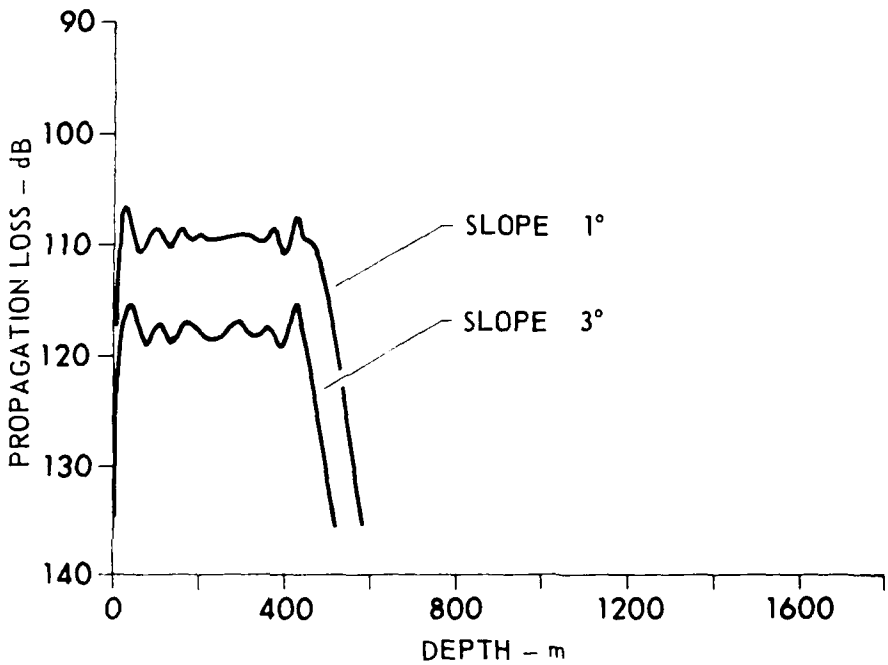

FIGURE III.32
***UPSLOPE PROPAGATION LOSS versus* DEPTH**
FOR BOTTOM SLOPES OF 1 AND 3°
SEDIMENT ATTENUATION: 0.025 dB/m/kHz
SOURCE DEPTH: 1600 m, RANGE: 200 km
FREQUENCY: 50 Hz

ARL:UT
AS-80-843
SRR-GA
2-27-80

sensitivity to bottom attenuation effects. The sensitivity to slope angle is significant for the 1600 m source depth, and the same type of behavior is obtained for shallow source depths.

C. Conclusions

This section summarizes the major conclusions reached during the course of the work on upslope and downslope propagation. It has been determined that the gross structure (minus phase effects) of acoustic propagation over a sloping bottom can be explained in terms of bottom attenuation effects, renormalization effects, spreading loss, and mode cutoff effects. The renormalization effects produce a gain in upslope propagation and a loss in downslope propagation. The mode cutoff effects are not operational in downslope propagation.

Concerning downslope propagation, the following statements can be made.

(1) The acoustic field is particularly sensitive to the shallow water bottom attenuation profile.

(2) The importance of bottom interaction mechanisms decreases as sound propagates from shallow to deep water and becomes negligible when the deep water sound channel becomes fully developed.

(3) The sensitivity of the acoustic field to the bottom attenuation greatly increases as sound propagates from shallow to deep water.

(4) Downslope acoustic propagation is not particularly sensitive to bottom slope.

With regard to upslope acoustic propagation, the following statements can be made.

(1) The acoustic field is particularly sensitive to the shallow water bottom attenuation profile.

(2) The importance of bottom interaction mechanisms increases as sound travels upslope from deep to shallow water where it reaches a maximum.

(3) The sensitivity of the acoustic field to the bottom attenuation greatly increases as sound travels from deep to shallow water.

(4) Upslope sound transmission is sensitive to slope angle, especially for deep or shallow source depths.

(5) A slope enhancement effect is possible in upslope propagation and is most apparent for source depths in the deep sound channel.

CHAPTER IV

THEORETICAL DEVELOPMENT OF THE MATHEMATICAL FORMALISM FOR IMPLEMENTING COUPLED MODE THEORY

The purpose of this chapter is to report on some further extensions of the theoretical mode coupling work that was completed in 1979 (see Ref. 4). This previous work focused on placing coupled mode theory on a firm theoretical foundation, and a corrected coupled mode theory was derived for use in propagation problems involving sloping boundaries. The work to be presented in this chapter concerns the implementation of coupled mode theory as a computational tool. Questions concerning when mode coupling effects become important, the coupling of energy into the backscattered field, and approximate methods for including mode coupling processes are addressed.

The material in this chapter is presented in the following order. First, expressions describing the radial functions for a general range dependent waveguide are derived. The derivations employ a WKB approximation for the radial Green's function. Next, first order perturbation theory is applied to the radial functions to produce expressions correct to first order in the rates of change of the medium, and attenuation is introduced. Finally, possible applications of the theoretical developments are discussed. These discussions concern the neglect of the backscattered field, estimation of the importance of mode coupling compared to attenuation, approximate ways to include mode coupling, and the use of modal transmission and reflection coefficients.

A. Theory

1. Fundamentals

Expressions for the acoustic field due to a point source, including mode coupling to first order, provide the starting point for the theoretical work of this section. These expressions were derived in detail in Ref. 4 and the results are reproduced below.

$$[\nabla^2+k^2(z,r)]\psi(z,r) = -4\pi\delta(\vec{r}-\vec{r}_o) \quad . \tag{4.1}$$

$$\psi(z,r) = \sum_n \frac{G_n(r)}{\sqrt{r}} [\phi_n(z,r)+\delta\phi_n(z,r)] \quad . \tag{4.2}$$

$$\left[\frac{d^2}{dr^2} + k_m^2(r) + \frac{1}{4r^2}\right] G_m(r) = -2 \sum_n{}' B_{mn} \frac{dG_n}{dr} = \beta_m(r) \quad . \tag{4.3}$$

$$\left[\frac{\partial^2}{\partial z^2} + k^2(z,r) - k_n^2(r)\right] \phi_n(z,r) = 0 \quad . \tag{4.4}$$

$$\left[\frac{\partial^2}{\partial z^2} + k^2(z,r) - k_n^2(r)\right] \delta\phi_n = \frac{-2}{G_n} \frac{dG_n}{dr} B_{nn}\phi_n \quad . \tag{4.5}$$

$$B_{mn}(r) = \int_o^\infty \phi_m(z,r) \frac{\partial\phi_n}{\partial r}(z,r)dz \quad . \tag{4.6}$$

In Eqs. (4.1) and (4.2) ψ is the velocity potential and $\sum_n{}'$ in Eq. (4.3) denotes a summation in which n=m is excluded.

$$\sum_{n}' = \sum_{\substack{n \\ n \neq m}} \tag{4.7}$$

The waveguide context within which the developments of this chapter are discussed is shown in Fig. IV.1. This waveguide geometry assumes that there is a region near the source between 0 and r_o which is essentially independent of range and a farfield region starting at r_f where the medium is again independent of range. The range variability is assumed to occur between r_o and r_f and is not restricted in any way.

The solution of Eq. (4.3) is of interest. The corrections to the depth functions $\delta\phi_n$ are not considered since previous work has indicated that they are of minor importance in general and of no importance when incoherent mode sums are performed. The solution to Eq. (4.3) can be expressed as

$$G_m(r) = F_m(r) + P_m(r) \quad , \tag{4.8}$$

where $F_m(r)$ and $P_m(r)$ are the homogeneous and particular solutions to Eq. (4.3), respectively. The function F_m satisfies

$$\left(\frac{d^2}{dr^2} + k_m^2(r) + \frac{1}{4r^2}\right) F_m(r) = 0 \quad , \tag{4.9}$$

and P_m, which contains the effects due to mode coupling, can be expressed as

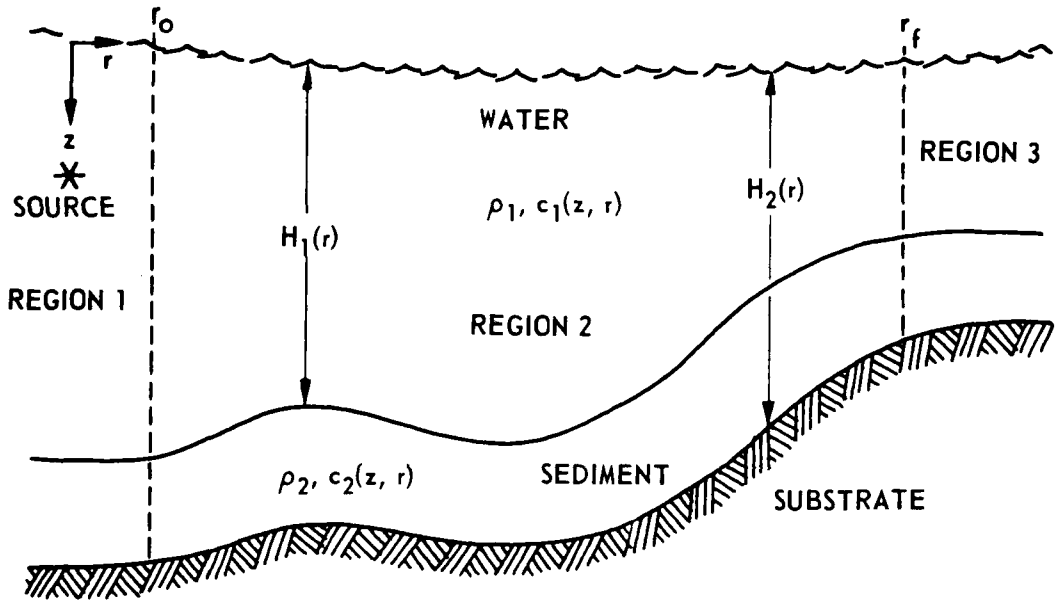

FIGURE IV.1
WAVEGUIDE GEOMETRY

ARL:UT
AS-80-869-P
SRR-GA
3-6-80

$$P_m(r) = \int_0^r g_m^{>}(r,r')\ \beta_m(r')dr' + \int_r^{\infty} g_m^{<}(r,r')\ \beta_m(r')dr' \ . \quad (4.10)$$

In Eq. (4.10) $g_m(r,r')$ is a Green's function formed from two linearly independent solutions of Eq. (4.9) and is given by (see Ref. 23, Chapter 16)

$$g_m^{>}(r,r') = \frac{y_m^{(+)}(r)\ y_m^{(-)}(r')}{W_m} \qquad r > r' \quad (4.11)$$

and

$$g_m^{<}(r,r') = \frac{y_m^{(+)}(r')\ y_m^{(-)}(r)}{W_m} \qquad r < r' \quad , \quad (4.12)$$

where $y_m^{(+)}$ and $y_m^{(-)}$ are two linearly independent solutions of Eq. (4.9) and W_m is this Wronskian defined by

$$W_m = y_m^{(-)} \frac{d}{dr} y_m^{(+)} - y_m^{(+)} \frac{d}{dr} y_m^{(-)} \quad . \quad (4.13)$$

To this point the development has been completely general even though the particular solutions cannot be obtained without resorting to some sort of iterative or perturbation technique. Now, a WKB approximation for the Green's function will be introduced and used throughout the remainder of this chapter. A WKB Green's function should work quite well because the solutions to Eq. (4.9) for the discrete modes have no turning points in realistic propagation problems. The WKB Green's function is

obtained by assuming that $y_m^{(+)}$ and $y_m^{(-)}$ are given by the WKB solutions of Eq. (4.9)

$$y_m^{(\pm)}(r) = \frac{1}{\sqrt{k_m(r)}} \exp\left\{\pm i \int_0^r k_m(x)dx \mp \frac{i\pi}{4}\right\} \quad . \tag{4.14}$$

In Eq. (4.14) r=0 is the reference range and the $1/4r^2$ term in Eq. (4.9) is neglected in comparison to k_m^2. If Eq. (4.14) is used with Eqs. (4.11)-(4.13), one obtains the WKB Green's function given below.

$$g_m^>(r,r') = \frac{\exp\left(i \int_{r'}^r k_m(x)dx\right)}{2i\sqrt{k_m(r)\ k_m(r')}} \qquad r > r' \tag{4.15}$$

$$g_m^<(r,r') = \frac{\exp\left(-i \int_{r'}^r k_m(x)dx\right)}{2i\sqrt{k_m(r)\ k_m(r')}} \qquad r < r' \tag{4.16}$$

The solution to Eq. (4.3) may now be expressed within the WKB approximation as

$$G_m(r) = F_m(r) + y_m^{(+)}(r)\int_0^r \frac{y_m^{(-)}(r')\ \beta_m(r')dr'}{2i} + y_m^{(-)}(r)\int_r^\infty \frac{y_m^{(+)}(r')\ \beta_m(r')dr'}{2i} \tag{4.17}$$

where Eqs. (4.8), (4.10), and (4.11)-(4.14) were employed. Equation (4.17) may be recast into the following form.

$$G_m(r) = F_m(r) + y_m^{(+)}(r)\ \Gamma_m^{(+)}(r) + y_m^{(-)}(r)\ \Gamma_m^{(-)}(r) \quad , \qquad (4.18)$$

where $\Gamma_m^{(+)}$ and $\Gamma_m^{(-)}$ are given by

$$\Gamma_m^{(+)}(r) = \int_0^r \frac{y_m^{(-)}(r')\ \beta_m(r')\,dr'}{2i} \quad , \qquad (4.19)$$

and

$$\Gamma_m^{(-)}(r) = \int_r^\infty \frac{y_m^{(+)}(r')\ \beta_m(r')dr'}{2i} \quad . \qquad (4.20)$$

Returning now to the waveguide geometry of Fig. IV.1, one can express the solutions for the radial functions in the three regions noted in the following forms.

$$G_m^{(1)}(r) = A_m\sqrt{r}\left[H_0^{(1)}(k_m r) + a_m H_0^{(2)}(k_m r)\right] \qquad r \le r_o \quad , \qquad (4.21)$$

$$G_m^{(2)}(r) = A_m\left[\alpha_m y_m^{(+)} + \varepsilon_m y_m^{(-)}\right] + \Gamma_m^{(+)} y_m^{(+)} + \Gamma_m^{(-)} y_m^{(-)} \qquad r_o < r \le r_f \quad , \qquad (4.22)$$

$$G_m^{(3)}(r) = A_m b_m \sqrt{r}\ H_0^{(1)}(k_m r) \qquad r > r_f \quad . \qquad (4.23)$$

In Eq. (4.22) a WKB approximation for $F_m(r)$ has been employed. In Eqs. (4.21) and (4.23), it is to be understood that the wave numbers are

to be taken from the sets appropriate to the range invariant regions 1 and 3, respectively.

The constant A_m is easily determined by requiring that the field satisfy point source conditions at range 0. Near r=0, $G_m^{(1)}$ should satisfy the following equation (see Refs. 11 and 4).

$$\hat{L}_r \left(\frac{G_m^{(1)}}{\sqrt{r}} \right) = \frac{-2\delta(r)\rho(z_o)\phi_m(z_o,o)}{r} \quad , \tag{4.24}$$

with $\hat{L}_r$ an operator given by

$$\hat{L}_r = \frac{d^2}{dr^2} + \frac{1}{r}\frac{d}{dr} + k_m^2 \quad .$$

If one recognizes that $\hat{L}_r$ operating on $H_0^{(1,2)}$ gives

$$\hat{L}_r \, H_0^{(1)}(k_m r) = \frac{2i}{\pi}\frac{\delta(r)}{r} \quad ,$$

$$\hat{L}_r \, H_0^{(2)}(k_m r) = \frac{-2i}{\pi}\frac{\delta(r)}{r} \quad ,$$

then A_m is easily seen to be given by

$$A_m = \frac{i\pi\rho(z_o)\ \phi_m(z_o,o)}{(1-a_m)} \quad . \tag{4.25}$$

The remaining constants in Eqs. (4.21)-(4.23) may be found by requiring the G_m function and its derivative to be continuous across the interfaces between regions 2 and 3 at r_f and 1 and 2 at r_o. Starting with the interface at r_f first, one finds that ε_m and b_m are given by

$$\varepsilon_m = 0 \tag{4.26}$$

and

$$b_m = \left[\alpha_m + \frac{\Gamma_m^{(+)}(r_f)}{A_m}\right] \frac{y_m^{(+)}(r_f)}{\sqrt{r_f}\, H_0^{(1)}\left[k_m(r_f) r_f\right]} \quad . \tag{4.27}$$

In obtaining Eqs. (4.26) and (4.27) the following expressions were employed.

$$\Gamma_m^{(-)}(r) = 0 \qquad r \geq r_f \quad , \tag{4.28}$$

$$\frac{d}{dr}\, y_m^{(\pm)} \approx \pm i k_m y_m^{(\pm)} \quad . \tag{4.29}$$

Matching the solutions for $G_m^{(1)}$ and $G_m^{(2)}$ at r_o allows one to determine a_m and α_m.

$$a_m = \frac{y_m^{(-)}(r_o)\Gamma_m^{(-)}(r_o)}{\Lambda_m \sqrt{r_o}\, H_0^{(2)}\left[k_m(r_o) r_o\right]} \quad . \tag{4.30}$$

$$\alpha_m = \frac{\sqrt{r_o}\, H_0^{(1)}\, k_m(r_o) r_o}{y_m^{(+)}(r_o)} \quad . \tag{4.31}$$

In determining Eq. (4.31), use was made of the following expression.

$$\Gamma_m^{(+)}(r) = 0 \qquad r \le r_o \quad . \tag{4.32}$$

Some simplification of the matching constants can be obtained by using the asymptotic forms of the Hankel functions given by

$$H_0^{(1,2)}(x) = \sqrt{\frac{2}{\pi x}}\, e^{\pm i(x-\pi/4)} \quad , \tag{4.33}$$

which is consistent with the use of the WKB approximation throughout this chapter. Equations (4.25) and (4.30) can be combined to give

$$a_m = \frac{\sigma_m \Gamma_m^{(-)}(r_o)}{1 + \sigma_m \Gamma_m^{(-)}(r_o)} \quad . \tag{4.34}$$

Equation (4.31), with the use of Eq. (4.33), becomes

$$\alpha_m = \sqrt{\frac{2}{\pi}} \quad . \tag{4.35}$$

Equation (4.27) becomes, with the use of Eqs. (4.25), (4.33), (4.34), and (4.35),

$$b_m = \left[1 + \frac{\Gamma_m^{(+)}(r_f)\sigma_m}{1 + \sigma_m \Gamma_m^{(-)}(r_o)}\right] \exp\left[i\int_0^{r_f} k_m dx - ik_m(r_f)r_f\right] \quad . \quad (4.36)$$

In Eqs. (4.34) and (4.36) σ_m is a constant for a given mode number defined by

$$\sigma_m = \frac{-i}{\sqrt{2\pi}\ \rho(z_o)\ \phi_m(z_o,0)} \quad . \quad (4.37)$$

The overall normalization constant A_m can be obtained by combining Eqs. (4.25) and (4.34) to obtain

$$A_m = i\pi\rho(z_o)\ \phi_m(z_o,0)\left|1+\sigma_m\Gamma_m^{(-)}(r_o)\right| \quad . \quad (4.38)$$

At this juncture one can write down a general expression for the radial function in region 2 where the range dependence of the medium occurs. This expression is given below.

$$G_m^{(2)}(r) = \left[1+\sigma_m\Gamma_m^{(-)}(r_o)\right]\frac{y_m^{(+)}}{\sigma_m} + \Gamma_m^{(+)}y_m^{(+)} + \Gamma_m^{(-)}y_m^{(-)} \quad . \quad (4.39)$$

It is reassuring to note that Eq. (4.39) reduces to the radial equation for a horizontally stratified medium when the range dependence of the

AD-A098 522 TEXAS UNIV AT AUSTIN APPLIED RESEARCH LABS F/G 20/1
A SUMMARY OF THE RESULTS OF A STUDY OF ACOUSTIC BOTTOM INTERACT--ETC(U)
NOV 80 S R RUTHERFORD, S G PAYNE, R A KOCH N00014-78-C-0113
UNCLASSIFIED ARL-TR-80-56 NL

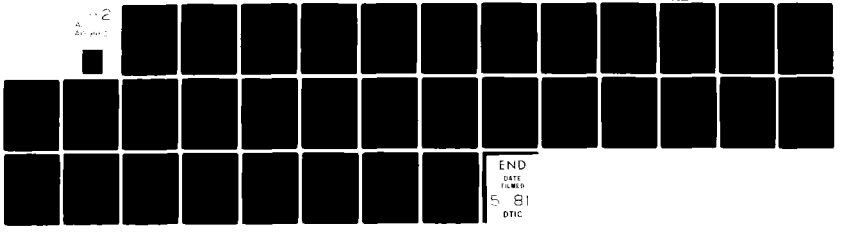

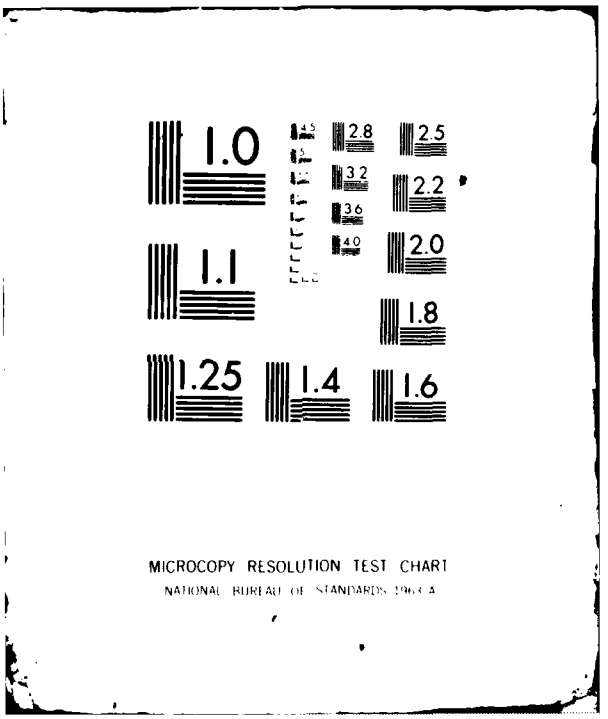
1.0
1.1
1.25
1.4
1.6
1.8
2.0
2.2
2.5
2.8
3.2
3.6
4.0
MICROCOPY RESOLUTION TEST CHART
NATIONAL BUREAU OF STANDARDS 1963 A

medium goes to zero ($\beta_m \to 0$). In this situation $G_m^{(2)}(r)$ should reduce to

$$i\pi\rho(z_o)\phi_m(z_o,0)\ \sqrt{r}\ H_0^{(1)}(k_m r) \quad .$$

If one uses Eq. (4.33) it is easy to verify that Eq. (4.39) reduces to the appropriate limit as the range variability of the medium approaches zero.

Equation (4.39) can be rearranged to the following form.

$$G_m^{(2)}(r) = \frac{y_m^{(+)}(r)}{\sigma_m} + \left[\Gamma_m^{(+)}(r) + \Gamma_m^{(-)}(r_o)\right] y_m^{(+)}(r) + \Gamma_m^{(-)}(r)\ y_m^{(-)}(r) \quad . \tag{4.40}$$

With the equation for $G_m^{(2)}$ written in this form all the effects due to mode-mode coupling are isolated in the second and third terms. The first term in Eq. (4.40) is the forward going adiabatic solution for mode m. The second term represents the contribution from mode m to the forward going field arising from energy coupled into mode m from the other propagating modes. The third term represents the contribution from mode m to the backscattered field due to energy coupled into mode m from other modes.

With reference to the radial equations in the source and farfield regions, i.e., Eqs. (4.21) and (4.23), it is possible to define potentially useful mode transmission and reflection coefficients. The coefficient a_m given by Eq. (4.34) can be defined as the reflection coefficient for mode m. This reflection coefficient gives the ratio of the backscattered amplitude to the forward going amplitude of mode m. In the limit of no range dependence, a_m goes to zero as expected. The coefficient b_m in Eq. (4.23) can be defined as a mode amplitude transmission

coefficient. This transmission coefficient is proportional to the amplitude of mode m that is transmitted from the source region through the range dependent region and into the farfield. More will be said about the potential use of these reflection and transmission coefficients later in this chapter.

2. First Order Perturbation Theory

As mentioned before, because of the coupled nature of the differential equations for G_m, one must resort to an iterative perturbation theory scheme to solve for the $G_m(r)$ functions when using the Green's function methods outlined in the previous section. There are ways other than using Green's functions to solve[4] the coupled radial equations. For example one can solve Eq. (4.3) directly using finite difference techniques. This technique, however, has the disadvantage that it requires the manipulation of matrices which are of the order of M · NR, where M is the number of modes present and NR is the number of range mesh points. One can also solve Eq. (4.3) in principle by diagonalizing the system of equations and then using standard techniques (see Ref. 24). This method, however, requires a range dependent diagonalization procedure, except for certain canonical types of range dependence, and is not particularly attractive.

The technique to be described in this section is a first order perturbation theory method for solving Eq. (4.3) via Eqs. (4.8)-(4.10). This method is the same one used so successfully in the solution of the Lippmann-Schwinger[25] equation of quantum mechanical potential scattering. The perturbation iteration procedure is carried out only to first order here because, due to the nature of the boundary condition approximations (see Refs. 4 and 5) in coupled mode theory, one is only entitled to include mode coupling effects to first order. This first order perturbation theory is analogous to the Born approximation[25] of the Lippmann-Schwinger equation.

The equation to be solved by perturbation theory is

$$\frac{d^2}{dr^2} G_m + k_m^2(r)G_m = \lambda\beta_m(r) = -\lambda \sum_n{}' 2\left(\frac{B_{mn}}{\lambda}\right) \frac{dG_n}{dr} \quad , \qquad (4.41)$$

where a perturbation strength parameter λ has now been introduced. The perturbation parameter λ is of first order in B_{mn}, which also implies it is of first order in range rates of change of the waveguide such as $dH/dr=\dot{H}$ and $dc/dr=\dot{c}$. Here H(r) is taken to describe the depth of an interface as a function of range in the waveguide and c(r) represents the radially variable ground speed.

$$\lambda \sim O(B_{mn}) \sim O(\dot{H},\dot{c}) \quad .$$

By introducing λ, $\beta_m(r)$ has been redefined as a zero order quantity. The end results will correspond to the theory outlined in the previous sections when λ is set equal to 1 as is customarily done. The solution to Eq. (4.41) can be written as

$$G_m(r) = F_m(r) + \lambda \int_0^\infty g_m(r,r')\ \beta_m(r')dr' \quad , \qquad (4.42)$$

where it is to be understood that the integral in Eq. (4.42) is to be split as is done in Eq. (4.10). The function F_m, as before, satisfies Eq. (4.9).

To implement the perturbation theory the radial function and the source term are expanded in powers of λ as follows.

$$G_m(r) = G_{0,m} + \lambda G_{1,m} + \lambda^2 G_{2,m} + \ldots \qquad (4.43)$$

$$\beta_m(r) = \beta_m^{(0)} + \lambda\beta_m^{(1)} + \lambda^2\beta_m^{(2)} + \ldots \tag{4.44}$$

$$\beta_m^{(1)} = -\sum_n{}' 2\left(\frac{B_{mn}}{\lambda}\right)\frac{dG_{1,n}}{dr} \quad . \tag{4.45}$$

If Eqs. (4.43) and (4.44) are used in Eq. (4.42) and terms of like powers of λ collected, the result is

$$G_{0,m}(r) = F_m(r) \quad , \tag{4.46}$$

$$G_{1,m}(r) = \int_0^\infty g_m(r,r')\ \beta_m^{(0)}(r')dr' \quad , \tag{4.47}$$

$$G_{2,m}(r) = \int_0^\infty g_m(r,r')\ \beta_m^{(1)}(r')dr' \quad , \tag{4.48}$$

and so on. Therefore, to first order the solution to Eq. (4.41) is given by

$$G_m(r) = F_m(r) + \lambda\int_0^\infty g_m(r,r')\ \beta_m^{(0)}(r')dr' \quad , \tag{4.49}$$

which is equivalent to the Born approximation. If one compares Eqs. (4.40) and (4.49), it is obvious that F_m is given by

$$F_m(r) = G_{0,m} = \frac{y_m^{(+)}}{\sigma_m} \quad , \tag{4.50}$$

which is simply the WKB solution to the adiabatic radial equation. The first order effects of mode coupling are included by using Eq. (4.50) to generate the first order terms $G_{1,m}(r)$.

3. Final Expressions

Before writing down the final expressions for the first order radial functions, it will be useful to introduce attenuation into Eq. (4.50) in the usual way to give

$$F_m(r) = G_{0,m} = \frac{y_m^{(+)}}{\sigma_m} \exp\left(- \int_0^r \delta_m(x)dx \right) \quad . \tag{4.51}$$

Equation (4.51) can now be used to generate the first order corrections $G_{1,m}(r)$ from the zero order source terms $\beta_m^{(0)}(r)$ including the effects of attenuation. The $G_{1,m}(r)$ functions represent the net amplitude coupled into or out of mode m due to interactions with the other propagating modes. By introducing attenuation via Eq. (4.51), the coupling effects given in $G_{1,m}$ will reflect the attenuation of the other modes ($n \neq m$) that are coupling to mode m.

The final first order expression for the field in the range variable region (Region 2) is given by

$$G_m^{(2)}(r) = \frac{y_m^{(+)}}{\sigma_m}\left[1+\sigma_m\gamma_m^{(-)}(r_o)\ \exp(-\delta_m r_o)\right]\ \exp\left(-\int_0^r \delta_m(x)dx\right)$$

$$+\ \gamma_m^{(+)}(r)\ y_m^{(+)} + \gamma_m^{(-)}(r)y_m^{(-)}(r) \quad . \tag{4.52}$$

Equation (4.52) is obtained by applying the techniques of Section IV.A.1 to Eq. (4.49) with $\lambda=1$ and with k_m replaced by $k_m+i\delta_m$ in the exponentials in Eqs. (4.15), (4.16), and (4.33). The $\gamma_m^{(+)}$ are given below.

$$\gamma_m^{(+)} = \int_0^r \frac{y_m^{(-)}(r')\beta_m^{(0)}(r')\ \exp\left(-\int_{r'}^r \delta_m dx\right)dr'}{2i} \tag{4.53}$$

$$= -\sum_n{}' \frac{1}{\sigma_n} \int_0^r dr'\ B_{mn}(r')\sqrt{\frac{k_n(r')}{k_m(r')}}\ \exp\left(i\int_0^{r'}(k_n-k_m)dx - \int_{r'}^r \delta_m dx - \int_0^{r'}\delta_n(x)dx\right)$$

$$\gamma_m^{(-)} = \int_r^{r_f} \frac{y_m^{(+)}(r')\beta_m^{(0)}(r')\ \exp\left(-\int_r^{r'} \delta_m dx\right)dr'}{2i} \tag{4.54}$$

$$= -\sum_n{}' \frac{1}{\sigma_n} \int_r^{r_f} dr'\ B_{mn}(r')\sqrt{\frac{k_n(r')}{k_m(r')}}\ \exp\left(i\int_0^{r'}(k_n+k_m)dx - \int_r^{r'} \delta_m dx - \int_0^{r'}\delta_n(x)dx\right)$$

$$\beta_m^{(0)}(r') = -2i \sum_n{}' B_{mn}(r')\left(\frac{k_n(r')}{\sigma_n}\right)y_n^{(+)}(r')\ \exp\left(-\int_0^{r'} \delta_n(x)dx\right) \tag{4.55}$$

With the further proviso that

$$\left[B_{mn}(r)\sqrt{\frac{k_n(r)}{k_m(r)}}\right]^{-1}\frac{d}{dr}\left[\frac{B_{mn}(r)\sqrt{\frac{k_n(r)}{k_m(r)}}}{i\left[k_n(r)-k_m(r)\right]+\delta_m(r)-\delta_n(r)}\right] \ll 1 \quad ,$$

the integral in Eq. (4.53) is given by

$$\int_0^r dr'\, B_{mn}(r')\sqrt{\frac{k_n(r')}{k_m(r')}}\exp\left[i\int_0^{r'}(k_n-k_m)dx-\int_{r'}^{r}\delta_m dx-\int_0^{r'}dx\delta_n(x)\right]$$

$$\simeq \frac{B_{mn}(r)\sqrt{\frac{k_n(r)}{k_m(r)}}\exp\left(i\int_0^r(k_n-k_m)dx-\int_0^r dx\delta_n(x)\right)}{i\left[k_n(r)-k_m(r)\right]-\delta_n(r)+\delta_m(r)}$$

$$-\frac{B_{mn}(0)\sqrt{\frac{k_n(0)}{k_m(0)}}\exp\left(-\int_0^r\delta_m dx\right)}{i\left[k_n(0)-k_m(0)\right]-\delta_n(0)+\delta_m(0)} \quad .$$

A similar statement holds concerning the integral of Eq. (4.54). Thus, in the limit that the interference wavelength, $|2\pi/(k_n-k_m)|$, is short compared to the characteristic range over which the waveguide varies, the

first order radial corrections follow the range variations in the interference pattern produced by neighboring modes. Equation (4.52) along with Eqs. (4.21) and (4.23) can be used to describe the field in a range variable waveguide like the one in Fig. IV.1. In the next section of this chapter some potentially useful applications of Eq. (4.52) to problems of interest will be discussed.

B. Applications

1. Neglect of Backscattered Energy

An important question that arises when considering propagation in a range variable environment (particularly one with sloping boundaries) concerns the backscattered field generated by the range dependence of the medium. In particular one is interested in whether this component is important when compared to the forward flow of energy. A. O. Williams[26] addressed this point within the context of a wedgeshaped waveguide with pressure release boundaries and found the backscattered field generated in upslope or downslope propagation to be of little significance.

Figure IV.2 shows the magnitude of the forward going amplitude and backscattered amplitude generated by mode coupling effects for upslope propagation in an isovelocity wedge. With reference to Eq. (4.52) curve 1 depicts $|\gamma_m^{(+)}(r)+\gamma_m^{(-)}(r_o)|$ versus range and curve 2 depicts $|\gamma_m^{(-)}(r)|$ versus range. The waveguide used to generate these curves had a rigid sloping bottom of 2.5° slope and an initial water depth of 500 m. The frequency was 20 Hz and the source depth was 200 m. Figure IV.2 indicates that the backscattered field is very insignificant compared to the forward going component. In fact propagation loss computations for the previously described isovelocity wedge proved totally insensitive to the inclusion or deletion of the backscattered field. This finding might lead one to suspect that the backscattered field (for reasonable slope angles) is insignificant for more general types of waveguides as well. This suspicion is strengthened by the fact that mode coupling effects are

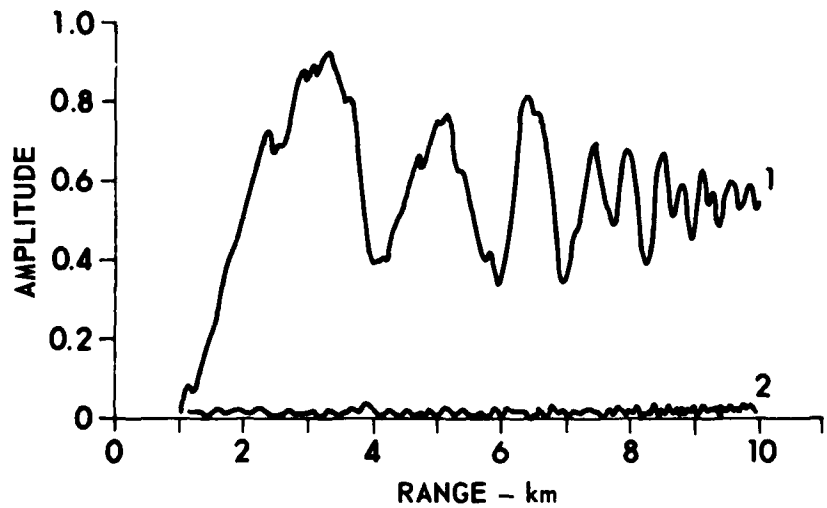

FIGURE IV.2
AMPLITUDES OF OUTGOING AND BACKSCATTERED COMPONENTS OF RADIAL FUNCTION FOR MODE 2

CURVE 1: OUTGOING, CURVE 2: BACKSCATTERED,
FREQUENCY: 20 Hz

ARL:UT
AS-80-875-P
SRR-GA
3-13-80

maximal for a rigid sloping bottom and decrease as the sloping interface becomes penetrable.

A qualitative argument for neglecting backscattering involves a comparison of Eqs. (4.53) and (4.54). The integrands of Eqs. (4.53) and (4.54) consist of slowly varying terms given by

$$B_{mn}(r)\sqrt{\frac{k_n(r)}{k_m(r)}}\exp\left(-\int_0^r \delta_n(x)dx \pm \int_{r'}^r \delta_m dx\right) ,$$

plus rapidly oscillating phase terms given by

$$\exp\left(i\int_0^r (k_n \pm k_m)dx\right) .$$

For all combinations of m and n the phase integral in Eq. (4.54) is extremely rapidly varying which, when coupled with the slowly varying nature of the other terms in the integrand, would lead one to expect small contributions from $\gamma_m^{(-)}$. On the other hand, because wave number differences are involved in the phase integral of Eq. (4.53), one would expect more contributions from $\gamma_m^{(+)}$, especially for mode numbers n close to m. As n ranges farther away from m and the phase integral becomes more rapidly varying, the contributions of those terms to $\gamma_m^{(+)}$ will correspondingly decrease. This gives rise to the possibility of a close coupling approximation in which the n values in the summation of Eq. (4.53) are restricted to a band of nearest neighbor modes centered about m. The numerical calculation of the individual terms contributing to Eq. (4.53) provides a way to quantify the close coupling approximation.

The remainder of the discussion in this chapter will assume that the contributions due to backscattering are negligible. A case for this assumption has been made in the previous discussion and the mathematical expressions required to test the assumption have been presented. The ratio of the backscattered to the forward going components in the source region should be an excellent indicator of the importance of backscattering. This quantity is given by a_m of Eq. (4.34) and is a measure of the total amount of backscattering resulting from the range dependence of the waveguide. In any event, neglecting backscattering, the radial function in Region 2 is given by

$$G_m^{(2)}(r) \approx \frac{y_m^{(+)}}{\sigma_m} \exp\left[-\int^r \delta_m(x)dx\right] + \gamma_m^{(+)} y_m^{(+)} \qquad (4.56)$$

and is obtained from Eq. (4.52) by neglecting the terms involving $\gamma_m^{(-)}$.

2. The Importance of Mode Coupling

Equation (4.56), which is rearranged below, can be used to obtain estimates of the importance of mode coupling effects.

$$G_m^{(2)}(r) = \left[\frac{\exp\left(-\int^r \delta_m dx\right)}{\sigma_m} + \gamma_m^{(+)}\right] y_m^{(+)}(r) \quad . \qquad (4.57)$$

The first term in Eq. (4.57) represents the propagation and attenuation of the energy originally imparted to mode m at the source. The second term represents the net energy transferred into or out of mode m from the other modes. The mode coupling process described by $\gamma_m^{(+)}$ feeds on the other propagating modes, which suffer an attenuation corresponding to the first term in Eq. (4.57); hence, $\gamma_m^{(+)}$ has attenuation effects

built in, and reflects the fact that the other propagating modes have increasingly less energy to couple into mode m due to their attenuation with range.

An examination of the form of Eq. (4.57) reveals that one might expect the effects of mode coupling to be small or even negligible if the magnitude of the second term was much less than the magnitude of the first. This criterion, which is similar to an adiabacity condition derived by Milder,[3] is shown below.

$$\frac{\exp\left(-\int_{}^{r} \delta_m(x)\,dx\right)}{|\sigma_m|} >> |\gamma_m^{(+)}(r)| \qquad (4.58)$$

A numerical comparison of the magnitudes of the first and the second terms in Eq. (4.57) offers a way of determining when mode-mode coupling is important and whether or not it should be included. Previous work,[5] which did not consider attenuation, and Fig. IV.2 have shown that the $\gamma_m^{(+)}$ can influence the magnitude of $G_m^{(2)}$ in a nonnegligible way. With the inclusion of attenuation it is possible that the importance of mode coupling might be considerably lessened or become negligible for some if not all ranges. This hypothesis can be tested by a numerical evaluation of the condition expressed in Eq. (4.58). The potential payoff for an investigation of this sort is great. For example, it might turn out that, at longer ranges from the source, attenuation has so severely limited the amount of energy which can be coupled into a given mode that mode coupling effects are negligible. A finding such as this would allow one to extend the domain of applicability of the adiabatic solution, thus greatly simplifying the numerical calculations to be performed. Equation (4.58) can also conceivably be used to quantify the importance of lateral geoacoustic parameter variability and sloping boundaries in terms of the mode coupling effects they produce.

3. Approximate Methods for Introducing Mode Coupling

An approximate method for introducing mode coupling effects, which can be incorporated in the computational scheme of ADIAB described in Chapter II, is discussed in this section. This approximate method attempts to incorporate the effects of mode coupling additively through Eq. (4.56) and is based on a bin by bin computation of $\gamma_m^{(+)}$.

The approximate method described here will rely on the same range bin partitioning procedure employed in ADIAB, i.e., the medium will be partitioned into range bins and mode functions and wave numbers computed for each range bin. In addition mode coupling coefficients must be computed for each range bin. $\gamma_m^{(+)}$ can be computed by a summation over the range bins, assuming the amplitude factors of Eq. (4.53) to be constant within a bin and evaluating the phase integrals using the splines describing the phase integral variation with range (available from ADIAB). For example if r_i denotes the beginning of a range bin, then the contribution to $\gamma_m^{(+)}$ from that range bin can be expressed as follows.

$$\gamma_m^{(+)}(r_i,r) = -\sum_n{}' \frac{B_{mn}(r_i)}{\sigma_n}\sqrt{\frac{k_n(r_i)}{k_m(r_i)}}\exp\left[i\int_0^{r_i} dr'(k_n-k_m) - \int_0^{r_i}\delta_n dr'\right]$$

$$\times \int_{r_i}^{r} \exp\left\{i\int_{r_i}^{r'}\left[k_n(x)-k_m(x)\right]dx - \int_{r'}^{r}\delta_m dx - \delta_n(r_i)(r'-r_i)\right\}dr' \quad , \tag{4.59}$$

where $r_i \le r < r_{i+1}$. In Eq. (4.59) the argument r_i used in B_{mn}, k_n, and δ_n denotes bin values for the quantities and r is assumed to be within the bin in question. Therefore, to compute the mode coupling term at a range r located in bin N+1, one would evaluate the following expression.

$$\gamma_m^{(+)}(r) = \sum_{i=1}^{N} \gamma_m^{(+)}(r_{i-1}, r_i) \exp\left(-\int_{r_i}^{r} \delta_m dx\right) + \gamma_m^{(+)}(r_N, r) \quad (4.60)$$

where $r_N \leq r < r_{N+1}$. The mode coupling terms evaluated by Eq. (4.60) could then be added to the adiabatic radial functions, already available in ADIAB, to produce the first order radial functions.

The computational method just described could be incorporated in ADIAB relatively easily. The only additional computations of major proportions that are required involve the computation of the modal coupling coefficients for each bin. All the information necessary to test the criterion given by Eq. (4.58) is available during the process of computing the coupling terms. It is easy to imagine testing Eq. (4.58) at the midpoint of each range bin to ascertain the relative importance of mode coupling in that range bin. This procedure could be incorporated in the computational scheme to give a running account of the importance of mode coupling as a function of range.

C. Summary and Conclusions

The purpose of this chapter has been to develop the mathematical formalism for implementing coupled mode theory and to suggest possible applications and approximations of the resulting formalism. In Section IV.A general expressions for the solutions of the coupled radial equations arising in coupled mode theory were derived. WKB expressions for the radial Green's functions were employed in the development of these expressions.

Modal transmission and reflection coefficients describing a range dependent segment of a waveguide were also derived. These quantities are of potential use in continental slope areas. If one were interested only in the field in the deep or shallow water regions (regions 1 and 3 in Fig. IV.1), large computational savings could be effected because the field could be computed in the regions of interest using Eqs. (4.21) and

(4.23) without having to solve for Eq. (4.22). Moreover, approximate methods like those described in Section IV.B.3 could probably be used to evaluate the a_m and b_m coefficients. Investigations such as those concerning the transmission of noise generated in shallow water over the continental slope into deep water might be facilitated through the use of mode transmission and reflection coefficients.

The last part of Section IV.A described perturbation theory as applied to the solution of inhomogeneous differential equations. This perturbation theory approach was then applied in first order to the expressions derived in the first part of the section. In addition attenuation was introduced into the formalism and the different components of mode coupling were pointed out.

In Section IV.B applications and approximations of the results of Section IV.A were discussed. The first topic considered concerned the neglect of backscattering in coupled mode theory. Qualitative arguments and a numerical example were presented to support the contention that backscattering could be neglected in many problems of interest. The next topic concerned ways to estimate the importance of mode coupling relative to an adiabatic description of propagation in which coupling is ignored. The last topic considered an approximate method for including mode coupling effects into the radial functions. This approximate method was described within the context of ADIAB and is based on a bin by bin treatment of mode coupling effects. A method for keeping a running tally of the importance of mode coupling effects was also described.

CHAPTER V
FUTURE DIRECTIONS

In this chapter some possible future areas of research concerning propagation in a range variable environment will be addressed. The state of the art regarding bottom interaction in range variable media is at a point now where the vertical variability bottom interaction problem was three to four years ago. In other words, we are still identifying the basic mechanisms and isolating the important geoacoustic parameters involved in the description of acoustic propagation in a range variable environment. As a result much of the future effort will focus on "zero order" questions such as identifying the basic mechanisms and "first order" questions regarding the sensitivity of acoustic propagation to the important geoacoustic parameters.

The work presented in Chapter III is an example of an investigation of "zero o· and "first order" questions. In particular, this work identified the dominant mechanisms involved in upslope and downslope propagation and specifically focused on the attenuation mechanism, which was shown to be an important geoacoustic parameter. The end result was a study of the effects of attenuation in conjunction with a sloping bottom. Similar studies involving other geoacoustic parameters as sediment sound speed and sediment vertical sound speed gradient should be performed. The mechanisms by which these parameters influence acoustic propagation is understood in a horizontally stratified medium, and this understanding should be extended to sloping bottom media.

Future work should address the lateral variability of subbottom geoacoustic parameters within the context of horizontally stratified layers. The effects of horizontal variations of sediment sound speed, vertical sound speed gradients, and attenuation should be investigated.

The results of these studies will be important in determining the level of detail required to specify the lateral variability of the bottom in order to adequately characterize acoustic propagation. Next, a sloping bottom should be incorporated in the sensitivity studies to determine whether lateral parameter variability is important when coupled with a sloping bottom. The results of this type of study could then be used to ascertain the relative importance of slope geometry versus lateral variability.

Other problem areas that should be investigated, in addition to identifying basic mechanisms and sensitivities, involve range averaging, coherence, three-dimensional problems, and energy partitioning. The questions dealing with coherence should focus on the effects of slopes and lateral variability with respect to field coherence or lack of coherence. At this point there is not much reason to suspect that lateral variability by itself will significantly influence field coherence. However, a sloping bottom, due to multipath conversion effects, could reasonably be expected to influence field coherence in a significant way. The effects of range variability on field coherence (particularly degrading effects) should be quantified in terms of lateral gradients and bottom slopes and the results applied to problems involving arrays (either vertical or horizontal) in a range variable medium.

The problem of energy partitioning between the water and bottom, which can probably be related to the coherence investigations, is another important area of investigation. The questions to be asked here relate to the portion of energy transported through the water compared to the portion transported via bottom interacting paths or modes, and how this changes as a function of lateral variability and bottom slope. Since the degrading effects of bottom interaction on field coherence are related to the relative amounts of bottom interacting and nonbottom interacting energy arriving at an array of receivers, a study of energy partitioning should complement and enhance the coherence investigations suggested earlier. Another phenomenon that could be investigated from an energy partitioning point of view is the possibility of energy traveling toward

a slope being refracted through the bottom in such a way that it reappears along the slope. The energetic feasibility of this process could be examined with energy partitioning techniques and coupled with the parallel use of ray-mode analogy ("fuzzy ray") techniques.

Another area needing further work is range variability in three dimensions. Since the numerical difficulties of modeling three-dimensional range dependence are much greater than for two dimensions, it is not likely that propagation in a three-dimensional range dependent waveguide could be modeled routinely. However, approximate ways for handling certain important cases can and probably should be developed. Some important cases that come to mind involve sea mounts and continental slopes. In a two-dimensional treatment of these types of range variation, one is missing certain diffraction effects by assuming the bathymetry changes to be cylindrically symmetric about the source position. Approximating a sea mount by a hump or ridge encircling the source is aesthetically unpleasing and possibly invalid for sources near the sea mount. It would therefore be advantageous to model potentially important types of three-dimensional features such as those mentioned previously, even if only in an approximate manner.

Perhaps one of the more important areas for future consideration concerns a range averaged description of the lateral variability of the bottom. One of the main concerns here would be to investigate the relationship between bottom loss as it would be measured for a laterally variable bottom and as it would be calculated using a range averaged geoacoustic model. The measurement of bottom loss, especially using multibounce techniques,[27,28] necessarily entails some sort of range averaging since different points along the bottom are sampled for different grazing angles and source-receiver separations. The pertinent question is whether, and in what manner, this measured bottom loss differs from the result obtained using a range averaged description of the geoacoustic environment. Preliminary indications are that there may be little or no relationship between the two types of bottom loss previously mentioned, as can be seen in Fig. V.1. Figure V.1 represents a rather

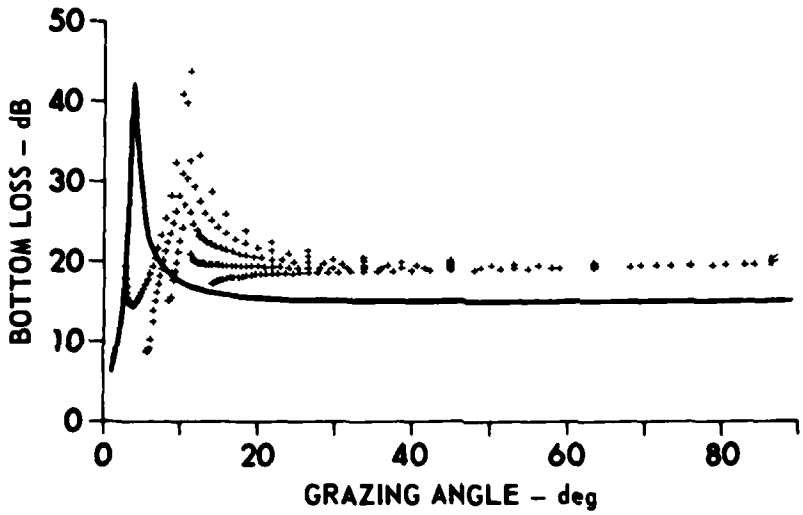

FIGURE V.1
BOTTOM LOSS versus GRAZING ANGLE

ARL:UT
AS-80-876-P
SRR-GA
3-13-80

simple but effective demonstration of the difference one might conceivably encounter between a measured bottom loss and a computed bottom loss using a range averaged geoacoustic model.

The crosses in Fig. V.1 represent a numerical reproduction of a bottom loss measurement using multibounce techniques in which arrivals having up to five bottom bounces were included. The bottom was taken as a half-space having a porosity which varied linearly from 85-65% over 200 km (porosity gradient = 10^{-4} %/m). The bottom loss at the ranges of bottom encounter was assumed to be given by a Rayleigh reflection coefficient and the sediment density and sound speed were obtained as a function of porosity from Hamilton's regression equations.[21,22] The water sound speed at the sediment interface was taken to be 1540 m/sec. For each angle considered in Fig. V.1 there are up to five bottom loss values representative of different numbers of bottom bounces and different source-receiver separations. To correspond more closely to an actual measurement these values should be averaged for each angle. The solid curve represents the Rayleigh reflection coefficient converted to bottom loss for a half-space, with the range averaged geoacoustic parameters generated using the median porosity (75%) over the range interval.

Some significant differences between the two types of bottom loss are apparent in Fig. V.1. For instance, the intromission angle peak has been shifted by about 7° and the high angle values of bottom loss differ by a 5 dB bias. The reason for these differences is that the range averaging of the multibounce bottom loss measurement is nonuniform, in that the range increment over which the averaging occurs varies across the angular spectrum. The high angle measured values sample the bottom over a relatively small range interval near the source and more closely resemble the reflection loss of an 85% porosity sediment. The intermediate and low angle measured values involve more complicated types of range averaging.

The pertinent question to be addressed in further research is how rapidly bottom properties must vary with range before a multibounce

bottom loss measurement becomes totally meaningless. The porosity gradient in Fig. V.1 is small but large differences in the bottom losses result. Future work in this area should attempt to incorporate a more descriptive characterization of the bottom than is available with a Rayleigh reflection coefficient. It is likely that the ARL:UT bottom loss models BOTLOSS[29,30] or BOTREF[31] could easily be incorporated in the numerical measurement synthesis scheme, and would allow vertical variability of the bottom to be incorporated in the study. Other ways of approaching the range averaging problem, such as through mode attenuation coefficients, should also be investigated.

REFERENCES

1. K. E. Hawker, S. R. Rutherford, and P. J. Vidmar, "A Summary of the Results of a Study of Acoustic Interaction with the Sea Floor," Applied Research Laboratories Technical Report No. 79-2 (ARL-TR-79-2), Applied Research Laboratories, The University of Texas at Austin, 5 March 1979.

2. A. D. Pierce, "Extension of the Method of Normal Modes to Sound Propagation in an Almost-Stratified Medium," J. Acoust. Soc. Am. 37, 19-27 (1965).

3. D. M. Milder, "Ray and Wave Invariants for SOFAR Channel Propagation," J. Acoust. Soc. Am. 46, 1259-1263 (1969).

4. S. R. Rutherford, "An Examination of Coupled Mode Theory as Applied to Underwater Sound Propagation," Applied Research Laboratories Technical Report No. 79-44 (ARL-TR-79-44), Applied Research Laboratories, The University of Texas at Austin, 26 July 1979.

5. S. R. Rutherford and K. E. Hawker, "A Consistent Coupled Mode Theory of Sound Propagation for a Class of Nonseparable Problems," to be published in The Journal of the Acoustical Society of America.

6. S. R. Rutherford, "An Examination of Multipath Processes in a Range Dependent Ocean Environment within the Context of Adiabatic Mode Theory," J. Acoust. Soc. Am. 66, 1482-1486 (1979).

7. S. R. Rutherford and K. E. Hawker, "An Examination of the Influence of the Range Dependence of the Ocean Bottom on the Adiabatic Approximation," J. Acoust. Soc. Am. 66, 1145-1151 (1979).

8. P. J. Vidmar, S. R. Rutherford, and K. E. Hawker, "A Summary of Some Recent Results in Acoustic Bottom Interaction," Applied Research Laboratories Technical Report No. 80-6 (ARL-TR-80-6), Applied Research Laboratories, The University of Texas at Austin, 19 February 1980.

9. S. K. Mitchell and K. C. Focke, "Initial Investigations on Shallow Water Acoustics in the ROUGH START Exercise Region," Applied Research Laboratories Technical Letter No. EV-80-9 (ARL-TL-EV-80-9), Applied Research Laboratories, The University of Texas at Austin, February 1980. CONFIDENTIAL

10. R. D. Graves, A. Nagl, H. Überall, and G. L. Zarur, "Range-Dependent Normal Modes in Underwater Sound Propagation: Application to the Wedge-Shaped Ocean," J. Acoust. Soc. Am. 58, 1171-1177 (1975).

11. A. Nagl, H. Überall, A. J. Haug, and G. L. Zarur, "Adiabatic Mode Theory of Underwater Sound Propagation in a Range-Dependent Environment," J. Acoust. Soc. Am. 63, 739-749 (1978).

12. R. D. Graves, A. Nagl, H. Überall, and G. L. Zarur, "Normal Modes in a Sound Channel with Range Dependent Parabolic Sound Speed Profile," Acustica 39, 173-181 (1978).

13. F. B. Jensen and M. C. Ferla, "SNAP: The SACLANTCEN Normal-Mode Acoustic Propagation Model," SACLANTCEN SM-2, SACLANT ASW Research Centre, La Spezia, Italy, 15 January 1979.

14. R. Gonzalez and K. E. Hawker, "The Acoustic Normal Mode Model Nemesis," Applied Research Laboratories Technical Report No. 80-13, (ARL-TR-80-13), Applied Research Laboratories, The University of Texas at Austin (in preparation).

15. K. E. Hawker, A. L. Anderson, K. C. Focke, and T. L. Foreman, "Initial Phase of a Study of Bottom Interactions of Low Frequency Underwater Sound," Applied Research Laboratories Technical Report No. 76-14 (ARL-TR-76-14), Applied Research Laboratories, The University of Texas at Austin, 6 April 1976.

16. S. T. McDaniel, "Parabolic Approximations for Underwater Sound Propagation," J. Acoust. Soc. Am. 58, 1178-1185 (1975).

17. C. W. Spofford, "A Synopsis of the AESD Workshop on Acoustic Propagation Modeling by Non-Ray Tracing Techniques," AESD Tech. Note TN-73-05, Acoustic Environmental Support Detachment (1973) (Unpublished).

18. F. Jensen and H. Krol, "The Use of the Parabolic Equation Method in Sound Propagation Modeling," SACLANTCEN Memorandum SM-72, SACLANT ASW Research Centre, La Spezia, Italy, 15 August 1975.

19. F. D. Tappert, "Selected Applications of the Parabolic Equation Method in Underwater Acoustics," in International Workshop on Low-Frequency Propagation of Noise, Vol. 1, Woods Hole, Massachusetts, 15-19 October 1974, (U.S. Government Printing Office, Washington, DC, 1977), pp. 155-197.

20. B. G. Roberts, Jr., "Horizontal-Gradient Acoustical Ray-Trace Program TRIMAIN," NRL Report No. 7827, Naval Research Laboratory, Washington, DC, 1974.

21. E. L. Hamilton, "Compressional-Wave Attenuation in Marine Sediments," Geophysics 37, 620 (1972).

22. E. L. Hamilton, "Prediction of Deep-Sea Sediment Properties: State-of-the-Art," in Deep-Sea Sediments, Physical and Mechanical Properties, edited by A. L. Inderbitzen (Plenum Press, New York, 1974), pp. 1-43.

23. G. Arfkin, Mathematical Methods for Physicists (Academic Press, New York, 1970).

24. F. S. Chwieroth, A. Nagl, H. Überall, R. D. Graves, and G. L. Zarur, "Mode Coupling in a Sound Channel with Range-Dependent Parabolic Velocity Profile," J. Acoust. Soc. Am. 64, 1105-1112 (1978).

25. L. I. Schiff, Quantum Mechanics (McGraw-Hill Book Co., Inc., New York, 1968).

26. A. O. Williams, "Mode Interactions in an Isovelocity Ocean of Uniformly Varying Depth," J. Acoust. Soc. Am. 67, 177-185 (1980).

27. S. K. Mitchell, K. C. Focke, J. A. Shooter, and N. R. Bedford, "BEARING STAKE--Vertical ACODAC Acoustic Measurements Data Report," (U), Applied Research Laboratories Technical Report No. 78-8 (ARL-TR-78-8), Applied Research Laboratories, The University of Texas at Austin, 15 February 1978. CONFIDENTIAL

28. S. K. Mitchell, K. C. Focke, J. J. Lemmon, and M. M. McSwain, "Analysis of Acoustic Bottom Interaction in BEARING STAKE," (U), Applied Research Laboratories Technical Report No. 79-24 (ARL-TR-79-24), Applied Research Laboratories, The University of Texas at Austin, 23 February 1979. CONFIDENTIAL

29. K. E. Hawker and T. L. Foreman, "A Plane Wave Reflection Loss Model Based on Numerical Integration," J. Acoust. Soc. Am. 64, 1470-1477 (1978).

30. P. J. Vidmar and T. L. Foreman, "A Plane Wave Reflection Loss Model Including Sediment Rigidity," J. Acoust. Soc. Am. 66, 1830-1835 (1979).

31. S. K. Mitchell and J. J. Lemmon, "A Ray Theory Model of Acoustic Interaction with the Ocean Bottom," J. Acoust. Soc. Am. 66, 855-861 (1979).

14 November 1980

DISTRIBUTION LIST FOR
ARL-TR-80-56
UNDER CONTRACT N00014-78-C-0113

Copy No.

Commanding Officer
Naval Ocean Research and Development Activity
NSTL Station, MS 39529
1 Attn: E. D. Chaika (Code 530)
2 CDR K. Evans (Code 520)
3 S. W. Marshall (Code 340)
4 H. Eppert (Code 360)
5 A. L. Anderson (Code 320)
6 L. P. Solomon (Code 500)
7 J. Matthews (Code 360)
8 G. Morris (Code 340)
9 R. R. Goodman (Code 110)

Commanding Officer
Office of Naval Research
Arlington, VA 22217
10 Attn: M. Odegard (Code 483)
11 M. McKisic (Code 486)

12 Office of Naval Research
Branch Office, Chicago
Department of the Navy
536 South Clark Street
Chicago, IL 60605

Commanding Officer
Naval Electronic Systems Command
Washington, DC 20360
13 Attn: J. Sinsky (Code 612)
14 CDR P. Girard (Code 612)
15 Code PME 124-62
16 Code PME 124TA

Director
Naval Research Laboratory
Department of the Navy
Washington, DC 20375
17 Attn: B. B. Adams (Code 8160)
18 O. Diachok
19 F. Ingenito
20 W. Mosley

Copy No.

21 S. Hanish
22 P. Rogers
23 R. Dicus
24 D. Del Balzo

Commanding Officer
Naval Ocean Systems Center
Department of the Navy
San Diego, CA 92152
25 - 27 Attn: E. L. Hamilton
28 M. A. Pederson
29 H. P. Bucker
30 D. Gordon
31 N. Booth
32 R. Bachman
33 R. Shockley
34 T. Kaye

Commander
Naval Sea Systems Command
Department of the Navy
Washington, DC 20362
35 Attn: C. D. Smith (Code 06R/63R)

Chief of Naval Operations
Department of the Navy
Washington, DC 20350
36 Attn: CDR J. Harlette, OP-952D1

37 Commander
Naval Surface Weapons Center
White Oak Laboratory
Department of the Navy
Silver Spring, MD 20910

38 Commander
David W. Taylor Naval Ship Research and
Development Center
Department of the Navy
Bethesda, MD 20034

Distribution List for ARL-TR-80-56 under Contract N00014-78-C-0113 (Cont'd)

Copy No.

Naval Oceanographic Office
NSTL Station, MS 39529
39 Attn: W. Jobst (Code 3400)
40 M. G. Lewis (Code 7200)

Commander
Naval Air Development Center
Department of the Navy
Warminister, PA 18974
41 Attn: C. L. Bartberger
42 P. Haas

Officer in Charge
New London Laboratory
Naval Underwater Systems Center
Department of the Navy
New London, CT 06320
43 Attn: F. R. DiNapoli
44 R. Deavenport
45 J. Papadakis
46 P. Herstein

47 Director Naval Warfare
Deputy Under Sec. Defense R&E
Room 3D1048, Pentagon
Washington, DC 20301

OASN (R,E & S)
Room 4D745 Pentagon
Washington, DC 20301
48 Attn: G. A. Cann

Defense Advanced Research Projects Agency
Acoustic Research Center
Moffett Field, CA 94035
49 Attn: E. Smith

Superintendent
Naval Postgraduate School
Monterey, CA 93940
50 Attn: Library
51 H. Medwin

Distribution List for ARL-TR-80-56 under Contract N00014-78-C-0113 (Cont'd)

Copy No.

Commanding Officer
Naval Air Systems Command
Department of the Navy
Washington, DC 20361
52 Attn: CDR J. Messegee (Code PMA-264)

Commander
Naval Coastal Systems Center
Department of the Navy
Panama City, FL 32407
53 Attn: G. McLeroy

54 - 65 Commanding Officer and Director
Defense Information Service Center
Cameron Station, Building 5
5010 Duke Street
Alexandria, VA 22314

Arthur D. Little, Inc.
15 Acorn Park
Cambridge, MA 02140
66 Attn: G. Raisbeck

Woods Hole Oceanographic Institution
86-95 Water Street
Woods Hole, MA 02543
67 Attn: E. E. Hayes
68 G. Frisk
69 R. Spindel
70 B. Tucholke

Science Applications, Inc.
1710 Goodridge Drive
McLean, VA 22101
71 Attn: J. Hanna
72 C. Spofford
73 L. Dozier

Applied Research Laboratory
The Pennsylvania State University
P. O. Box 30
State College, PA 16801
74 Attn: S. McDaniel

Copy No.

Underwater Systems, Inc.
World Building
8121 Georgia Avenue
Silver Spring, MD 20910
75 Attn: M. S. Weinstein

Marine Physical Laboratory of
The Scripps Institution of Oceanography
The University of California, San Diego
San Diego, CA 92132
76 Attn: F. Fisher
77 G. Shor

Scripps Institution of Oceanography
The University of California, San Diego
La Jolla, CA 92037
78 Attn: Library
79 R. Tyce
80 J. Orcutt
81 L. Dorman

Bell Telephone Laboratories, Inc.
Whippany Road
Whippany, NJ 07961
82 Attn: S. A. Kramer
83 F. Labianca
84 P. Ogushwitz

Planning Systems, Inc.
7900 Westpark Drive, Suite 507
McLean, VA 22101
85 Attn: R. Cavanaugh

TRW, Inc.
TRW Defense & Space Systems Group
Washington Operations
7600 Colshire Drive
McLean, VA 22101
86 Attn: R. T. Brown
87 I. Gereben

Copy No.

SUTRON Corporation
Suite 700
1925 North Lynn Street
Arlington, VA 22209
88 Attn: C. Dabney

Daubin Systems Corporation
104 Crandon Boulevard
Key Biscayne, FL 33149
89 Attn: S. Daubin

Defence Scientific Establishment
HMNZ Dockyard
Devonport, Auckland
NEW ZEALAND
90 Attn: K. M. Guthrie
91 R. N. Denham
92 R. Bannister

School of Mechanical Engineering
Georgia Institute of Technology
Atlanta, GA 30332
93 Attn: Dr. A. D. Pierce

The Catholic University of America
Washington, DC 20064
94 Attn: H. M. Uberall

Department of Geology and Geophysics
Geophysical and Polar Research Center
Lewis G. Weeks Hall for Geological Sciences
The University of Wisconsin, Madison
1215 W. Dayton Street
Madison, WI 53706
95 Attn: C. S. Clay

Courant Institute
251 Mercer Street
New York, NY 10012
96 Attn: D. C. Stickler

Distribution List for ARL-TR-80-56 under Contract N00014-78-C-0113 (Cont'd)

Copy No.

Bolt, Beranek, & Newman, Inc.
50 Moulton Street
Cambridge, MA 02138
97 Attn: P. W. Smith, Jr.

The Institute of Acoustic Research
615 SW 2nd Avenue
Miami, FL 33130
98 Attn: J. Clark
99 R. Flanagan

Department of Ocean Engineering
Massachusetts Institute of Technology
Cambridge, MA 02139
100 Attn: Professor I. Dyer

Hawaii Institute of Geophysics
The University of Hawaii
2525 Correa Road
Honolulu, HI 96822
101 Attn: G. Sutton
102 M. Manghnani

Director
North Atlantic Treaty Organization
SACLANT ASW Research Centre
APO New York 09019
103 Attn: T. Akal
104 W. Kuperman

Defence Research Establishment Pacific
CF Dockyard
Victoria, BC
CANADA
105 Attn: Ross Chapman

Defence Research Establishment Atlantic
9 Grove Street
P. O. Box 1012
Dartmouth, NS
CANADA
106 Attn: I. Fraser
107 D. Chapman

Copy No.

Rosenteil School of Marine and
Atmospheric Science
The University of Miami
10 Rickenbacker Causeway
Miami, FL 33149
108 Attn: Dr. H. DeFarrari

Applied Physics Laboratory
The Johns Hopkins University
Johns Hopkins Road
Laurel, MD 20810
109 Attn: L. H. Wallman

The University of Miami
10 Rickenbacker Causeway
Miami, FL 33149
110 Attn: Dr. F. Tappert

Physics Department
The University of Rhode Island
Kingston, RI 02881
111 Attn: C. Kaufman

Department of Electrical Engineering
Polytechnic Institute of New York
Farmingdale, NY 11735
112 Attn: L. B. Felsen

113 I. Tolstoy
Knockvennie, Castle Douglas
S. W. SCOTLAND
GREAT BRITAIN

National Oceanic and Atmospheric Administration
Environmental Research Laboratories
Boulder, CO 80303
114 Attn: J. R. Wait

Department of Geology
The University of Texas at Austin
Austin, TX 78712
115 Attn: Dr. M. M. Backus
116 Dr. Clark Wilson

Copy No.

Physics Department
The University of Auckland
Private Bag, Auckland
NEW ZEALAND
117 Attn: A. C. Kibblewhite
118 G. Bold
119 C. T. Tindle

Brown University
Providence, RI 02912
120 Attn: A. O. Williams, Jr.

The Lamont-Doherty Geological Observatory
Columbia University
Palisades, NY 10964
121 Attn: R. D. Stoll
122 H. A. Kutschale
123 R. E. Houtz

Ocean Data Systems, Inc.
3255 Wing Street
San Diego, CA 92110
124 Attn: Kenneth R. Osborne

125 Office of Naval Research
Resident Representative
Room No. 582, Federal Bldg.
Austin, TX 78701

126 Garland R. Barnard, ARL:UT

127 Glen E. Ellis, ARL:UT

128 Terry L. Foreman, ARL:UT

129 Loyd Hampton, ARL:UT

130 Kenneth E. Hawker, ARL:UT

131 Claude W. Horton, Sr., ARL:UT

132 Robert A. Koch, ARL:UT

133 James F. Lynch, ARL:UT

134 Stephen K. Mitchell, ARL:UT

Distribution List for ARL-TR-80-56 under Contract N00014-78-C-0113 (Cont'd)

Copy No.

135	Susan G. Payne, ARL:UT
136	Clark S. Penrod, ARL:UT
137	Jack A. Shooter, ARL:UT
138	Paul J. Vidmar, ARL:UT
139	Reuben H. Wallace, ARL:UT
140	Library, ARL:UT
141 - 171	Reserve, ARL:UT


DATE
ILME